

# In-materio reservoir computing with single-walled carbon nanotube/porphyrin-polyoxometalate random network A novel approach for next-generation machine intelligence

著者	Deep Banerjee
year	2021
その他のタイトル	単層カーボンナノチューブ/ポルフィリン-ポリ酸ランダムネットワークを用いたマテリアルリザーバー演算素子 次世代機械知能への新規アプローチ
学位授与年度	令和3年度
学位授与番号	17104生工博甲第425号
URL	<a href="http://hdl.handle.net/10228/00008819">http://hdl.handle.net/10228/00008819</a>

**In-materio reservoir computing with single-walled carbon  
nanotube/porphyrin-polyoxometalate random network – A  
novel approach for next-generation machine intelligence**



**Kyutech**

Kyushu Institute of Technology

by

**Deep Banerjee**

**Dissertation submitted in partial fulfilment  
of the requirement for the degree of  
Doctor of Philosophy**

**SUPERVISOR:**

**PROF. HIROFUMI TANAKA**

**Graduate School of Life Science and Systems Engineering**

**Kyushu Institute of Technology**

**2021**

## **Acknowledgement**

I dedicate this research work in the loving memory of my Grandfathers Mr. Anuj Kumar Banerjee, Mr. Basudeb Roy Chowdhury, Mr. Radhakanta Roychowdhury, Grandmother Mrs. Chhabhi Rani Roy Chowdhury and Uncle Mr. Sanjay Kumar Banerjee.

Firstly, my sincere thanks to my supervisor Prof. Hirofumi Tanaka for believing in me and giving me this great opportunity of conducting Ph.D research work in the multidisciplinary field of materials science and unconventional computing. His constant guidance, conceptual ideas and support has been an assistance to me in writing up this dissertation, shaping my analytical skills and helping me grow as an independent researcher over the years. Along with him, I also show my deepest gratitude to Prof. Takashi Morie, Prof. Hakaru Tamukoh and Prof. Takuya Matsumoto for their valuable suggestions and advices as my committee members.

A valuable mention goes to the Ministry of Education, Culture, Sport, Science and Technology (MEXT) of Japan for funding my full three year Ph.D course through Global Assistive Adaptive Robotic Program (GAAR). The lectures in the program were comprehensive and gave an insight to the extensive research areas being dealt in varied fields of science. I would also like to express my gratitude towards the entire student administrative staff, especially Mrs. Hayashi, of KYUTECH, Wakamatsu for carrying out all the legal documented procedures on my behalf for a smoother admission to the institute.

I would like to acknowledge Dr. Chandramouli Subramaniam of IIT Bombay, India, a dear colleague of Prof. Tanaka, whose recommendation provided me this beautiful opportunity of becoming an esteemed part of the present lab. My humble respect also goes to Prof. Gimzewski of University of California Los Angeles, another colleague of Prof. Tanaka, whose research work in the field of physical reservoir computing served as an inspiration and reference for my doctoral thesis.

A special thanks goes to Prof. Usami, Dr. Saman Azhari, of Tanaka Lab for being by my side and brushing up my experimental, writing and presenting skills. A genuine shout out goes to Yu Xinguang, Hadiyawarma and Wahyu Aji, the previous Tanaka lab members, for their support, teachings and fruitful discussions thought my three years journey.

I pay my gratitude to our beloved Lab Secretaries, Mrs. Ryoko Ikeno, Mrs. Mizuho Shimoda and my tutor Mr. Yusuke Nakao for being my friendly guide and processing all my personal problems in times of trouble and need.

Lastly and most importantly, my love, respect and regards to the most prized possessions of my life; my mother Seema Banerjee, father Deb Kumar Banerjee, sister Archita Banerjee and extended family in India. To my school teachers, especially Mrs. Motiri Barua, Miss Chanda Chatterjee and Miss Suchismita Sanyal; my college teachers, Prof. Reena Ghosh, Prof. Indranil Chakraborty, Prof. Rahul Sharma, Prof. Sanjib Ganguly, Prof. Swapan Chakrabarti and Prof. Dipankar Chattopadhyay. To my childhood friend Sourav Das, school friends Priyabrata Garai, Kaustav Sengupta, Partha Halder, Sayantan Dutta, college buddies Manas Sajjan, Utsab Mitra, Prasenjit Das, Rahul Ghosh, Navendu Mondal, Kaustav Das Gupta, Arkopal Roy, Sougata Mallick, Shankar Saha, Krishnendu Pal, Anirban Paul, Devleena Samanta, Nairhita Samanta, Arya Gupta, Hrishita Bhattacharya, Ahana Dey, Sayantan Roy, Madhurima Bhattacharya, Maku Moronshing, Vishwanath Kalyani, Debjani Ghosh and Japan friends Souraj Mandal, Shubhendu Ranadive, Pancho Dachkinov, Ryan Labebe and Jimmy Majumdar. Thank you all for being my pillar and bearing my tantrums. Even though they were physically absent, but their immeasurable love, blessings, support, advices and teachings showered virtually has always been a boost of positivity at the hardest times of my struggle. Their trust and faith in me is what defines my existence as a human being today. I will always be indebted to them and promise to continue to work harder so that my journey of success and happiness becomes a part of their life stories too which they can cherish it for eternity when rummaging through their diary of memorable moments.

## Table of Contents

<b>Abstract</b> .....	7
<b>Chapter 1</b> .....	9
<b>Introduction and Literature review</b> .....	9
<b>1.1 General Introduction</b> .....	9
<b>1.2 The human brain and the von Neumann architecture</b> .....	9
<b>1.3 Evolution of artificial neural networks</b> .....	12
<b>1.4 The existing problem</b> .....	20
<b>1.5 Reservoir computing: A general overview</b> .....	21
<b>1.6 A survey of physical reservoir devices</b> .....	23
<b>1.7 RC with nano networks: A brain equivalent system</b> .....	29
<b>1.8 Problem statement</b> .....	35
<b>1.9 Objective study</b> .....	36
<b>1.10 Research scope</b> .....	36
<b>1.11 Outline of the thesis</b> .....	37
<b>1.12 References</b> .....	38
<b>Chapter 2</b> .....	51
<b>Methodology</b> .....	51
<b>2.1 Introduction</b> .....	51
<b>2.2 Chemicals and materials</b> .....	51
<b>2.3 Synthesis of single-walled carbon nanotube/porphyrin polyoxometalate (SWNT/Por-POM) dispersion</b> .....	52
2.3.1 Purification of HiPCo SWNT.....	52
2.3.2 Dispersion of HiPCo SWNT with Por-POM.....	53
<b>2.4 Fabrication of the micro electrode array</b> .....	54
<b>2.5 SWNT/Por-POM random network thin film deposition</b> .....	54
<b>2.6 Atomic force microscopy (AFM)</b> .....	56
<b>2.7 Field Emission Scanning Electron Microscopy (FE-SEM)</b> .....	58
<b>2.8 Spectroscopic studies</b> .....	58
<b>2.8 Electrical measurements</b> .....	60
2.8.1 The current –voltage ( <i>I-V</i> ) characteristic of the SWNT/Por-POM device.....	60
2.8.2 The current –time ( <i>I-t</i> ) characteristic of the SWNT/Por-POM device.....	61
<b>References</b> .....	62

<b>Chapter 3</b> .....	63
<b>Reservoir dynamics emerging from an incidental structure of single-walled carbon nanotube/porphyrin-polyoxometalate complex</b> .....	63
<b>Abstract:</b> .....	63
<b>3.1 Introduction</b> .....	64
3.2.1 <i>SWNT/Por-POM dispersion</i> .....	67
3.2.2 <i>Fabrication of MEA substrate</i> .....	67
3.2.3 <i>Thin film deposition of SWNT/Por-POM computational material</i> .....	67
3.2.4 <i>Characterization</i> .....	68
3.2.5 <i>Electrical Measurements</i> .....	68
<b>3.3 Results and discussion</b> .....	69
<b>3.4 Conclusion</b> .....	76
<b>References</b> .....	78
<b>Chapter 4</b> .....	84
<b>Fourier transform waveforms via in-materio reservoir computing from single-walled carbon nanotube/porphyrin-polyoxometalate complex</b> .....	84
<b>Abstract</b> .....	84
<b>4.1 Introduction</b> .....	85
<b>4.2 Methods</b> .....	86
4.2.1 <i>SWNT/Por-POM dispersion</i> .....	86
4.2.2 <i>Fabrication of MEA substrate</i> .....	86
4.2.3 <i>Thin film deposition of SWNT/Por-POM computational material</i> .....	87
4.2.4 <i>Measurements</i> .....	87
<b>4.3 Results and discussion</b> .....	88
<b>4.4 Conclusion</b> .....	100
<b>References</b> .....	101
<b>Chapter 5</b> .....	104
<b>Room temperature demonstration of in-materio reservoir computing for optimizing Boolean function with single-walled carbon nanotube/porphyrin-polyoxometalate composite</b> .....	104
<b>Abstract</b> .....	104
<b>5.1 Introduction</b> .....	105
<b>5.2 Methods</b> .....	108
5.2.1 <i>SWNT/Por-POM dispersion</i> .....	108

5.2.2 Fabrication of MEA substrate .....	108
5.2.3 Thin film deposition of SWNT/Por-POM computational material.....	108
5.2.4 Measurements .....	109
5.3 Results and discussion .....	110
5.4 Conclusion.....	123
References.....	124
<b>Chapter 6</b> .....	127
<b>Binary object classification with tactile sensory input information of via single-walled carbon nanotube/porphyrin-polyoxometalate network as in-materio reservoir computing</b> .....	127
Abstract .....	127
6.1 Introduction .....	128
6.2 Methods.....	129
6.2.1 SWNT/Por-POM dispersion .....	129
6.2.2 Fabrication of MEA substrate .....	129
5.2.3 Thin film deposition of SWNT/Por-POM computational material.....	130
5.2.4 Tactile sensory information and conversion to time-series data .....	130
6.3 Results and Discussion.....	132
6.4 Conclusion.....	140
References.....	141
<b>Chapter 7</b> .....	144
<b>Future scope and Conclusion</b> .....	144
7.1 Future scope.....	144
7.2 Conclusion.....	147
References.....	152
<b>List of Publications</b> .....	153
<b>List of Conferences</b> .....	154
Oral Presentations .....	154
Poster Presentations .....	155

## Abstract

In a layman's term, computation is defined as the execution of a given instruction through a programmable algorithm. History has it that starting from the simplest calculator to the sophisticated von Neumann machine, the above definition has been followed without a flaw. Logical operations for which a human takes a minute long to solve, is a matter of fraction of seconds for these gadgets. But contrastingly, when it comes to critical and analytical thinking that requires learning through observation like the human brain, these powerful machines falter and lag behind. Thus, inspired from the brain's neural circuit, software models of neural networks (NN) integrated with high-speed supercomputers were developed as an alternative tool to implement machine intelligent tasks of function optimization, pattern, and voice recognition. But as device downscaling and transistor performance approaches the constant regime of Moore's law due to high CMOS fabrication cost and large tunneling energy loss, training these algorithms over multiple hidden layers is turning out to be a grave concern for future applications. As a result, the interplay between faster performance and low computational power requirement for complex tasks deems highly disproportional. Therefore, alternative in terms of both NN models and conventional Neumann architecture needs to be addressed in today's age for next-generation machine intelligence systems. Fortunately, through extensive research and studies, unconventional computing using a reservoir based neural network platform, called in-materio reservoir computing (RC) has come to the rescue. In-materio RC uses physical, biological, chemical, cellular automata and other inanimate dynamical systems as a source of non-linear high dimensional spatio-temporal information processing unit to construct a specific target task. RC not only has a three-layer simplified neural architectural layer, but also imposes a cheap, fast, and simplified optimization of only the readout weights with machine intelligent regression algorithm to construct the supervised objective target via a weighted linear combination of the readouts.

Thus, utilizing this idea, herein in this work we report such an in-materio RC with a dynamical random network of single walled carbon nanotube/porphyrin-polyoxometalate (SWNT/Por-POM) device. We begin with Chapter 1, which deals with the introduction covering the literature of ANN evolution and the shortcomings of von Neumann architecture and training models of these ANN, which leads us to adopt the in-materio RC architecture. We design the problem statement focused on extending the theoretical RC model of previously suggested SWNT/POM network to an experimental one and present the objective of fabricating a random network based on nanomaterials as they closely resemble the network structure of the brain. Finally, we conclude by stating the scope of this research work aiming towards validating the non-linear high dimensional reservoir property SWNT/Por-POM holds for it to explicitly demonstrate the RC benchmark tasks of optimization and classification.

Chapter 2 describes the methodology including the chemical repository required for the facile synthesis of the material. The synthesis part is divided broadly into SWNT purification and then its dispersion with Por-POM to form the desired complex. It is then followed up with the



microelectrode array fabrication and the consequent wet-transfer thin film deposition to give the ultimate reservoir architecture of input-output control read pads with SWNT/por-POM reservoir. Finally we give a briefing of AFM, UV-Vis spectroscopy, FE-SEM characterization techniques of SWNT/por-POM complex along with the electrical set-up interfaced with software algorithm to demonstrate the RC approach of in-materio machine intelligence.

In Chapter 3, we study the current dynamics as a function of voltage and time and validate the non-linear information processing ability intrinsic to the device. The study reveals that the negative differential resistance (NDR) arising from redox nature of por-POM results in oscillating random noise outputs giving rise to  $1/f$  brain-like spatio-temporal information. We compute the memory capacity (MC) and prove that the device exhibits echo state property of fading memory, but remembers very little of the past information. The low MC and high non-linearity allowed us to choose mostly non-linear tasks of waveform generation, Boolean logic optimization and one-hot vector binary object classification as the RC benchmark.

The Chapter 4 relates to the waveform generation task. Utilizing the high dimensional voltage readouts of varying amplitude, phase and higher harmonic frequencies, relative to input sine wave, a regression optimization was performed towards constructing cosine, triangular, square and sawtooth waves resulting in a high accuracy of around 95%.

The task complexity of function optimization was further enhanced in Chapter 5 where two inputs were used to construct Boolean logic functions of OR, AND, XOR, NOR, NAND and XNOR. Similar to the waveform, accuracy over 95% could be achieved due to the presence of NDR non-linearity.

Furthermore, the device was also tested for classification problem in Chapter 6. Here we showed an off-line binary classification of four object toys; hedgehog, dog, block and bus, using the grasped tactile information of these objects as inputs obtained from the Toyota Human Support Robot. A one-ridge regression analysis to fit the hot vector supervised target was used to optimize the output weights for predicting the correct outcome. All the objects were successfully classified owing to the  $1/f$  information processing factor.

Lastly, we conclude the section in Chapter 7 with the future scope of extending the idea to fabricate a 3-D model of the same material as it opens up opportunity for higher memory capacity fruitful for future benchmark tasks of time-series prediction. Overall, our research marks a step stone in utilizing SWNT/por-POM as the in-materio RC for the very first time thereby making it a desirable candidate for next-generation machine intelligence.

## **Chapter 1**

### **Introduction and Literature review**

#### **1.1 General Introduction**

The chapter gives a brief overview of the background, motivation and based knowledge gathered from literature as guidance on assessing and evaluating the work results. The main focus relies on the framework of reservoir computing and the present materials that are being researched for emulating it physically in order to have a paradigm shift from the conventional von Neumann architecture to the in-materio unconventional way. We begin by talking about different artificial neural networks that are being commonly used in the realm of machine intelligence and then talk about the importance of RC in the context of its simple architectural design with an easy and fast learning approach. We survey about the materials being under use and move on to talk about the importance of using random nano-networks especially based on single-walled carbon nanotube and polyoxometalate complexes for this in materio-RC purpose.

#### **1.2 The human brain and the von Neumann architecture**

The well-known natural intelligent computer that exists today is the human brain.<sup>1</sup> The brain is a complex dynamical entity<sup>2</sup> and is the central organ of the nervous system which tackles all information processing being signaled from every part of the human body. The basic functional units that carry out these tasks are the neurons and the synapses as shown in Fig. 1.1a. Generally the neuron gathers electrical signals and integrates them over time to produce useful information in the form spikes. The spikes are then transferred to the post neuron via chemical transmitters called synapses which acts as the memory cell unit. Depending upon the strength of the incoming

spike these synapses can modulate their weights to become strong or weak and produce either meaningful excitatory or inhibitory pulses to be transferred to the next neuron. The entire principle works as a 'leaky and fire integrator'<sup>3</sup> where incoming signals are integrated and fired only when the neuron reaches a threshold to keep the information process going. Although looks simple in picture, but in reality such information exchange happens throughout the brain network in a parallel and hierarchical way among billions of neurons and trillions of synapses as shown in Fig. 1.1b. Such network connection produces neuronal activities of different strengths which are learned and memorized simultaneously over the synapses. Analogous to the brain, the von Neumann architecture Fig. 1.1c too enables calculations in a similar way, except that here the basic building blocks are the billions of transistors coupled together via complex circuitry. The development of transistor became the step stone for creating electronic microprocessors to produce integrated circuits that transferred information in binary codes of '0' and '1'. With the advent of Moore's law<sup>4,5</sup>, miniaturization of electronic components have made von Neumann architectures to conduct operation at the rate of 10 billion/s much higher than the human brain with a rate of 1000/s as suggested in the book "*The computer and the Brain*" by John von Neumann. However, such speedy performance comes at the cost of 100 Watts of power consumption, where only 10 Watts is used up by the palm sized brain to perform intelligent tasks of thinking, learning, pattern and speech recognition. When it comes to the tug of war between speed and efficiency, the latter always has a winning situation because modern day technology demands energy consumption maintaining the same performance speed.

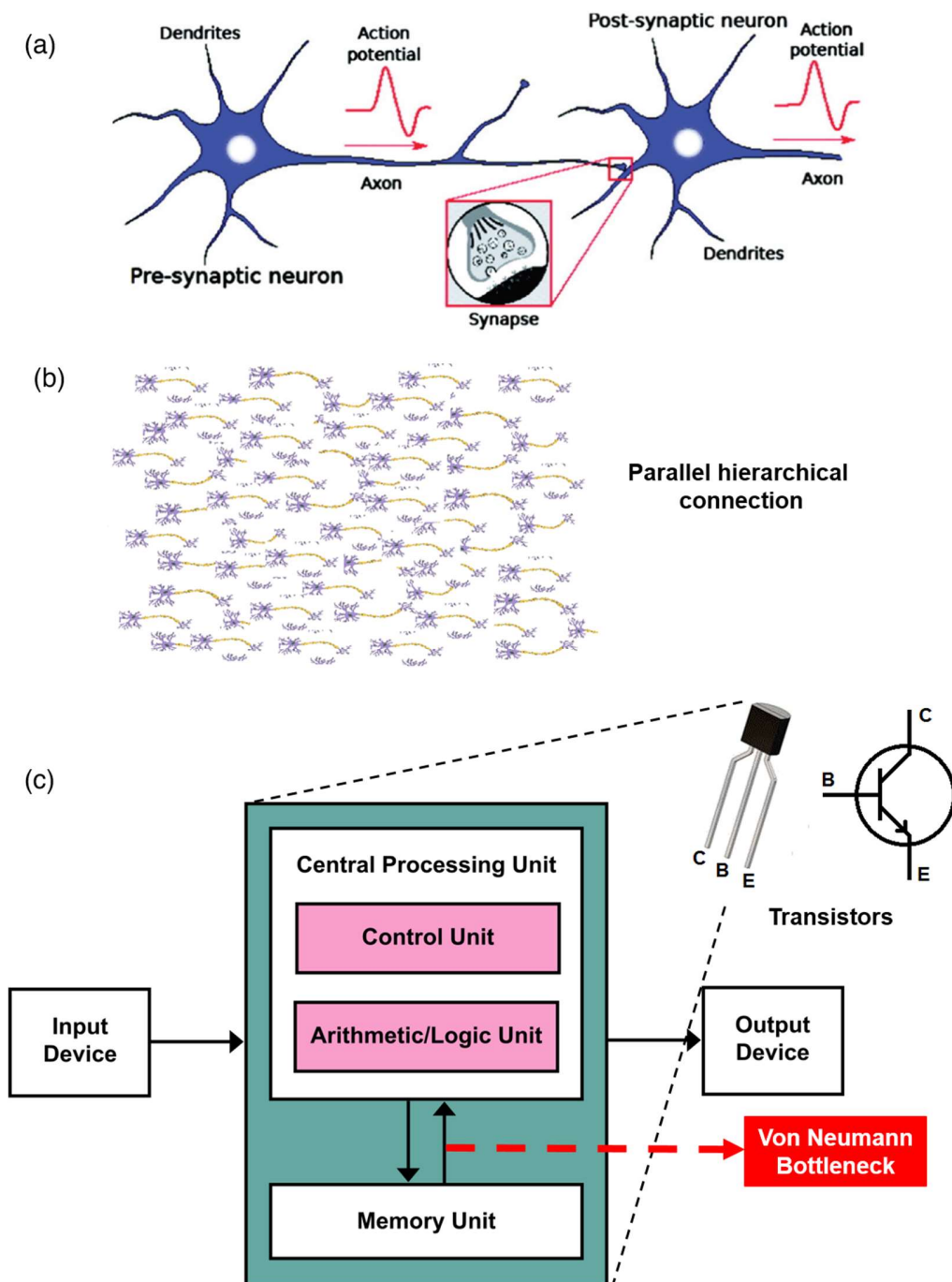


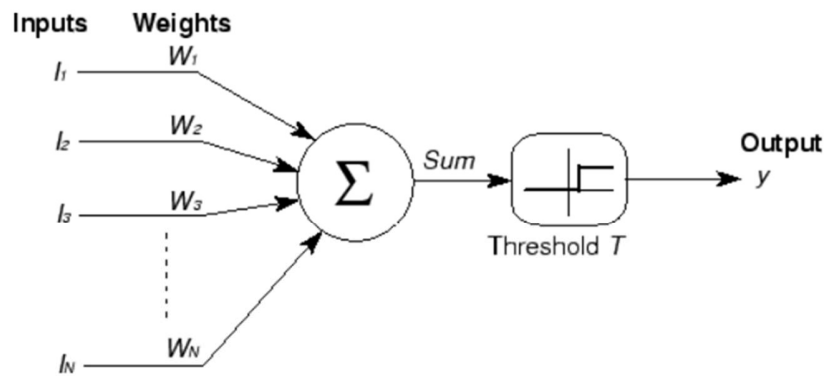
**Fig. 1.1** The brain and the von Neumann architecture. (a) The processing unit, neuron and the memorization unit, synapse of the human brain acting for learning and information transfer.<sup>6</sup> (b) Multiple neurons and synapses are stacked in a hierarchical fashion to allow parallel computation. (c) von Neumann architecture with separate memory and processing creating a bottleneck in transfer rate. *Image source: (b) towardsdatascience portal, (c) Wikipedia.*

One easy solution that most people come up with is to continue with device downscaling, but Moore's law<sup>7</sup> is not an everlasting phenomena. Factors such as energy dissipation and high fabricating cost for CMOS circuitry limits this option to be a wise choice. But, even if somehow this becomes a viable option in near future, then the problem of von Neumann bottleneck, Fig. 1.1c, remains a big issue. Due to the presence of separate memory and processing unit, a huge amount of power and time is consumed in data transferring between the two interfaces, hence causing a latency. So, the most probable solution to come up with is to adopt the brain structure of massive parallelism which results in a small-world topology of faster and efficient information processing<sup>6</sup> along with unified processing and learning to compute brain like intelligent tasks on conventional computers. Thus began the dawn of making intelligent machines whereby the already present computers were instructed to follow constructive algorithms based on the neuron-synapse model of the brain leading to the discovery of a booming scientific field called the 'artificial neural network' (ANN).

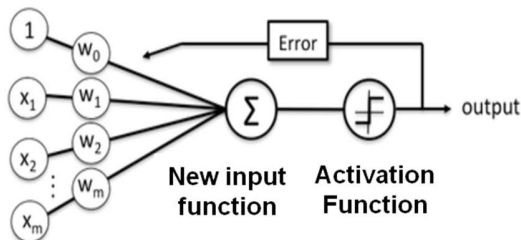
### **1.3 Evolution of artificial neural networks**

The first conceptual circuit based on an input output neuron system was proposed in 1943 by Warren S. McCulloch and Walter Pitts shown in Fig. 1.2a. The McCulloch-Pitts model (MP)<sup>8</sup> describes the complex processing of the brain using a threshold electronic gate where a neuron takes an input connected with synapses of specific weights, and outputs a valuable '1' only when it reached a threshold otherwise it remained in the '0' state. One of major drawback of this model was that the weights were fixed manually and was adjusted only for a given task thereby lacking any self-learning from the output decision. To tackle this, Frank Rosenblatt came up with the idea of first perceptron model<sup>9</sup> in 1958, depicted in Fig. 1.2b.

(a)



(b)



(c)



(d)

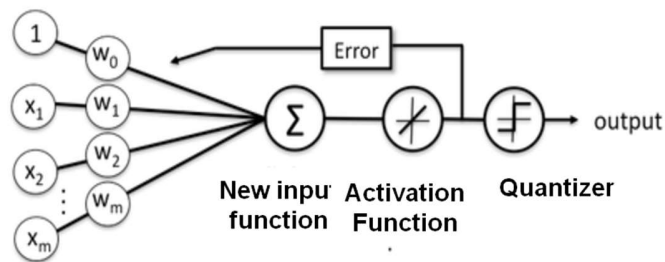


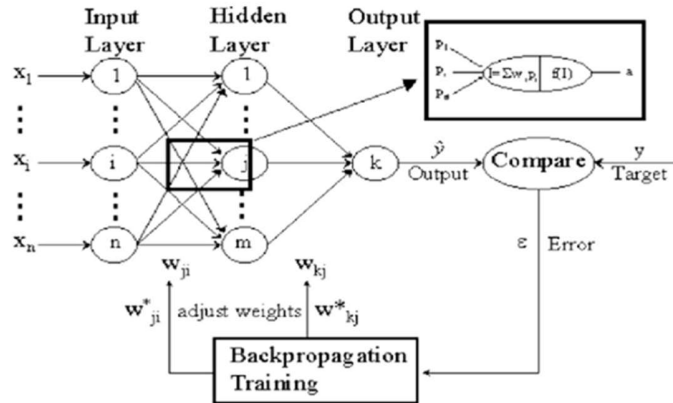
**Fig. 1.2** Artificial neural network architectures. (a) The McCulloch-Pitts model of a simple one unit neuron-synapse network. (b) The Frank Rosenblatt model with the concept of single layer perceptron. (c) Frank Rosenblatt with IBM 704. (d) The Widrow-Hoff model of trainable weights, a successor of MP model. *Image source: towradscience portal*

The perceptron model is inspired from the Hebbian learning rule,<sup>10</sup> where synapses of variable strengths between layers of neurons are implemented to carry out binary output responses or ‘yes’ or ‘no’ tasks. He developed his concept using an IBM 704, 5 ton computer, the size of the room, Fig. 1.2c, and showed that by using a feedback between the output and its preceding neuron layer the weights can be self-learned like the human brain and hence can formulate the task without the requirement of manual labor. The idea was highly welcomed and based on this technique Bernard Widrow and Ted Hoff in 1960 redefined the MP model and constructed an equivalent electronic network with memistors by adding an extra output layer after the threshold activation function to incorporate the learning of the weights hence calling it an Adaptive Linear Element (ADALINE),<sup>11</sup> Fig. 1.2d. Both perceptron and ADELINe were designed for binary classification purposes, but the former majorly use the output class as a reference for optimizing the synaptic weights while the latter used the predicted values from the inputs to do the same via an adaptive algorithm. The concepts though solved the purpose of self-adjustable weights and imparted self-learning but in 1969 Minsky and Papert<sup>12</sup> found that the computational capability of these models were limited to only linearly separable tasks like OR and AND functions and failed for higher non-linear complexities like XOR, as they are solely linear classifiers with linear activation functions. Thus, began the dark ages in the field of ANN when no prime evolution happened until the mid-1980s when a revolution in the training algorithm of perceptron layers was adopted through the contributions from Webros, Rumelhart, Hinton and Williams. They solved the problem by fixing three major fallacies in the existing model; (i) included multiple perceptron layers for higher weights and information processing, (ii) implement non-linear activations in all the neuronal layers and (iii) adopted the back propagation (BP) algorithm<sup>13,14</sup> for optimizing weights in the each layer for better learning and classifying. The model was termed as the multi-layer perceptron (MLP),<sup>15,16</sup>

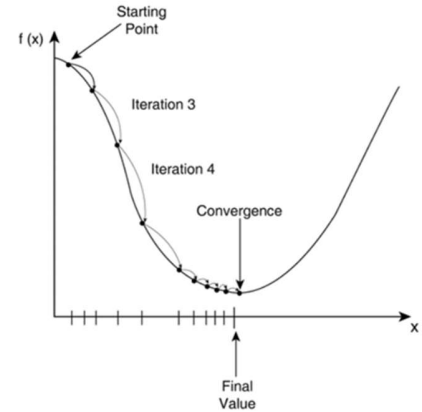
Fig. 1.3a, and became a subclass of today's deep feed-forward neural network architecture (FFNN). The concept of combining multiple linear preceptors through synapses, like the brain, and coupling it with BP learning was proven to be a valid method for approximating any non-linear function that is continuous.<sup>17,18</sup> BP is a supervised learning model where each output class is trained with a specific target task. To achieve the best result, the error between the target and the weighted linear output needs to be minimized. For this, the outputs, obtained from feed forwarding the input information is tested and if there's a mismatch, then via BP, each node of the hidden layer is trained using a gradient descent method, Fig. 1.3b, where the aim is to find the optimized weights of each neuron so that the weighted combination with the respective activation functions descent down a convergence point via repeated iterations producing the minimum error. The algorithm works on a boundary condition that each activation function has to be differentiable, so non-linear functions like *tanh* or *sigmoid* becomes the common choice for such architectures. MLP major use has been in the context of pattern recognition<sup>19</sup> where features of each pixel in the image serve as the inputs to the hidden layers which are then non-linearly processed by the neurons of each hidden layer to get the desired correct pattern over repeated trainings via BP method. Though useful, but the model complexity grows as the pixel size of image; meaning larger arrays require excessive amount of hidden neurons and layers in order to process big data viably and efficiently. To address this, a new architecture called convolutional neural network (CNN)<sup>20,21</sup> was introduced in 1994 by Yann LeCun as depicted in Fig. 1.3c.



(a)



(b)



(c)

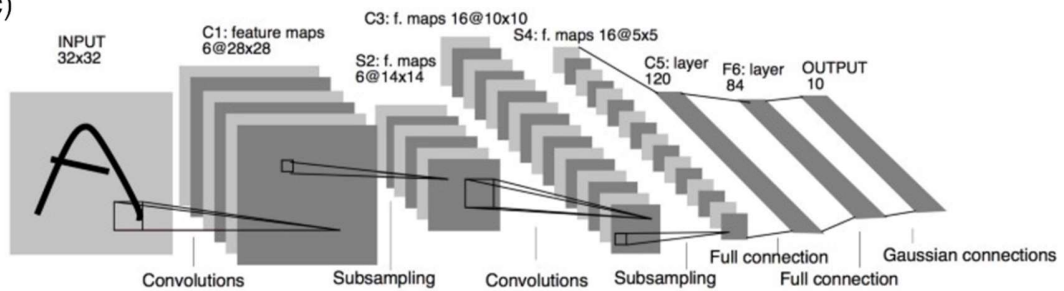


**Fig. 1.3** Multi-layer perceptron (MLP) and the convolution neural network. (a) MLP model developed by Rumelhart, Hinton and Williams by using the backpropagation (BP) learning technique. (b) Gradient descent method implemented in BP to compute error and converge to the minimum for optimization. (c) The first CNN model named LeNet-5 developed by Yann LeCun. *Image source: towardsdatascience portal for all.*

It consists of a convolution layer, which is aimed at extracting patches of features distributed in image to be used as inputs opposed to taking each pixel one by one as in MLP. This is done by fixing a kernel matrix of definite array with respective weight values those strides along a section of the input pixel array, connected to the neurons in the convolution layer, to produce the desired feature map array. The feature maps are passed as information to neurons of the pooling layer, where a smaller dimensional matrix is used to pick up the maximum values from the feature map matrix is thereby reducing the input dimension further to be processed in the sparsely connected MLP layer. Finally the weighted linear optimized feature is collected at the output layer to generate the given image. For maximum accuracy the same BP algorithm is adopted, but only to one layer of MLP thereby reducing both the cost and time of training compared to the MLP architecture. In the field of deep learning,<sup>22</sup> CNN is considered the best architecture to replicate the human visionary concept with maximum efficiency as proven by the AlexNet AI system<sup>23,24</sup> that won the 2012 ImageNet contest hands down with 85% accuracy. Owing to their popularity and advantages in imparting machine intelligence these above mentioned architectures are still not deemed to be considered a close replica of the human brain. The brain consists of one layer of recurrent hidden units and is considered a dynamical system, where the information is not just restricted to the spatial dimension, like the perceptron models, but extends to temporal dimension as well. Neuronal activities studied via electroencephalography (EEG)<sup>25</sup> have shown that neuronal electrical signals produced from a time-varying input signal travels in every direction due to such interconnections resulting in random signals of time varying spatial information as shown in Fig. 1.4a.

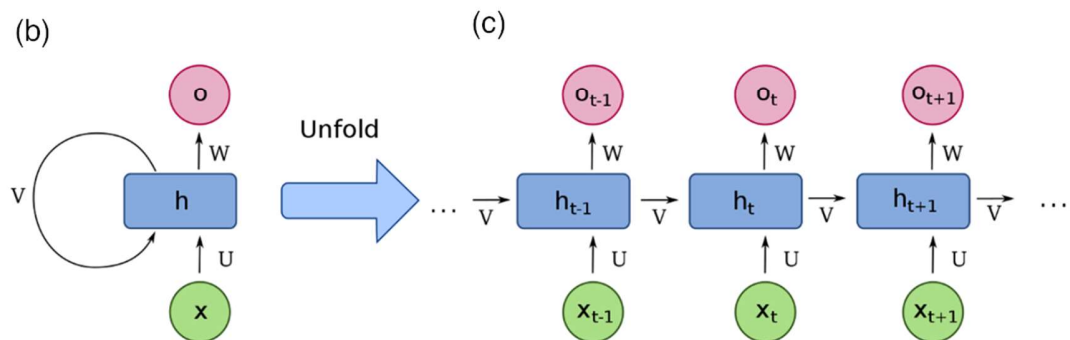
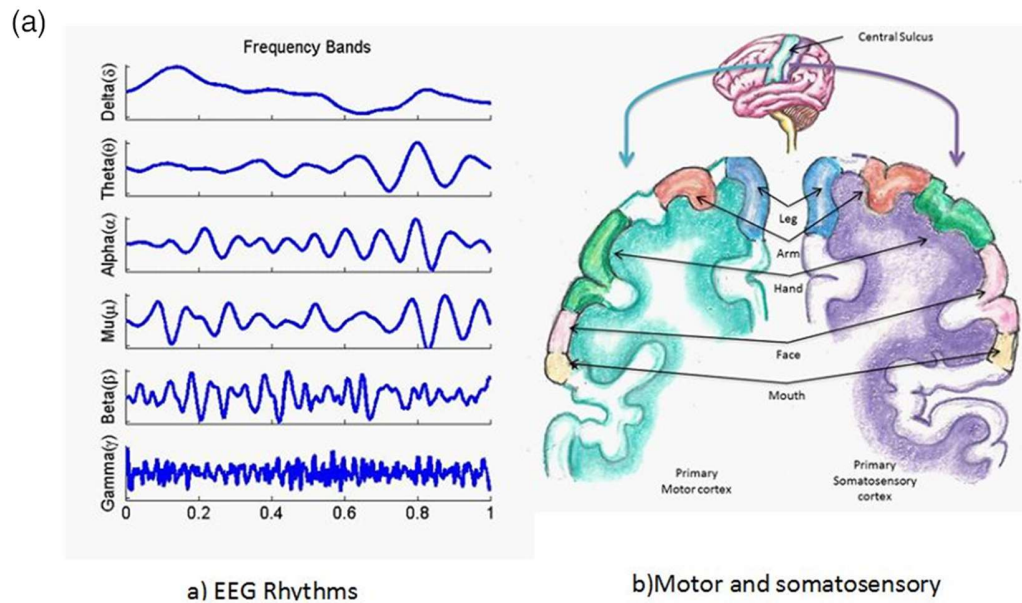


**Fig. 1.4** Brain is a recurrent neural structure. (a) The EEG of brain shows multiple neuron activities at differing time scales.<sup>25</sup> (b) The recurrent neural network (RNN) proposed by Rumelhart. (c) The unfolding of RNN to understand the backpropagation through time algorithm. *Image source: towardsdatascience portal.*

Such dynamical processing is absent in the present FFNN, as the information is only transferred in one direction containing only spatial information. Thus, call for a new architectural design was very much needed which was later on addressed by David Rumelhart in 1986 by introducing the concept of recurrent neural network (RNN)<sup>26</sup> shown in Fig. 1.4b. In RNN the input  $x$  is mapped to the output  $O$  via the hidden state  $h$ , but here the multiple hidden layers are created by recursively using the hidden state of the prior input as its new input ( $v$ ) along with the current input  $U$  which can be understood from the unfolded version shown in Fig. 1.4c. The main advantages of the RNN is (i) it learns from its past information by using the same parameters of  $U$ ,  $v$  and  $W$ , irrespective of the size of the network, (ii) because of this it can process sequential input of any length without the need of increasing the hidden layers as in MLP or CNN and (iii) since the coefficients are correlated to the past information, so temporal learning is automatically incorporated along with the spatial information. In RNN too, the training is done at all the layers by a modified BP algorithm which includes temporal parameter, formulated as back propagation through time (BPTT) popularized by Webros in 1990.<sup>27</sup> Since RNN is a spatio-temporal dynamical system, normal BP cannot be used as it only optimizes the errors ( $U$  and  $W$ ) for the output ( $O$ ) and previous neuron layer ( $x$ ) without causing any change to the recurrent parameter ( $v$ ) of the hidden state. So BPTT takes into consideration of this part and it does so by unrolling the network as seen in Fig. 1.4c into each time-step layer, calculates and accumulates the error for each time-step, averages out all the errors, rolls up the network and then updates the weight by a gradient descent method.

## 1.4 The existing problem

The evolution of ANN has been a milestone in the age of machine intelligence so much that they are even being implemented with conventional von Neumann hardware<sup>28</sup> to carry out tasks like function approximation, pattern recognition, speech recognition and time series forecasting. But in order to match up at par with brain, learning algorithms are constantly being updated for it to handle big data in faster and convenient way. In this regard supercomputers like Fugaku,<sup>29</sup> are coming into action with high end GPU's, CPU's and memory units, built up of numerous transistors and large wiring circuitry, to ease the algorithm process of these neural networks with faster data transfer. But in order to compute 16000 TFLOPS/s it consumes a tremendous power of around 30 MW. This inefficiency not just arises from big data handling, but also from the existing training platform of BP or BPTT. Firstly, it has to train multiple hidden layers, so a lot of power is consumed in iterating every layer to learn at the best accuracy. Secondly, the gradient descent which used for the optimization of weights, suffers from a big problem of vanishing gradient, meaning that for systems with low memory, the past information is forgotten quickly making it difficult to converge and give correct result. So alternatively high memory systems have to be incorporated which increases the data storage space and hence directly the transfer process due to the bottleneck. Hence, the concern for maximized performance at a faster and energy efficient way boils down to tackling the problem in two ways; (i) is to come up with non von Neumann hardware platforms and (ii) adopt an architecture where the design and learning is cheap, simplified, robust and requires minimum training. The former is addressed as the unconventional computing<sup>30,31</sup> correlating to the natural computation emergent in everyday life examples and the latter can be overcome by the reservoir computing framework. Unconventional computing is way of using non-silicon devices that does not follow instructions by operating in logical '0' or '1'. It is more inclined

towards exploiting the intrinsic analog dynamics, natural to any biological, physical and chemical body, as output instructions when instigated by an external stimuli and then evolving them by controlled algorithms to solve a given problem statement. The term was first coined by Claude and Casti and is gaining popularity as an interdisciplinary research that holds immense potential to be a replacement for current von Neumann conventional structures. A few notable systems among the many which are currently being investigated includes DNA computing, quantum computing, optical computing, cellular automata, evolution in-materio and swarm intelligence.<sup>32–40</sup> A definitive set of algorithms, set-up for every system, is used to compute a given task. So in this context, we review the training technique of RC framework and discuss its unification with vivid dynamical physical systems, via literature reports, and see how well they stand out in the realm of unconventional computing as an efficient hardware implemented ANN approach for solving machine intelligent tasks.

### **1.5 Reservoir computing: A general overview**

Reservoir computing<sup>41–47</sup> is a class of recurrent neural networks where the learning framework is based on two architectures: an echo state network<sup>48–52</sup> and a liquid-state machine.<sup>53–57</sup> Fig. 1.5 characterized by a recurrently connected non-linear dynamical system acting as time-based memory cells. The overall framework consists of three layers: a time-varying input layer  $U(t)$ , a reservoir layer  $X(t)$ , and an output layer  $O(t)$ . The input perturbation produces reservoir states  $X_i(t)$  that evolve over time given by Eq. 1.1 where  $X_i(t)$  at each instant of time, is mostly a non-linear mapping of the current weighted input state  $U(t)$  and its recent past weighted state  $X_i(t-1)$ . The overall reservoir output  $z(t)$ , in contrast, is represented by the linear combinations of different reservoir states  $X_i(t)$  weighted with the output weights ' $W$ ' as given in Eq. 1.2.

$$X_i(t) = f(W_{in}U(t) + W_{res}X_i(t-1)) \quad (1.1)$$

$$z(t) = \sum_i W_i X_i(t) \quad (1.2)$$

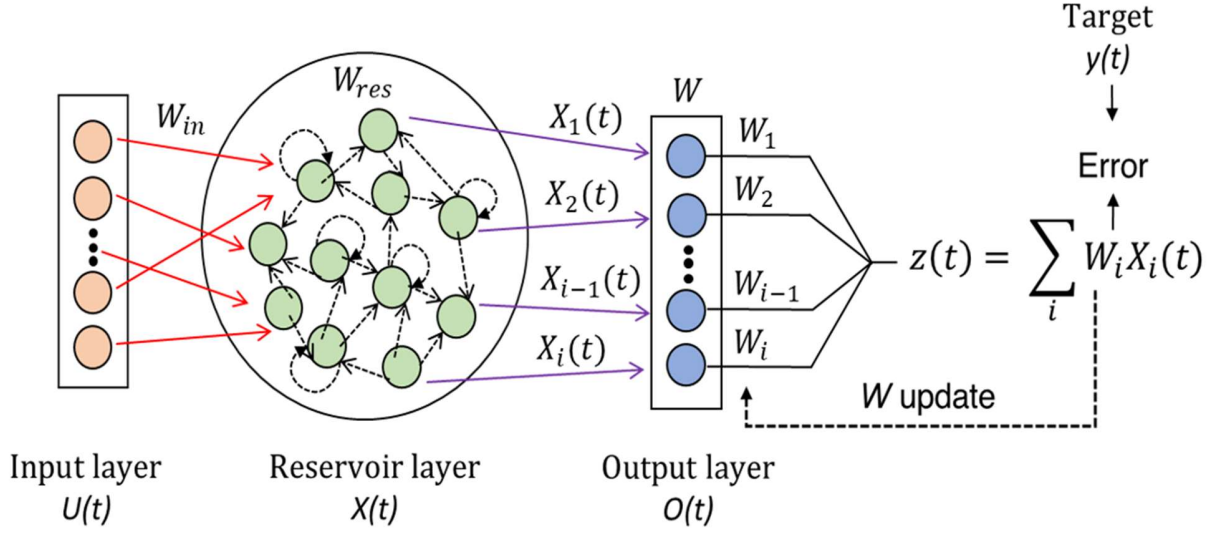


**Fig. 1.5** The schematic of reservoir computing architecture which includes an input layer  $U(t)$ , reservoir layer  $X(t)$ , and readout layer  $O(t)$ . The reservoir contains non-linear units (green circles) with recurrent connections (black dotted line).

Unlike MLP, CNN and RNN that requires training of multiple hidden layers, in RC, only the output layer undergoes supervised training<sup>58–62</sup> using a target signal  $y(t)$  with input weight  $W_{in}$  and the reservoir weight  $W_{res}$  being kept fixed. Successful training is achieved through minimization of the learning error via simultaneous upgradation of weight  $W$  over a simple regression model, thus paving for an efficient computation paradigm at the hardware level. For a system to qualify as the reservoir<sup>63,64</sup> it has to be (i) non-linear, as real world information are erratic and doesn't have a linear dependence on time, so non-linear dynamical systems are important; (ii) high dimensional,

this refers to the ability to produce multiple spatio-temporal sequences arising from different points of the system when perturbed by same input; (iii) echo state property/fading memory, which suggests that all reservoir states should respond the same way when stimulated by same input sequence irrespective of the initial state of the reservoir, and this is possible only when the reservoir remembers information about the recent past and forgets anything about the distant temporal sequence; (iv) input separability, reservoir outputs should not be the same for two different input sequences otherwise it will not be able to classify them. As the architecture and the training is simple, RC thus can be realized in an unconventional way by using physical dynamical systems instead of relying on the present day logical components. Since the physical phenomena arising from these materials can be used as high dimensional information data, hence they can be thought of as satisfactory components for administering in-materio RC.

### **1.6 A survey of physical reservoir devices**

Research in this area has been under constant progress, but owing to the abundance of materials present in nature the scope to explore is immense. Using this concept and the principles of liquid state machine, Fernando and Sojakka proposed a water bucket system for pattern recognition<sup>65</sup> and called it a ‘liquid brain’, Fig. 1.6a. Here they used wave ripples, generated by electrical motors, as the non-linear information processing, arising from wave interference, to achieve the tasks of speech recognition and XOR approximation. Kristof et al. in 2014 came up with the concept of RC on a silicon photonic chip,<sup>66</sup> Fig. 1.6b as optical based system promises a power efficient, lossless speedy data processing, important for handling big data in the context of machine intelligence. They designed a 16 node mesh reservoir in a 4x4 array on with passive silicon photonic chips consisting of waveguides, splitters and combiners. The nodes itself acted as linear units of superimposed amplitude signals of the input optics, but were post-processed to impose



non-linearity by reading out as power levels which were then trained off-line with regression to achieve the Boolean task of XOR with an error rate of as low as 5 %. Although first reports on photonics dates back to 2008 by Vondoorne et al., but subsequent progress since then have been on the go for various tasks of time series prediction and spoken digit recognition.<sup>67–72</sup>

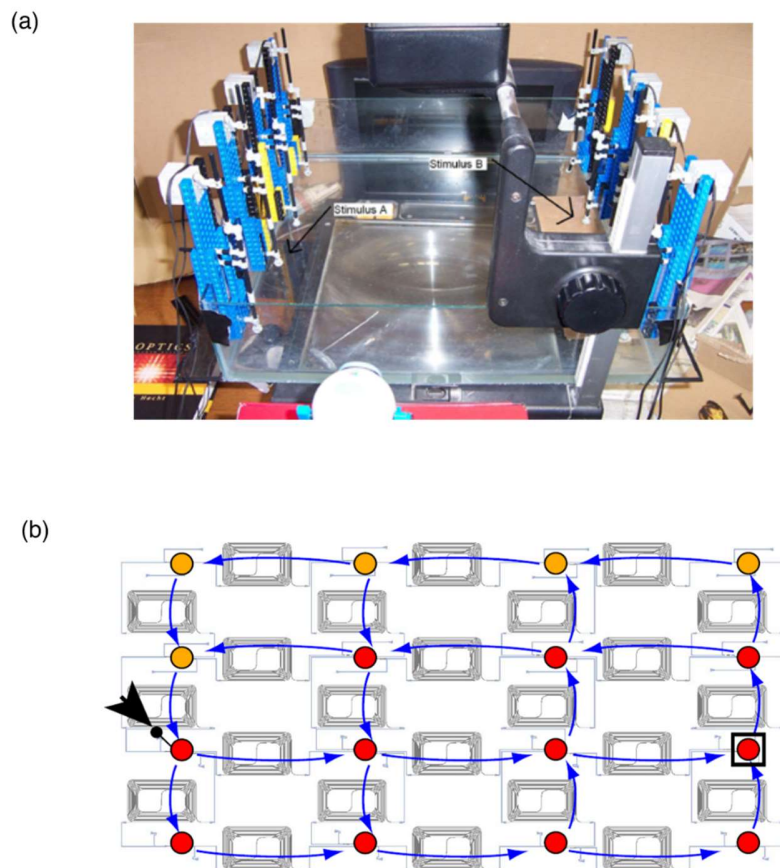


**Fig. 1.6** Physical reservoir systems. (a) The water bucket system called the ‘Liquid brain’.<sup>65</sup> (b) Design of our 16-node passive reservoir in 4\_4 configuration, overlain with the topology. All connections are bidirectional but by using one input (black arrow), the light flows according to the blue arrows. The 11 nodes marked with a red dot were measured.<sup>66</sup>

Other ultrafast non-linear dynamical system of interest consists of spintronic devices which uses both spin and charge to exchange information.<sup>73–81</sup> For example, Wencong et al. in 2019 displayed spintronic RC based on magnetic skyrmion (MS) and spin torque oscillators (STO) separately for different tasks, Fig. 1.7a. The MS made of Pt/Co ferromagnetic showed a non-linear motion under the influence of pulse current due to the non-linear dipole field and current induced spin-torque. The position at each time instant was recorded as the reservoir outputs from a series of pulse inputs originating in a hand written digit image. The outputs were trained off line and were then trained to classify each digit with an accuracy rate of greater than 80%. Similar to this, STO made of ferromagnetic layers were used as another RC device wherein their non-linear magnetic precision, a function of the input current amplitude, was exploited as reservoir outputs to construct NARMA 10 time series off-line with an accuracy of 85%, Fig. 1.7b. Significant research of RC implemented with memristive device is also well studied for temporal signal prediction, speech recognition, language learning and environmental sensing applications.<sup>73–75,82–85</sup> An example of one such memristive RC work was carried out by Chao et al.<sup>85</sup> where they proposed  $WO_x$  based system that utilizes the dynamics of non-linear filament formation, due to oxygen vacancies, and used those as reservoir outputs to optimize the weights for handwritten digit recognition with a very high classification accuracy.

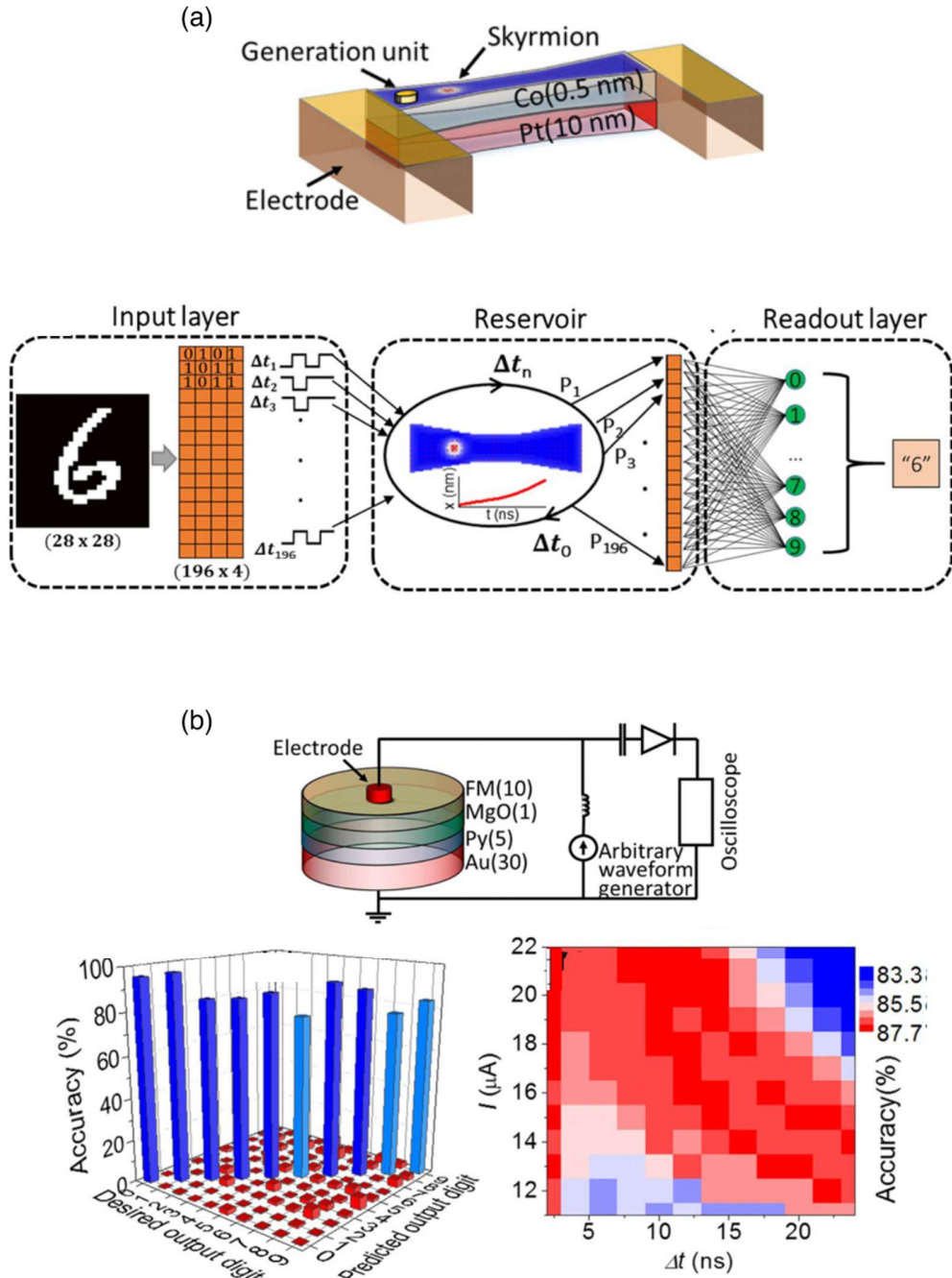


**Fig. 1.7** RC with spintronic. (a) Structure schematic of a magnetic skyrmion (MS) consisting of the dumbbell shape ferromagnetic Pt(10)/Co(0.5) bilayer (top). Process flow diagram of handwritten digit recognition using an MS-based RC system (bottom). (b) Schematic of a vortex-type STO and block diagram (top). Results of handwritten digit recognition using a RC system with one single STO (bottom).<sup>77</sup>

RC derived directly from body motion was recently evaluated by Nakajima et al. by using a soft robot arm<sup>86–92</sup> under water environment, shown in Fig. 1.8. The body dynamics recorded from different embedded sensors were taken as reservoir outputs when stimulated by an external input and was trained off-line to compute the time series task of NARMA 10.

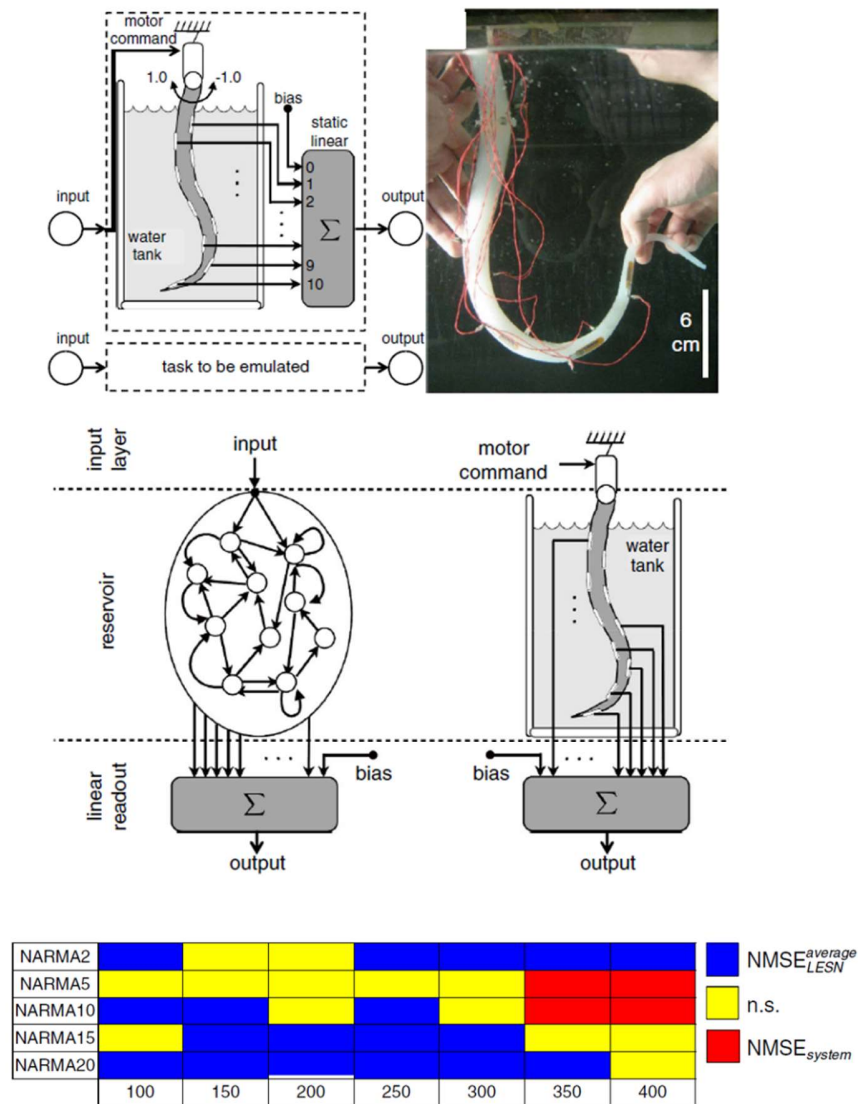
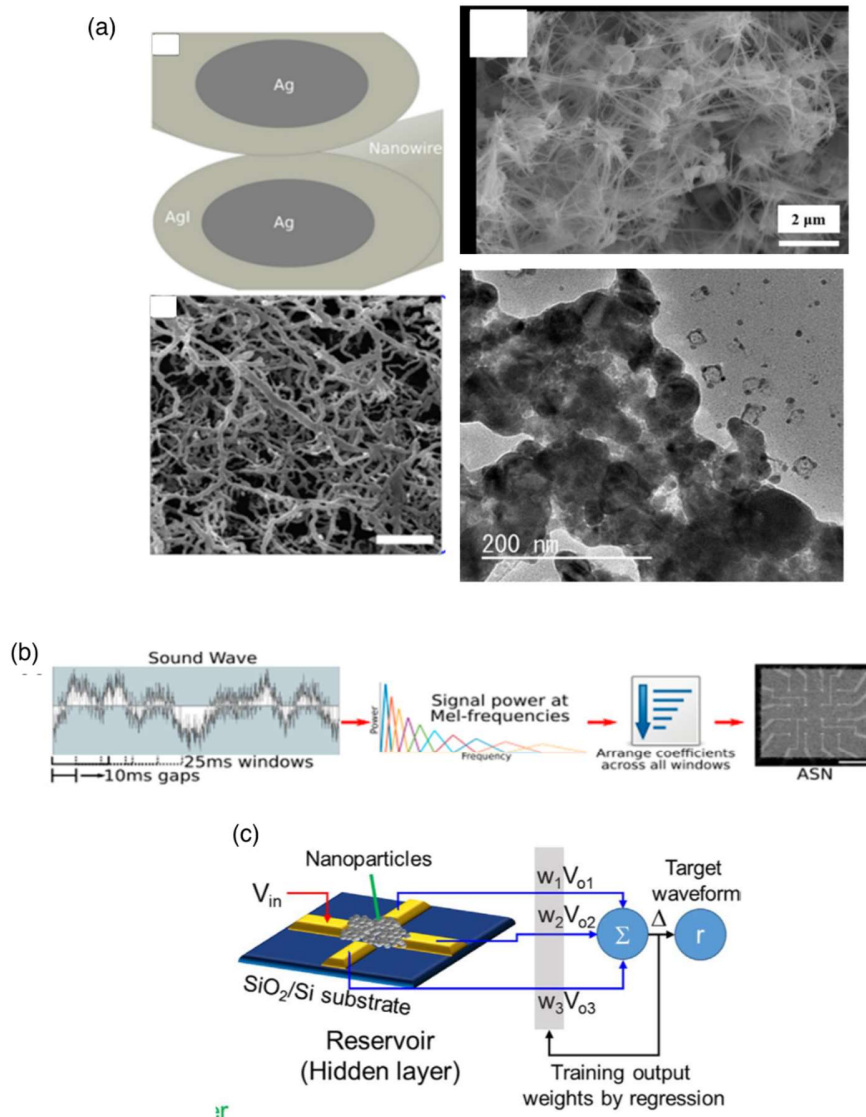


Fig. 1.8 RC with soft body. Platform setup for a soft silicone arm and schematics showing the information processing scheme using the arm (top). Diagram summarizing the significant differences between  $NMSE_{system}$  and  $NMSE_{LESN}$  (bottom).

RC based platform using atomic switch networks (ASN)<sup>93–95</sup> of Ag/Ag<sub>2</sub>S nanowire, Ag/Ag<sub>2</sub>Se nanowire, and Ag/Ag<sub>2</sub>S nanoparticles. Fig. 1.9a have also been demonstrated. Each of these systems were embedded on micro electrode arrays that allowed recording multiple voltage readouts of high dimensional dynamics to be trained for tasks like Boolean logic, voice classification, Fig. 1.9b, waveform generation, Fig. 1.9c, and frequency separation.



**Fig. 1.9** RC with atomic switch networks (ASN). (a) Shows Ag/AgI (left) nanowires, Ag/Ag<sub>2</sub>Se (top right) nanowires and Ag/Ag<sub>2</sub>S (bottom right) nanoparticle ASN systems.<sup>93–95</sup> (b) Voice classification task schematic.<sup>93</sup> (c) Waveform generation task schematic.<sup>95</sup>

### 1.7 RC with nano networks: A brain equivalent system

All the above systems show promising platforms for unconventional RC, but considering from the biological point of view, resemblance to brain like network structure is best replicated by the ASN's reported. The sheer advantage of ASN is the presence of inherent feedback loops, which are otherwise circuited for rest of the large RC systems making it cost ineffective. Moreover, the nanostructures have an upper hand when it comes to large scale integration on variable substrates making them architecturally more viable and compact when it comes to VLSI design. Although, ASN holds a remarkable position, but their non-linear dynamics is parameterized by a pre-condition of set threshold filament formation which might lead to some uncertainty within or among different devices. In terms of RC this is not a grave issue as the training only happens at output layer without worrying about the reservoir internal state, but nano-networks are not just limited to ASN. So, materials apart from ASN too should come in picture and in this regard the most prominent choice is the use of single walled carbon nanotube (SWNT). Unconventional computing with SWNT via evolutionary algorithm is very well reported in literature for solving many problems<sup>96–101</sup> but little is known about them being used for RC implementation. SWNT are rolled up graphene sheets that has a length of the order of  $\mu\text{m}$  and diameter of nm thus making them one dimensional nanomaterials with  $\pi$  conjugated benzene rings. The rolling up along the (n, m) indexes results in different chirality SWNT possessing either semiconducting or metallic properties as shown in Fig. 1.10a and hence can show excellent electrical, mechanical and thermal properties.<sup>102</sup> Recent reports have shown that the conductive states of SWNT can be modulated by covalent/non-covalent functionalization with different molecules resulting in non-linear dynamics emerging from charge transfer (CT) mechanisms.<sup>103–107</sup> One such CT arises from molecules having redox properties like polyoxometalates (POM).<sup>108,109</sup> POM are polyatomic anions that contains

transition metal oxyanions linked together via shared oxygen atoms to form a 3D framework cage with collective electrical, magnetic and optical properties.<sup>33,110–113</sup> Depending upon their co-ordination number ( $c_n$ ) they can be classified into Keggin and Dawson type ( $c_n = 4$ , tetrahedral) or Anderson type ( $c_n = 6$ , octahedral) as shown in Fig. 1.10b. They have a rich chemistry due to presence of numerous transition metals that possess multiple redox states and hence can undergo step wise charge discharge reactions facilitating the CT process.

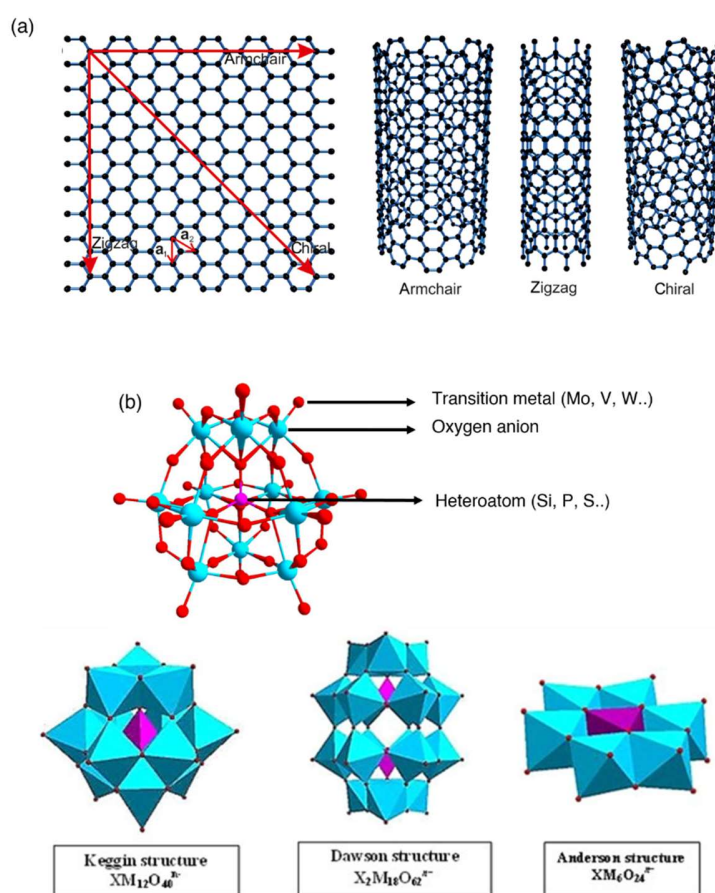


**Fig. 1.10** The single walled carbon nanotube (SWNT) and polyoxometalate (POM). (a) Graphene sheets rolled up along the (n,m) indices to give different configuration SWNT like zigzag, armchair and chiral.<sup>114</sup> (b) The 3D framework of POM with the respective molecules (top). The different POM classes based on their co-ordination number (bottom)<sup>115</sup>

SWNT/POM have been majorly used in the field of catalysis or supercapacitors due to this property,<sup>116,117</sup> but recently this conventional idea was changed, when Tanaka et al. showed that a system of SWNT/POM, Fig. 1.11a, can be used to develop a neuromorphic system that behaved exactly like the spiking neurons.<sup>118</sup> They used phosphomolybdic acid to be non-covalently adsorbed on the SWNT surface and produced a thin film network sandwiched between parallel electrodes. Upon passing electrical stimuli of varying voltages, noise like fluctuations in lower voltage regime changed to higher spike like signals gradually, Fig. 1.11b. Such spiking behavior was attributed to be an equivalent analogue of negative differential resistance (NDR) peak found in the current-voltage curve. The correlation was validated theoretically by a cellular automata model, Fig. 1.11d, where it was confirmed that both the behavior shared the same source of threshold charge-discharge phenomena arising due to the redox property of POM. When instigated by an input bias, charge accumulation starts to happen at the POM molecules which gives rise to such fluctuations initially, but with increasing bias this charge storage can then reach a threshold for one of the POM molecules thereby undergoing sudden discharge through SWNT channels giving such spike or NDR signals. The research work stands out in the way that, SWNT devices before have been shown to behave as synaptic devices<sup>119,120</sup> but never has it been exploited for neuronal properties with just molecular adsorption.



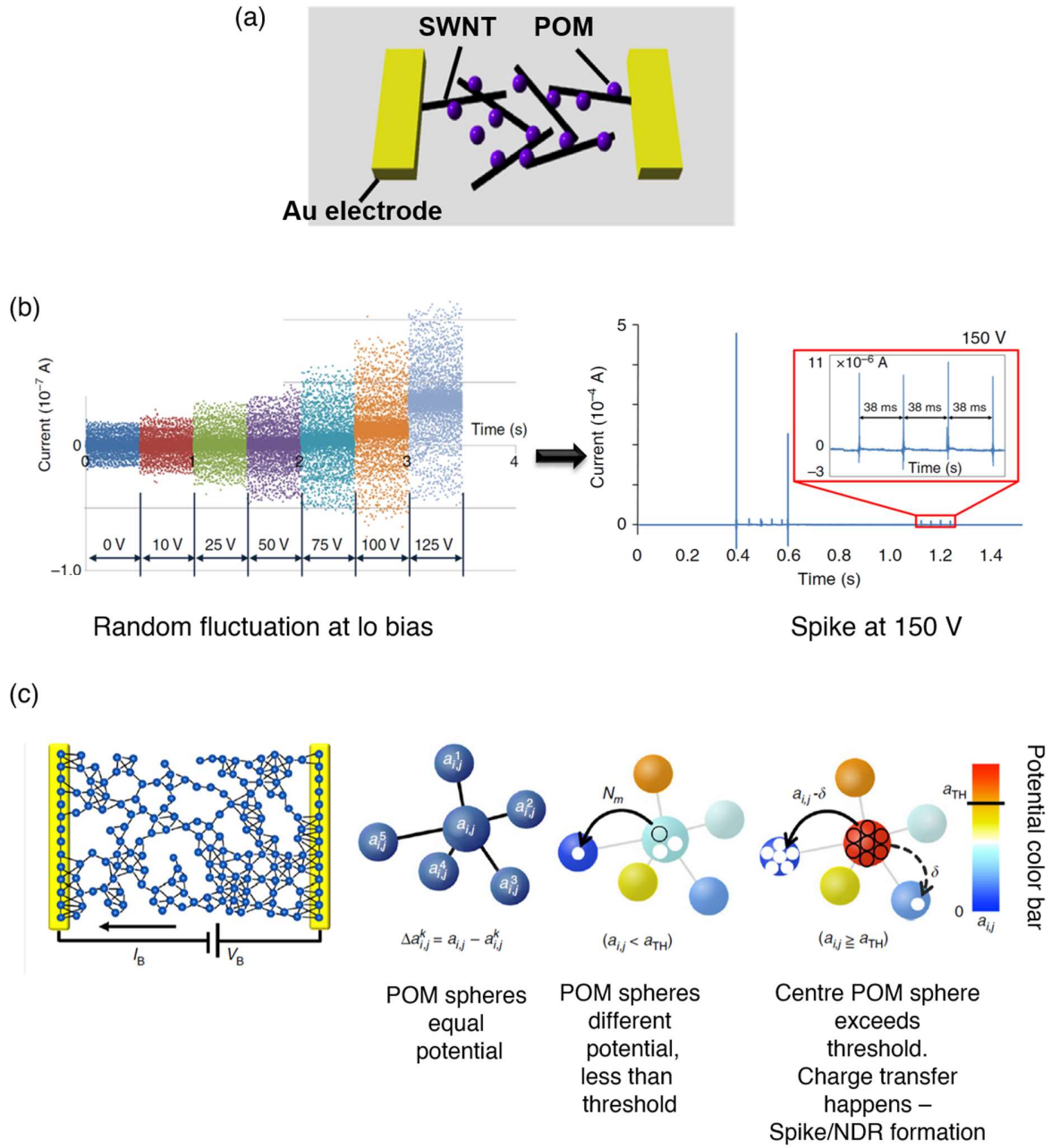


**Fig. 1.11** The spiking neuromorphic behavior of SWNT/POM complex. (a) Network of SWNT/POM between parallel plate electrodes. (b) Random fluctuation at low bias changing to spike at 150 V. (c) Step-wise threshold charge-discharge mechanism for spiking/NDR behavior modelled with cellular automata architecture.<sup>118</sup>

Now spiking events are mostly considered as single point gating effect originating from generation-recombination processes. The SWNT/POM in between the parallel plate capacitor replicates such point gates, but when randomly arranged can result in higher degree of interconnected networks leading to a cumulative signal transfer, hence averaging out the spiking nature to give mostly random fluctuations like brain (see Fig.1.4a). Based on this concept, in the same paper<sup>118</sup> a theoretical model of RC architecture with SWNT/POM was introduced. They showed clearly that by exploiting the voltage output readouts from various points in the network and applying an off-line FORCE training, Fig. 1.12a-b, a higher order time series target signal of NARMA-10 can be constructed with excellent accuracy, Fig. 1.12c-d. The report is the first instance on SWNT/POM unconventional RC where no precondition is required for random filament formation or generating non-linearity but rather utilizes the intrinsic random noise generated from the redox behavior as non-linear high dimensional dynamics to incorporate such an in-materio RC.

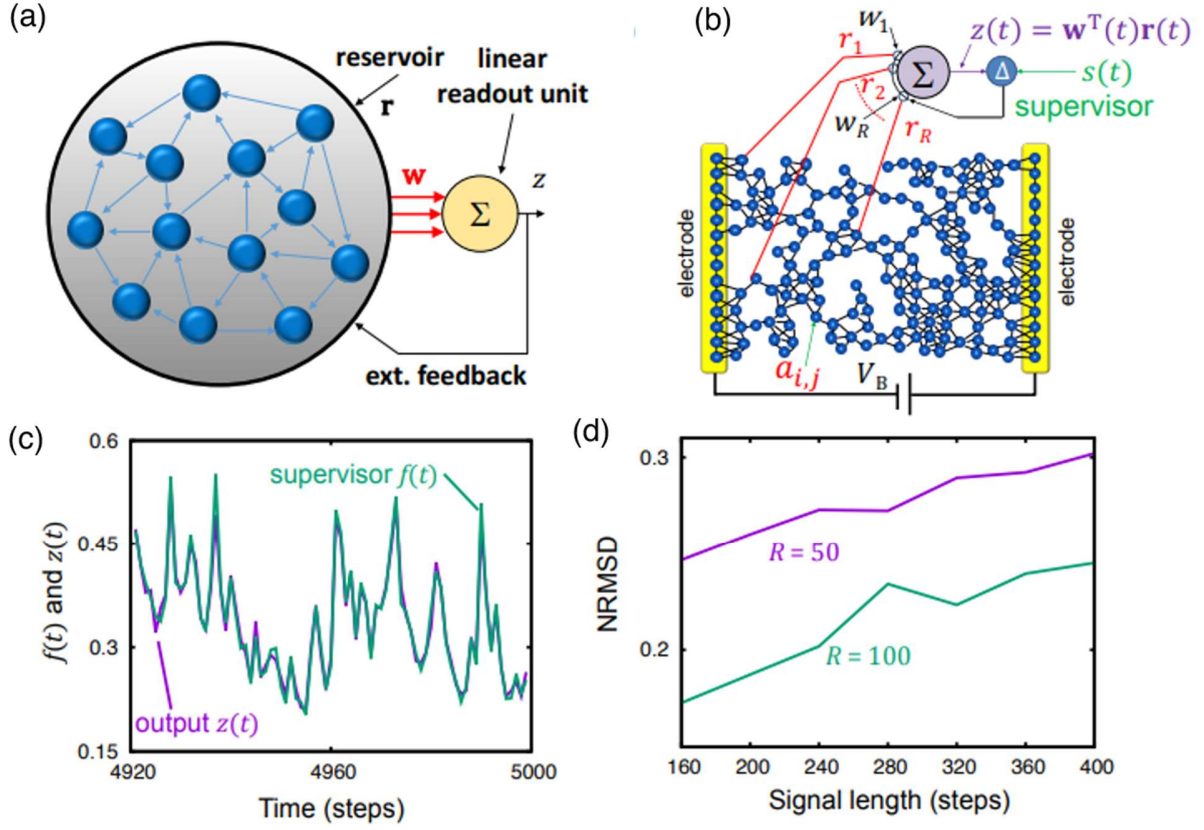


**Fig. 1.12** Demonstration of RC with SWNT/POM complex. (a) Basic schematic of RC architecture. (b) Theoretical model constructed from SWNT/POM random network where each node (blue sphere POM) acts a source of information connected via recurrent connection (black line SWNT). A supervised learning algorithm is implemented to teach the reservoir outputs  $z(t)$  a given target  $s(t)$ . (c) The successful NARMA-10 task replicated after training. (d) Device performance measured in terms of normalized root mean square deviation (NRMSD) for different number of node readouts.<sup>118</sup>

## 1.8 Problem statement

The present work is aimed at expanding the theoretical idea of SWNT/POM reservoir to a real substrate platform and investigate the reservoir properties along with testing the device for in-materio RC for various benchmark tasks. To do this, we first fixate our material to an organic functionalized porphyrin polyoxometalate (Por-POM), the chemical formula of which is  $SV_2W_{10}O_{40}[H_4TPP]$ . The Por-POM have shown potential application in the field of spike based neuromorphic behavior,<sup>121</sup> but their use as a material oriented RC has never been discussed before. The presence of an extra porphyrin  $\pi$  benzene ring makes them highly non-linear with NDR like current fluctuation due to their charge transfer from the porphyrin to POM.<sup>122,123</sup> Moreover a facile non-covalent adsorption on the SWNT is possible just by sonication for a shorter time due to the possibility of  $\pi$ - $\pi$  interaction. The second focus is given on choosing a well fabricated substrate that will not only allow for an easy thin film transfer of the SWNT/Por-POM complex but should also interface with a hardware and PC platform by avoiding excessive circuitry. After deciding on the synthesis, fabrication and hardware built up we dedicate our concern towards developing strategies and experiments through survey of literature reports to help confer the reservoir properties our device holds as this is important to formulate the RC tasks it will be able to perform. Lastly, we proceed to select definitive RC tasks and using the correct off-line training algorithm we train the device for specific targets and then evaluate the device's performance on other test datasets to prove its capability for in-materio RC.

## **1.9 Objective study**

The main aims of this research is as follows:

1. Synthesize the SWNT/Por-POM complex following a simple procedure.
2. Build and fabricate a multi-electrode array.
3. Test the device dynamics and its reservoir properties initially.
4. Move on to conduct benchmark tasks related to the reservoir properties found.
5. To find a validation behind each of the task the device performed.
6. To show that it has a resemblance to brain like information processing.
7. To study the effect of training time and training outputs.

## **1.10 Research scope**

The scope of this research is focused mainly on establishing RC with a dynamical system of SWNT/Por-POM. So, the main areas covered will be dedicated to

1. Establishing the MEA architecture via photolithography, which is cheap and non-complicated. The MEA is chosen as it gives us an easy way to read multiple voltage readouts from different regions of the material similar just like reading nerve cell activities using an EEG machine.
2. Interface the MEA to hardware which will control all the input-output signals given or readout from the device, which can finally be utilized for an off-line supervised training.
3. Confirm the reservoir property by analyzing a simple function approximation, containing non-linear and memory parameters, which will reflect on the device's extent for a particular kind of RC task.

4. Choose three tasks of waveform generation-single input-output learning, Boolean optimization – two input-one output problem and one-hot vector object classification, two input-two output binary classifier.

### **1.11 Outline of the thesis**

The thesis consists of seven chapters in total. Chapter 1 starts off with a general introduction that summarizes the contents of the section. A highlight is given between the brain and von Neumann architecture followed by historical evolution of artificial neural networks and their usage in conventional computer. The drawbacks are discussed and the solution for in-materio reservoir computing approach is mentioned. Finally the idea motivation and scope of this work is detailed. Chapter 2 begins with the repository of materials used in a tabulated form. Briefing regarding synthesis procedure, fabrication method, and custom built hardware and characterization methods with their respective working principle is given. Chapter 3 uses these characterization techniques to confirm the synthesis and show the random network structure present in our device akin to the brain connectivity. It goes on to discuss the important property of memory-non linearity trade off and confirms that the device is best suited for non-linear task rather than memory through current-voltage and low memory capacity experiments. It also reflects on the maximized information processing via the FFT studies of temporal current dynamics. Chapter 4, 5 and 6 discusses the RC benchmark tasks of waveform generation, Boolean logic optimization and one-hot vector object classification with briefing on the reasons behind the performances. Chapter 7 gives an overview of a possible future scope the SWNT/Por-POM holds for computing other memory tasks and gives the concluding remarks.

## 1.12 References

1. Hameroff, S. R. The brain is both neurocomputer and quantum computer. *Cogn. Sci.* **31**, 1035–1045 (2007).
2. Legenstein, R. & Maass, W. What Makes a Dynamical System Computationally Powerful? in *New Directions in Statistical Signal Processing: From Systems to Brain* (MIT Press, 2007). doi:10.7551/mitpress/4977.003.0008
3. Liu, Y. H. & Wang, X. J. Spike-frequency adaptation of a generalized leaky integrate-and-fire model neuron. *J. Comput. Neurosci.* **10**, 25–45 (2001).
4. Golio, M. Fifty Years of Moore's Law. *Proc. IEEE* **103**, 1932–1937 (2015).
5. 3. Brain Computer.pdf.
6. Huang, A., Zhang, X., Li, R. & Chi, Y. Memristor Neural Network Design. *Memristor and Memristive Neural Networks* (2018). doi:10.5772/intechopen.69929
7. Eeckhout, L. Is Moore's Law Slowing Down? What's Next? *IEEE Micro* **37**, 4–5 (2017).
8. In, S.  $t M(t) = \sum M_0$ . 191–196 (2008).
9. Rosenblatt, F. The perceptron: A probabilistic model for information storage and organization in the brain. *Psychol. Rev.* **65**, 386–408 (1958).
10. Brown, R. E. Donald O. Hebb and the Organization of Behavior: 17 years in the writing. *Mol. Brain* **13**, 1–28 (2020).
11. Widrow, B. & Lehr, M. A. 30 Years of Adaptive Neural Networks: Perceptron, Madaline, and Backpropagation. *Proc. IEEE* **78**, 1415–1442 (1990).

12. Minsky, M. L. & Papert, S. A. Perceptrons. (1988).
13. Rumelhart, D. E. & Hinton, G. E. Learning Representations by Back-Propagating Errors. *Cogn. Model.* 3–6 (2019). doi:10.7551/mitpress/1888.003.0013
14. Alsmadi, M. K., Omar, K. Bin, Noah, S. A. & Almarashdah, I. Performance comparison of multi-layer perceptron (Back Propagation, Delta Rule and Perceptron) algorithms in neural networks. *2009 IEEE Int. Adv. Comput. Conf. IACC 2009* 7, 296–299 (2009).
15. Noriega, L. Multilayer perceptron tutorial. *Sch. Comput. Staff. Univ.* 1–12 (2005).
16. Ramchoun, H., Amine, M., Idrissi, J., Ghanou, Y. & Ettaouil, M. Multilayer Perceptron: Architecture Optimization and Training. *Int. J. Interact. Multimed. Artif. Intell.* 4, 26 (2016).
17. Hornik, K. Approximation capabilities of multilayer feedforward networks. *Neural Networks* 4, 251–257 (1991).
18. Deba0, C. Degree of approximation by superpositions of a sigmoidal function. *Approx. Theory its Appl.* 9, 17–28 (1993).
19. Basu, J. K., Bhattacharyya, D. & Kim, T. Use of Artificial Neural Network in Pattern Recognition. *Int. J. Softw. Eng. its Appl.* 4, 23–34 (2010).
20. Botalb, A., Moinuddin, M., Al-Saggaf, U. M. & Ali, S. S. A. Contrasting Convolutional Neural Network (CNN) with Multi-Layer Perceptron (MLP) for Big Data Analysis. *Int. Conf. Intell. Adv. Syst. ICIAS 2018* 1–5 (2018). doi:10.1109/ICIAS.2018.8540626
21. Ingwersen, P., Kaae, S. & Kajberg, L. Letter from Copenhagen. *J. Inf. Sci.* 1, 63–66 (1979).



22. Lecun, Y., Bengio, Y. & Hinton, G. Deep learning. *Nature* **521**, 436–444 (2015).
23. Yuan, Z.-W. & Zhang, J. Feature extraction and image retrieval based on AlexNet. *Eighth Int. Conf. Digit. Image Process. (ICDIP 2016)* **10033**, 100330E (2016).
24. Alom, M. Z. *et al.* The History Began from AlexNet: A Comprehensive Survey on Deep Learning Approaches. (2018).
25. Ponce, P., Molina, A., C., D. & Grammatikou, D. Brain Computer Interfaces for Cerebral Palsy. *Cereb. Palsy - Challenges Futur.* (2014). doi:10.5772/57084
26. Bahá'u'lláh, 1817-1892. The Kitab-I-Aqdas. **59**, 258 (2007).
27. P.J. Werbos. Backpropagation Through Time: What It Does and How to Do It. *Proceedings of the IEEE* **78**, 1550–1560 (1990).
28. Schuman, C. D. *et al.* A Survey of Neuromorphic Computing and Neural Networks in Hardware. *arXiv* 1–88 (2017).
29. Dongarra, J. Report on the Fujitsu Fugaku System. *Hilos Tensados* **1**, 1–476 (2020).
30. Ziegler, M. Novel hardware and concepts for unconventional computing. *Sci. Rep.* **10**, 10–12 (2020).
31. Adamatzky, A. *et al.* East-West paths to unconventional computing. *Prog. Biophys. Mol. Biol.* **131**, 469–493 (2017).
32. Parpinelli, R. S. & Lopes, H. S. New inspirations in swarm intelligence: A survey. *Int. J. Bio-Inspired Comput.* **3**, 1–16 (2011).

33. Li, S. S., Long, G. L., Bai, F. S., Feng, S. L. & Zheng, H. Z. Quantum computing. *Proc. Natl. Acad. Sci. U. S. A.* **98**, 11847–11848 (2001).
34. Solli, D. R. & Jalali, B. Analog optical computing. *Nat. Photonics* **9**, 704–706 (2015).
35. Miller, J. F., Harding, S. L. & Tufte, G. Evolution-in-materio: Evolving computation in materials. *Evol. Intell.* **7**, 49–67 (2014).
36. Miller, J. F. & Downing, K. Evolution in materio: Looking beyond the silicon box. *Proc. - NASA/DoD Conf. Evolvable Hardware, EH 2002-Janua*, 167–176 (2002).
37. Bose, S. K. *et al.* Evolution of a designless nanoparticle network into reconfigurable Boolean logic. *Nat. Nanotechnol.* **10**, 1048–1052 (2015).
38. Wolfarm, S. Cellular automata: a model of complexity. *Nature* **31**, 419–424 (1984).
39. Kari, L. DNA computing: Arrival of biological mathematics. *Math. Intell.* **19**, 9–22 (1997).
40. Ezziane, Z. DNA computing: Applications and challenges. *Nanotechnology* **17**, (2006).
41. Konkoli, Z. Reservoir Computing. *Encycl. Complex. Syst. Sci.* 1–12 (2017).  
doi:10.1007/978-3-642-27737-5\_683-1
42. Mosleh, S. S., Liu, L., Sahin, C., Zheng, Y. R. & Yi, Y. Brain-Inspired Wireless Communications: Where Reservoir Computing Meets MIMO-OFDM. *IEEE Trans. Neural Networks Learn. Syst.* **29**, 4694–4708 (2018).
43. Butcher, J. B., Verstraeten, D., Schrauwen, B., Day, C. R. & Haycock, P. W. Reservoir computing and extreme learning machines for non-linear time-series data analysis. *Neural Networks* **38**, 76–89 (2013).

44. Gallicchio, C., Micheli, A. & Pedrelli, L. Deep reservoir computing: A critical experimental analysis. *Neurocomputing* **268**, 87–99 (2017).
45. Seoane, L. F. Evolutionary aspects of reservoir computing. *Philos. Trans. R. Soc. B Biol. Sci.* **374**, (2019).
46. Schrauwen, B., Verstraeten, D. & Van Campenhout, J. An overview of reservoir computing: Theory, applications and implementations. in *ESANN 2007 Proceedings - 15th European Symposium on Artificial Neural Networks* 471–482 (2007).
47. Lukosevicius, M., Jaeger, H. & Schrauwen, B. Reservoir Computing Trends. *Kunstl Intell* **26**, 365–371 (2012).
48. Gallicchio, C. & Micheli, A. Echo State Property of Deep Reservoir Computing Networks. *Cognit. Comput.* **9**, 337–350 (2017).
49. Jaeger, H. Discovering multiscale dynamical features with hierarchical Echo State Networks. *Jacobs Univ. Bremen, Tech. Rep* 1–30 (2007).
50. Jaeger, H. Short term memory in echo state networks. *GMD Rep.* **152** 60 (2002).
51. Jaeger, H. & Haas, H. Harnessing Nonlinearity: Predicting Chaotic Systems and Saving Energy in Wireless Communication. *Science (80-. ).* **304**, 78–80 (2004).
52. Jaeger, H. The “echo state” approach to analysing and training recurrent neural networks – with an Erratum note 1. *GMD Rep.* 1–47 (2010).
53. Wojcik, G. M. & Kaminski, W. A. Liquid state machine and its separation ability as function of electrical parameters of cell. *Neurocomputing* **70**, 2593–2597 (2007).

54. Grzyb, B. J., Chinellato, E., Wojcik, G. M. & Kaminski, W. A. Which model to use for the Liquid State Machine? *Proc. Int. Jt. Conf. Neural Networks* 1018–1024 (2009).  
doi:10.1109/IJCNN.2009.5178822
55. Verstraeten, D., Schrauwen, B., Stroobandt, D. & Van Campenhout, J. Isolated word recognition with the Liquid State Machine: A case study. *Inf. Process. Lett.* **95**, 521–528 (2005).
56. Yamazaki, T. & Tanaka, S. The cerebellum as a liquid state machine. *Neural Networks* **20**, 290–297 (2007).
57. Maass, W. Chapter 8 Liquid State Machines : Motivation , Theory , and Applications. 275–296
58. Ferreira, A. A. & Ludermir, T. B. Genetic Algorithm for reservoir computing optimization. *Proc. Int. Jt. Conf. Neural Networks* 811–815 (2009).  
doi:10.1109/IJCNN.2009.5178654
59. Dutoit, X. *et al.* Pruning and regularization in reservoir computing. *Neurocomputing* **72**, 1534–1546 (2009).
60. Grigoryeva, L. & Ortega, J. P. Differentiable reservoir computing. *J. Mach. Learn. Res.* **20**, 1–62 (2019).
61. Verstraeten, D., Schrauwen, B., D’Haene, M. & Stroobandt, D. An experimental unification of reservoir computing methods. *Neural Networks* **20**, 391–403 (2007).
62. Lukoševičius, M. & Jaeger, H. Reservoir computing approaches to recurrent neural network training. *Comput. Sci. Rev.* **3**, 127–149 (2009).

63. Nakajima, K. Physical reservoir computing-an introductory perspective. *Jpn. J. Appl. Phys.* **59**, (2020).
64. Tanaka, G. *et al.* Recent advances in physical reservoir computing: A review. *Neural Networks* **115**, 100–123 (2019).
65. Sojakka, C. F. and S. Pattern Recognition in a Bucket. *Am. J. Clin. Pathol.* **86**, 688–689 (1986).
66. Vandoorne, K. *et al.* Experimental demonstration of reservoir computing on a silicon photonics chip. *Nat. Commun.* **5**, 1–6 (2014).
67. Salehi, M. R. & Dehyadegari, L. Optical signal processing using photonic reservoir computing. *J. Mod. Opt.* **61**, 1442–1451 (2014).
68. Duport, F., Schneider, B., Smerieri, A., Haelterman, M. & Massar, S. All-optical reservoir computing. **20**, 1958–1964 (2012).
69. Duport, F., Smerieri, A., Akrou, A., Haelterman, M. & Massar, S. Fully analogue photonic reservoir computer. *Sci. Rep.* **6**, 1–12 (2016).
70. Van Der Sande, G., Brunner, D. & Soriano, M. C. Advances in photonic reservoir computing. *Nanophotonics* **6**, 561–576 (2017).
71. Larger, L. *et al.* Photonic information processing beyond Turing: an optoelectronic implementation of reservoir computing. *Opt. Express* **20**, 3241 (2012).
72. Takano, K. *et al.* Compact reservoir computing with a photonic integrated circuit. *Opt. Express* **26**, 29424 (2018).

73. Sun, L. *et al.* In-sensor reservoir computing for language learning via two-dimensional memristors. *Sci. Adv.* **7**, (2021).
74. Athanasiou, V. & Konkoli, Z. On using reservoir computing for sensing applications: exploring environment-sensitive memristor networks. *Int. J. Parallel, Emergent Distrib. Syst.* **33**, 367–386 (2018).
75. Marinella, M. J. & Agarwal, S. Efficient reservoir computing with memristors. *Nat. Electron.* **2**, 437–438 (2019).
76. Kulkarni, M. S. Memristor-based Reservoir Computing. 226–232 (2012).
77. Jiang, W. *et al.* Physical reservoir computing using magnetic skyrmion memristor and spin torque nano-oscillator. *Appl. Phys. Lett.* **115**, (2019).
78. Tsunegi, S. *et al.* Physical reservoir computing based on spin torque oscillator with forced synchronization. *Appl. Phys. Lett.* **114**, (2019).
79. Chęciński, J. Synchronization properties and reservoir computing capability of hexagonal spintronic oscillator arrays. *J. Magn. Magn. Mater.* **513**, 1–6 (2020).
80. Nomura, H. *et al.* Reservoir computing with dipole-coupled nanomagnets. *Jpn. J. Appl. Phys.* **58**, (2019).
81. Jiang, W. *et al.* Physical reservoir computing built by spintronic devices for temporal information processing. *arXiv* **192403**, (2019).
82. Zhong, Y. *et al.* Dynamic memristor-based reservoir computing for high-efficiency temporal signal processing. *Nat. Commun.* **12**, 1–9 (2021).

83. Moon, J. *et al.* Temporal data classification and forecasting using a memristor-based reservoir computing system. *Nat. Electron.* **2**, 480–487 (2019).
84. Midya, R. *et al.* Reservoir Computing Using Diffusive Memristors. *Adv. Intell. Syst.* **1**, 1900084 (2019).
85. Du, C. *et al.* Reservoir computing using dynamic memristors for temporal information processing. *Nat. Commun.* **8**, 1–10 (2017).
86. Nakajima, K. *et al.* A soft body as a reservoir: Case studies in a dynamic model of octopus-inspired soft robotic arm (11916 words). *Front. Comput. Neurosci.* **7**, 1–19 (2013).
87. Nakajima, K., Hauser, H., Li, T. & Pfeifer, R. Exploiting the dynamics of soft materials for machine learning. *Soft Robot.* **5**, 339–347 (2018).
88. Horii, Y. *et al.* Physical reservoir computing in a soft swimming robot. (2019).
89. Li, T. *et al.* From the octopus to soft robot control: An octopus inspired behaviour control architecture for soft robots. *Vie Milieu* **61**, 211–217 (2011).
90. Bhovad, P. & Li, S. Physical reservoir computing with origami and its application to robotic crawling. *Sci. Rep.* **11**, 1–18 (2021).
91. Li, T., Nakajima, K., Cianchetti, M., Laschi, C. & Pfeifer, R. Behavior switching using reservoir computing for a soft robotic arm. *Proc. - IEEE Int. Conf. Robot. Autom.* **1**, 4918–4924 (2012).
92. Nakajima, K., Hauser, H., Li, T. & Pfeifer, R. Information processing via physical soft body. *Sci. Rep.* **5**, 1–11 (2015).

93. Lilak, S. *et al.* Spoken Digit Classification by In-Materio Reservoir Computing With Neuromorphic Atomic Switch Networks. *Front. Nanotechnol.* **3**, 1–11 (2021).
94. Kotooka, T. *et al.* Ag<sub>2</sub>Se Nanowire Network as an Effective In-Materio Reservoir Computing Device. 1–20 doi:10.21203/rs.3.rs-322405/v1
95. Hadiyawarman *et al.* Performance of Ag-Ag<sub>2</sub>S core-shell nanoparticle-based random network reservoir computing device. *Jpn. J. Appl. Phys.* **60**, (2021).
96. Mohid, M. & Miller, J. F. Evolving Robot Controllers Using Carbon Nanotubes. 106–113 (2015). doi:10.7551/978-0-262-33027-5-ch025
97. Clegg, K. D., Miller, J. F., Massey, M. K. & Petty, M. C. Practical issues for configuring carbon nanotube composite materials for computation. *IEEE SSCI 2014 - 2014 IEEE Symp. Ser. Comput. Intell. - IEEE ICES 2014 IEEE Int. Conf. Evolvable Syst. Proc.* 61–68 (2014). doi:10.1109/ICES.2014.7008723
98. Clegg, K. D., Miller, J. F., Massey, K. & Petty, M. Travelling salesman problem solved ‘in materio’ by evolved carbon nanotube device. *Lect. Notes Comput. Sci. (including Subser. Lect. Notes Artif. Intell. Lect. Notes Bioinformatics)* **8672**, 692–701 (2014).
99. Dale, M., Miller, J. F., Stepney, S. & Trefzger, M. A. Evolving carbon nanotube reservoir computers. in *Unconventional Computation and Natural Computation: 15th International Conference, UCNC 2016* (eds. Amos, M. & Condon, A.) 49–61 (Springer, 2016). doi:10.1007/978-3-319-41312-9\_5
100. Massey, M. K. *et al.* Computing with carbon nanotubes: Optimization of threshold logic gates using disordered nanotube/polymer composites. *J. Appl. Phys.* **117**, 134903 (2015).



101. Mohid, M. *et al.* Evolution-in-materio: solving computational problems using carbon nanotube–polymer composites. *Soft Comput.* **20**, 3007–3022 (2016).
102. Ganesh, E. N. Single Walled and Multi Walled Carbon Nanotube Structure. *Synth. Appl.* **2**, 311–320 (2013).
103. Inoue, S., Kokabu, T. & Matsumura, Y. Effects of physical and chemical adsorption on the electric conductance of carbon nanotube films. *AIP Adv.* **8**, 1–7 (2018).
104. Shim, M. Electrochemical gating and molecular adsorption on carbon nanotubes. *Phys. Chem. Interfaces Nanomater. IV* **5929**, 592913 (2005).
105. Tanaka, H. *et al.* Method for Controlling Electrical Properties of Single-Layer Graphene Nanoribbons via Adsorbed Planar Molecular Nanoparticles. *Sci. Rep.* **5**, (2015).
106. Subramaniam, C. *et al.* Visible fluorescence induced by the metal semiconductor transition in composites of carbon nanotubes with noble metal nanoparticles. *Phys. Rev. Lett.* **99**, 1–4 (2007).
107. Tanaka, H. *et al.* Influence of nanoparticle size to the electrical properties of naphthalenediimide on single-walled carbon nanotube wiring. *Nanotechnology* **23**, (2012).
108. Bosch-Navarro, C. *et al.* Charge transfer interactions in self-assembled single walled carbon nanotubes/Dawson-Wells polyoxometalate hybrids. *Chem. Sci.* **5**, 4346–4354 (2014).
109. Wen, S. *et al.* Theoretical insights into [PMo12O40]3- grafted on single-walled carbon nanotubes. *Phys. Chem. Chem. Phys.* **15**, 9177–9185 (2013).

110. Gumerova, N. I. & Rompel, A. Synthesis, structures and applications of electron-rich polyoxometalates. *Nat. Rev. Chem.* **2**, (2018).
111. Long, D. L. & Cronin, L. Towards polyoxometalate-integrated nanosystems. *Chem. - A Eur. J.* **12**, 3698–3706 (2006).
112. Kee, H. L. & Tang, H. Domestic Value Added in Chinese Exports : Firm-level Evidence. *Angew. Chemie - Int. Ed.* **30**, 34 (2013).
113. Coronado, E. & Gómez-García, C. J. Polyoxometalate-based molecular materials. *Chem. Rev.* **98**, 273–296 (1998).
114. Bocko, J., Lengvarský, P., Hunady, R. & Šarloši, J. The computation of bending eigenfrequencies of single-walled carbon nanotubes based on the nonlocal theory. *Mech. Sci.* **9**, 349–358 (2018).
115. Dehghani, R., Aber, S. & Mahdizadeh, F. Polyoxometalates and Their Composites as Photocatalysts for Organic Pollutants Degradation in Aqueous Media—A Review. *Clean - Soil, Air, Water* **46**, (2018).
116. Chen, H. Y. *et al.* A novel SWCNT-polyoxometalate nanohybrid material as an electrode for electrochemical supercapacitors. *Nanoscale* **7**, 7934–7941 (2015).
117. Toma, F. M. *et al.* Efficient water oxidation at carbon nanotube-polyoxometalate electrocatalytic interfaces. *Nat. Chem.* **2**, 826–831 (2010).
118. Tanaka, H. *et al.* A molecular neuromorphic network device consisting of single-walled carbon nanotubes complexed with polyoxometalate. *Nat. Commun.* **9**, 1–7 (2018).

119. Sanchez Esqueda, I. *et al.* Aligned Carbon Nanotube Synaptic Transistors for Large-Scale Neuromorphic Computing. *ACS Nano* **12**, 7352–7361 (2018).
120. Zhao, W. S. *et al.* Nanotube devices based crossbar architecture: Toward neuromorphic computing. *Nanotechnology* **21**, (2010).
121. Banerjee, D. *et al.* Pulse Generation Behavior of Single-Walled Carbon Nanotube/Polyoxometalate Complex Random Network. **3**, 150–145 (2020).
122. Shi, Z. *et al.* New supramolecular compounds based on porphyrin and polyoxometalate: Synthesis, characterization and nonlinear optical and optical limiting properties. *RSC Adv.* **4**, 50277–50284 (2014).
123. Yamazaki, Y., Yamashita, K., Tani, Y., Aoyama, T. & Ogawa, T. Structure determination and negative differential resistance of tetraarylporphyrin/polyoxometalate 2 : 1 complexes. *J. Mater. Chem. C* **8**, 14423–14430 (2020).

## Chapter 2

### Methodology

#### 2.1 Introduction

The chapter contains information of the chemicals, materials, equipment and the experimental procedure for this research work. It includes four sections: (i) the dispersion synthesis procedure of the nanocomposite, (ii) the electrode array fabrication technique, (iii) random network distribution method and, (iv) the characterization methods of AFM, FTIR, U-V Vis spectroscopy, I-V and I-t for the dispersion samples and the device. We start by tabulating the materials and chemicals used and then move on to the detailed descriptions of each section.

#### 2.2 Chemicals and materials

Table 2.1 List of all chemicals and materials used in this experiment

Chemical Name	Chemical Formula	Function	Supplier	Remarks
<b>HiPCo Single-walled carbon nanotube (SWNT)</b>		Conductive channel	Nanointegris	95% Purified Diameter = 0.8-1 nm
<b>Porphyrin Polyoxometalate</b>	$SV_2W_{10}O_{40}[H_4TPP]$	Redox active molecule	Osaka University	MW: 3845.84 gmmol <sup>-1</sup> Orthorhombic
<b>Ethanol</b>	$C_2H_5OH$	Dispersion solvent	Wako	Purity: 95% MW: 46.07 gmmol <sup>-1</sup>
<b>Acetone</b>	$CH_3COCH_3$	Solvent	Wako	Purity: 95% MW: 58.08 gmmol <sup>-1</sup>
<b>LOR-10A</b>		Lift-off resist		
<b>S18186</b>		Photoresist		
<b>MF319</b>		Developing agent		
<b>Dimethyl sulfoxide</b>	$(CH_3)_2SO$	Lift-off solution	Kanto Chemical	Purity: 99% MW: 78.14 gmmol <sup>-1</sup>

## 2.3 Synthesis of single-walled carbon nanotube/porphyrin polyoxometalate (SWNT/Por-POM) dispersion

### 2.3.1 Purification of HiPCo SWNT

The HiPco SWNT (purchased from NanoIntegris) with an average diameter of 1.2 nm and an average length of 1  $\mu\text{m}$  was purified by annealing at 200  $^{\circ}\text{C}$ , followed by applying HCl reflux to remove amorphous carbon and Fe catalysts.<sup>1</sup> The acid treated SWNT was filtered, washed with DI water, and dried to obtain the purified version. The schematic is shown in Fig. 2.3.1

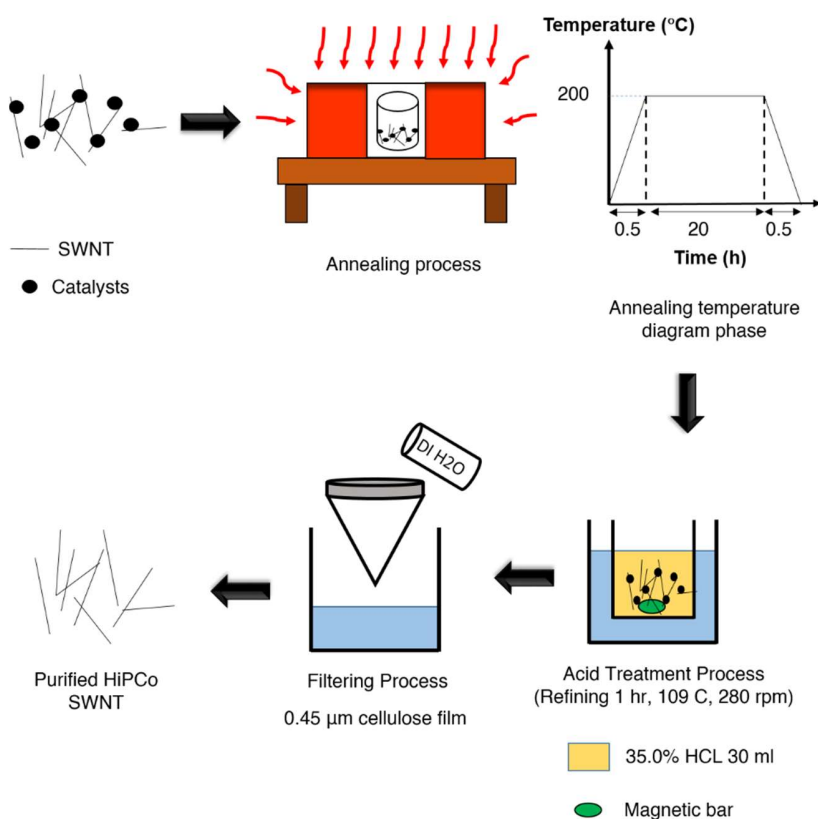


Fig.2.3.1 Schematic of the acid treated purification of HiPCo SWNT.

### 2.3.2 Dispersion of HiPCo SWNT with Por-POM

We functionalized the purified SWNT with Por-POM, using ultrasonication.<sup>2</sup> First, the purified SWNT ( $2 \times 10^{-2} \text{ gL}^{-1}$ ) was sonicated in ethanol for 1 h to initialize the unbundling process. We then added Por-POM ( $4 \times 10^{-2} \text{ gL}^{-1}$ ) in ethanol to the SWNT dispersion and ultrasonicated it for another 4 h to enhance the unbundling process. The resultant dispersion was centrifuged at 1,000 G for 15 mins, and the excess supernatant of Por-POM was discarded. The precipitate was again sonicated in ethanol to obtain the final stable dispersion of SWNT/Por-POM. A detailed schematic is shown in Fig. 2.3.2

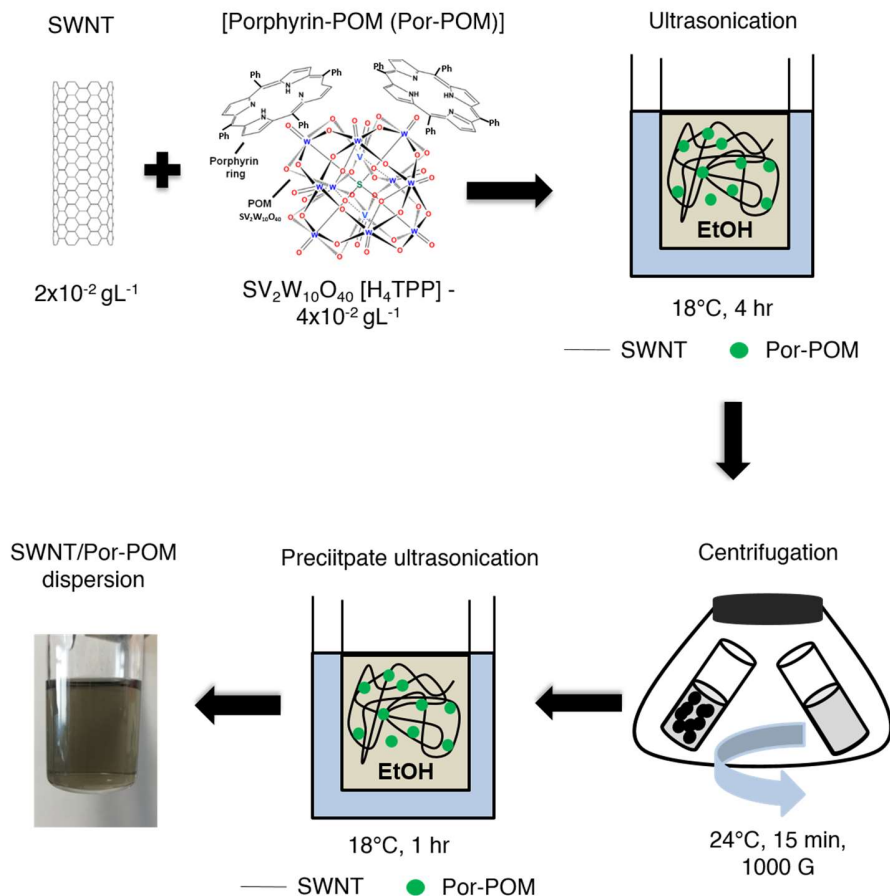


Fig.2.3.2 Schematic of the SWNT/Por-POM dispersion. The Por-POM is a Keggin type molecule where the porphyrin groups are attached to the oxygen groups of POM via hydrogen bonding of the amide group in porphyrin ring as depicted in the 2D ChemDraw schematic.

## **2.4 Fabrication of the micro electrode array**

Figure 2.4a shows the aluminum coated MEA patterned on a borosilicate glass substrate with photolithography, where the inner circular pads are 500  $\mu\text{m}$  and have a pitch of 1.5 mm. The substrate was cleaned each with IPA followed by DI water using a bath sonicator at 28 Hz for 3 min. A lift-off resist LOR-10A was then spin-coated onto the substrate with a spin coater ramped at 3,000 rpm for 50 s and was dried at 180  $^{\circ}\text{C}$  for 5 min on a hot plate. Following this was the deposition of a photoresist S18186, spin-coated at 4,000 rpm for 2 s, which was eventually dried on the hot plate at 90  $^{\circ}\text{C}$  for 5 min. The pattern was developed by placing a mask atop the substrate with exposure to UV light for 25 s using a photolithography machine. The resist was developed using a MF 319 developer for 90 s, which was washed with DI water and baked at 120  $^{\circ}\text{C}$  for 5 min to get the desired pattern. Aluminum metal with a thickness of 50 nm was sputtered onto the pattern and the LOR was removed by submerging in dimethyl sulfoxide solution at 60  $^{\circ}\text{C}$  for 20 min.

## **2.5 SWNT/Por-POM random network thin film deposition**

A vacuum-assisted wet transfer process like previous one<sup>3,4</sup> was adopted to initiate the deposition of SWNT/Por-POM thin film. 500  $\mu\text{l}$  SWNT/Por-POM dispersion was filtered through a 1  $\mu\text{m}$  mesh nitrocellulose filter paper (MCE, Millipore) and placed atop the circular pads of the electrode array. Few drops of acetone solution were casted on the filter paper, which left the substrate with only the SWNT/Por-POM film. The sample deposited on the substrate was then placed on top of a glass veil, 80% filled with acetone solution, and was dried using the acetone vapors by heating to 80  $^{\circ}\text{C}$  for 30 min. The schematic is displayed in Fig. 2.4b with the close optical microscopy images of the MEA before and after deposition of SWNT/Por-POM thin film.

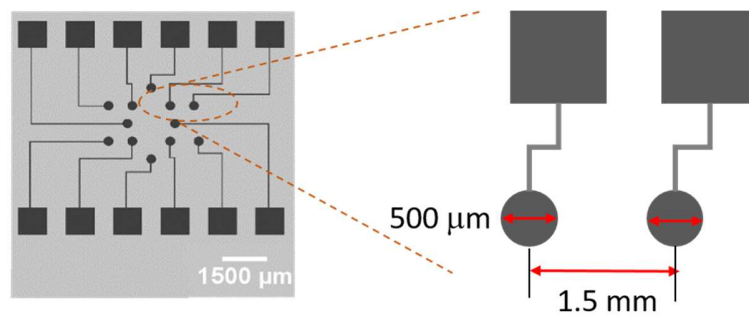
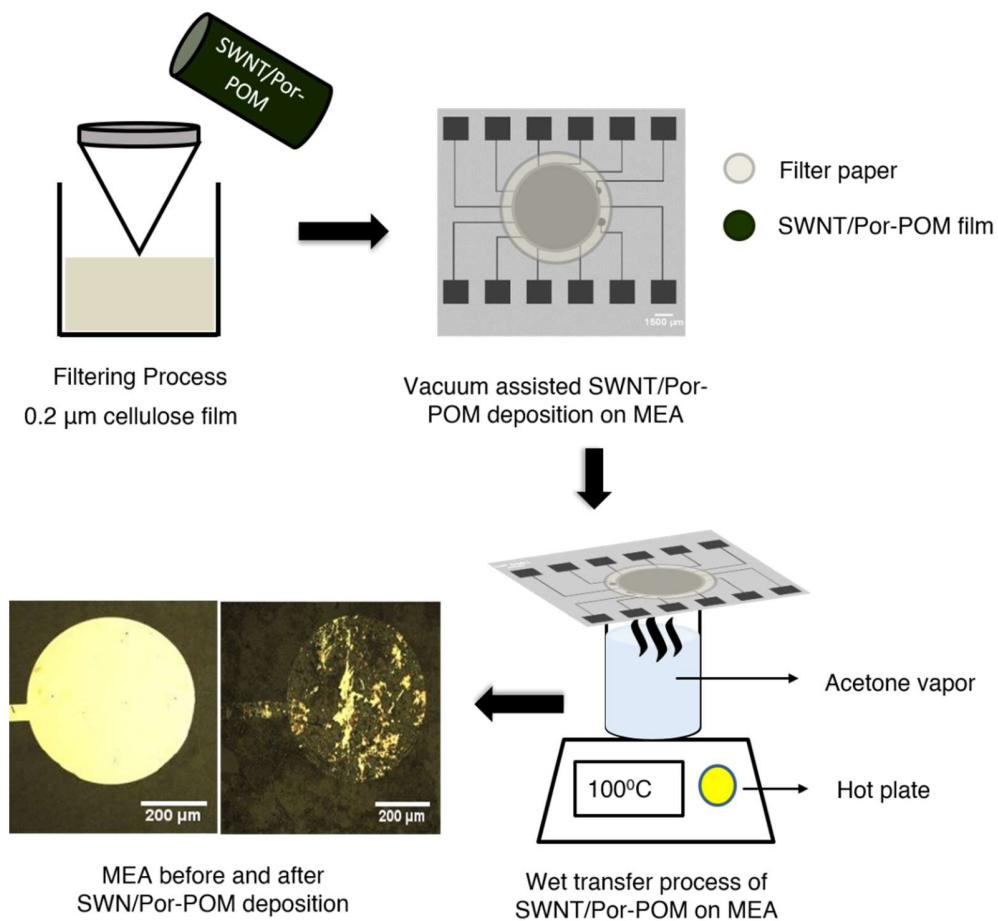


Fig.2.4 Shows optical image of the MEA fabricated using photolithography.



**Fig. 2.5** Schematic of the vacuum-assisted wet transfer thin film deposition of the SWNT/Por-POM on MEA. The optical microscopy image shows the MEA circular pads before (left) and after (right) the thin film deposition.



## **2.6 Atomic force microscopy (AFM)**

The atomic force microscopy (AFM) of a drop casted dispersion of SWNT/Por-POM on a Si/SiO<sub>2</sub> substrate was measured using a JEOL JSPM-5200 instrument shown in Fig. 4. AFM is a very high resolution type microscopic imaging process which can give information about the surface topology in the orders of fractions of a nanometer. The three major configurations used in studying the surface structure includes (i) contact mode, (ii) tapping mode and the (iii) non-contact mode of AFM study. The mode differs in terms of the probe distance from the sample surface. In this research work we characterize the surface of SWNT/Por-POM using the tapping mode method. The schematic of the mode is shown in Fig.5. The main principle of any AFM mode requires a raster scanning of the surface by the cantilever probe tip along x-y direction. The tip is irradiated with a laser and the motion of the tip along the z direction is studied via the change in the laser beam by a photodetector arising from the tip-surface interaction force. In tapping mode, the laser causes the tip to vibrate at its resonating frequency in a sinusoidal motion. Since the tip does not come in contact with the surface so the attractive and repulsive forces of the amplitude change laser is detected which gives us the idea of the topology. A feedback loop is connected to readjust the tip frequency and amplitude to its original point.<sup>5</sup>

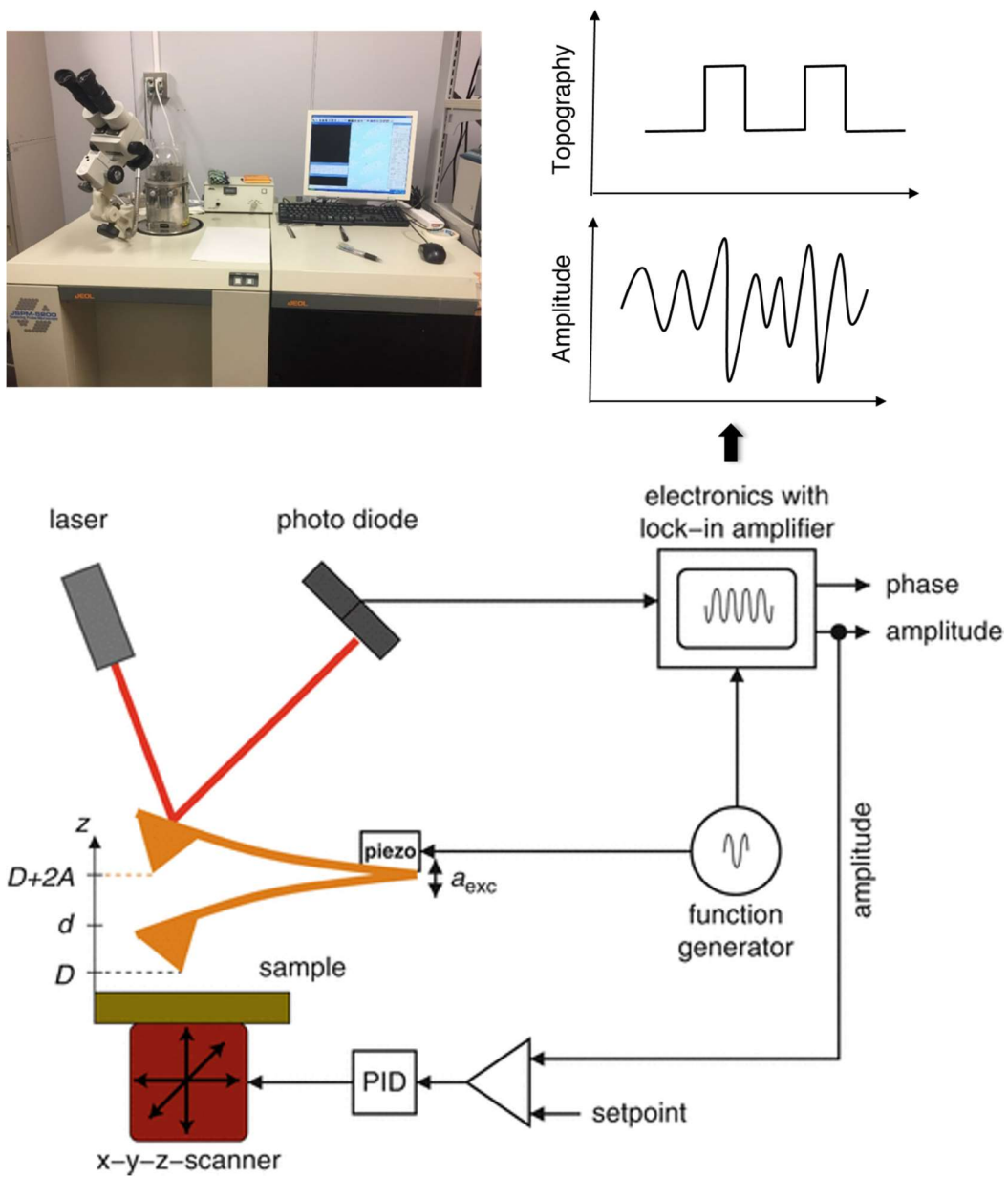


**Fig 2.6** AFM system JEOL JSPM-5200 with the tapping mode AFM schematic principle obtained from published report.

## 2.7 Field Emission Scanning Electron Microscopy (FE-SEM)

The FE-SEM measurements were done using Hitachi S-3400N model as shown in Fig. 2.7a. FE-SEM is a high resolution microscopy study that uses high accelerated electrons to determine the structure via scanning the sample and has a resolution of 1 nm. It was used to observe the SWNT/Por-POM network structure. The basic working principle is shown schematically shown in Fig. 2.7a. The electron gun is used to generate high voltage electrons ( $\sim 30$  kV) in vacuum which are accelerated in a high electric field gradient when passing through the anodes. The beam is collimated into a narrow point on the sample via electromagnetic lenses. On hitting the sample secondary electrons are deflected from the surface whose speed and angle are measured by the detector which gives the structural information of the material. The detector passes electrical signals to the processor to amplify it and finally is readout by the PC as an image file.

## 2.8 Spectroscopic studies

The UV-Vis spectroscopic measurement was done using the single monochromator Shimadzu-2600 equipment shown in Fig. 2.7b. The fundamental principle of UV-Vis spectroscopy is to give a quantitative measurement about the amount of incident light being absorbed when transmitted through a sample in solution as depicted in the schematic. Molecules of different nature absorbs different wavelengths of light upon interaction hence causes excitation of electrons from lower to higher states which are reflected as sharp absorption peaks in the spectrum. The absorbance intensity  $A$  is measured following Eq. (1) which is the logarithmic ratio of the incident light  $I_0$  to the transmitted light  $I$ .

$$A = \log_{10} \frac{I_0}{I} \quad (1)$$

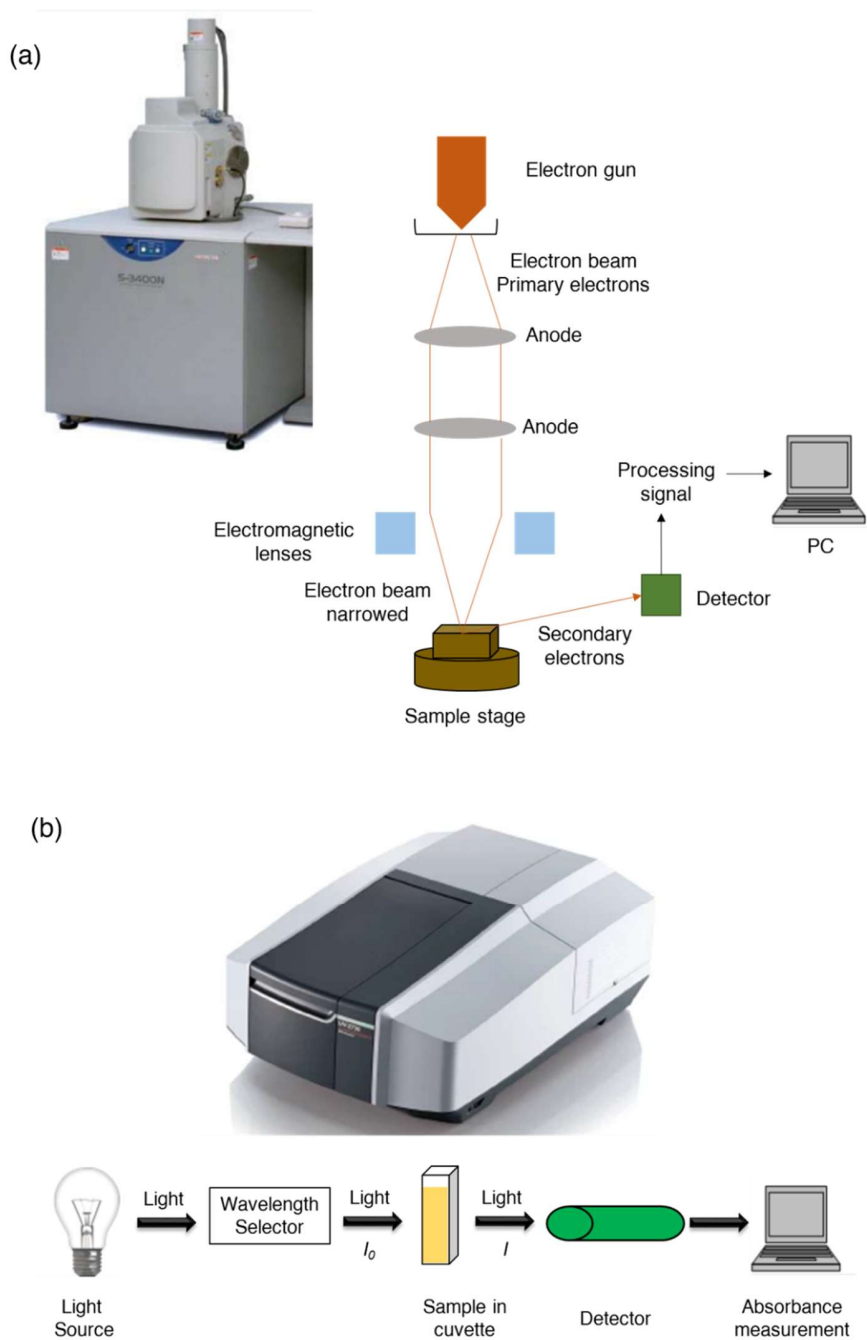


**Fig 2.7** Working principle of spectroscopic instruments. (a) Shimadzu-2600 UV-Vis spectrometer, top. Bottom shows the schematic of the absorbance principle. (b) Shimadzu IRSpirit A224057 spectrometer, top. Bottom shows the schematic of the FTIR principle.

## 2.8 Electrical measurements

### 2.8.1 The current –voltage ( $I$ - $V$ ) characteristic of the SWNT/Por-POM device

The  $I$ - $V$  characteristic of the fabricated sample was performed under a cyclic DC sweeping bias utilizing a probe system (Pascal Co., Ltd) with a semiconductor parameter analyzer (Agilent 4156B). The photograph of the machine is displayed in Fig. 2.8.1 with each of the equipment labelled specifically. The parameter analyzer functions as the software interface that supplies the input bias to the electrical probes. The optical microscope is used for magnification purpose to set up the probe pins on the device electrode pads. The entire set up is also equipped with a temperature controller whose need was not required in our study as all the measurements were done in room temperature (28°C) and pressure.

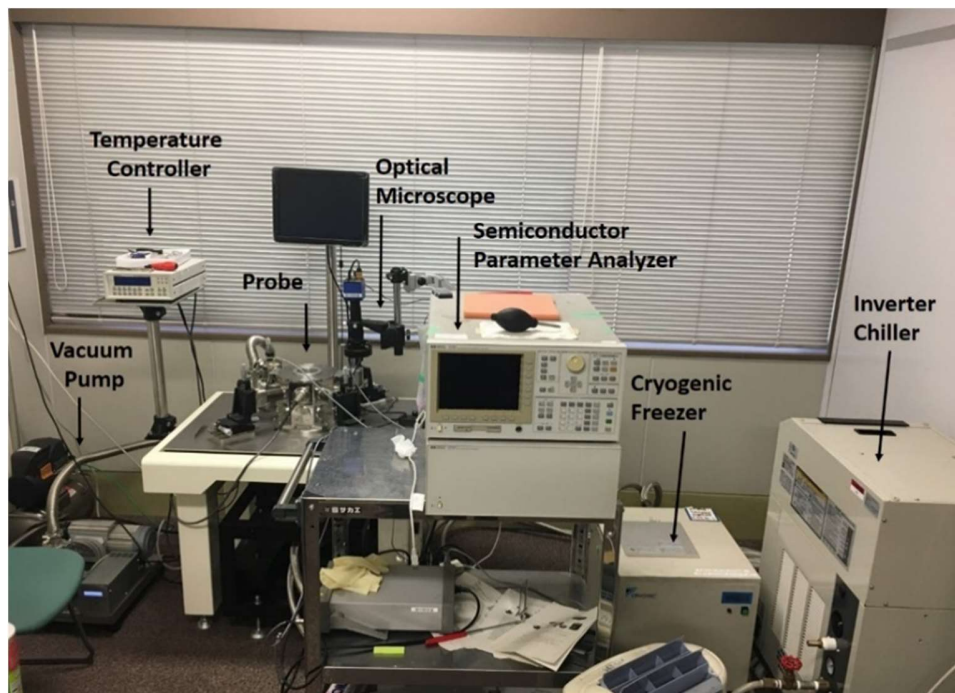


Fig. 2.8.1 Photograph of the probe station to carry out  $I$ - $V$  characterization.

### 2.8.2 The current –time (*I-t*) characteristic of the SWNT/Por-POM device

The *I-t* and majority reservoir computing (RC) tasks were all done using a custom-built electrical set-up schematically shown in Fig. 2.8.2. The input signal controlling the dynamics of the SWNT/Por-POM is fed through a function generator (Agilent 33120A), and readout signals collected from different outer electrode pads are measured using the DAQ (National Instruments, NI USB-9162). The electrode connectivities are established with the electrical probes using a two-probe system. The desktop PC acts as the software interface between the function generator and the DAQ via the LabVIEW software to monitor the I/O. To get the current from voltage response an additional 1 M $\Omega$  resistor along with a variable gain low noise current amplifier (DLPCA-200) was added in between the output electric probe and DAQ system.

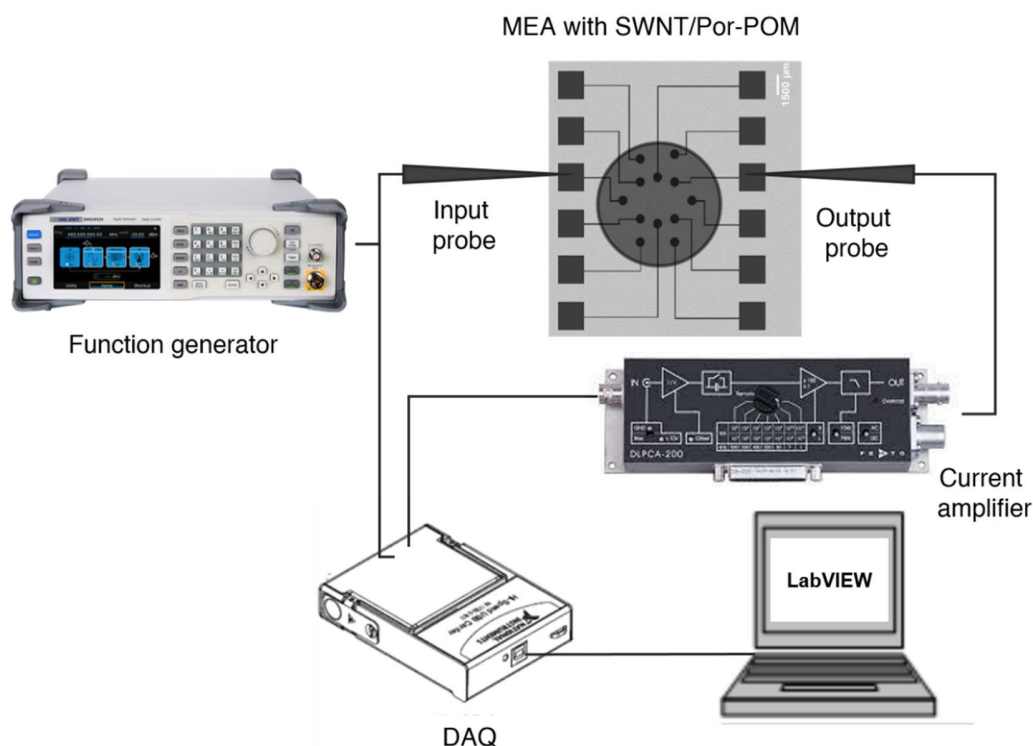


Fig. 2.8.1 Schematic showing the *I-t* measurement set-up. The custom built probe station was also used for conducting different RC tasks.

## References

1. Aji, W. W., Usami, Y., Hadiyawarman, Oyabu, R. & Tanaka, H. Frequency dependence dielectrophoresis technique for bridging graphene nanoribbons. *Appl. Phys. Express* **13**, (2020).
2. Hu, J., Ji, Y., Chen, W., Streb, C. & Song, Y. F. ‘Wiring’ Redox-Active Polyoxometalates To Carbon Nanotubes Using a Sonication-Driven Periodic Functionalization Strategy. *Energy Environ. Sci.* **9**, 1095–1101 (2016).
3. Tanaka, H. *et al.* A molecular neuromorphic network device consisting of single-walled carbon nanotubes complexed with polyoxometalate. *Nat. Commun.* **9**, 1–7 (2018).
4. He, X. *et al.* Wafer-scale monodomain films of spontaneously aligned single-walled carbon nanotubes. *Nat. Nanotechnol.* **11**, 633–638 (2016).
5. Aliano, A. & Cicero, G. *Encyclopedia of Nanotechnology. Encyclopedia of Nanotechnology* (2012). doi:10.1007/978-90-481-9751-4.

## Chapter 3

### **Reservoir dynamics emerging from an incidental structure of single-walled carbon nanotube/porphyrin-polyoxometalate complex**

**Abstract:** The fundamental pre-requisite for any dynamical system to act as a reservoir requires the fulfillment of non-linearity, echo state property and higher dimensional spatio-temporal information processing. In this chapter we explore these areas of interest in the single-walled carbon nanotube/porphyrin-polyoxometalate (SWNT/Por-POM) complex. We firstly synthesize the random network complex via a simple sonication and confirm the adsorption of Por-POM on SWNT via AFM, UV-Vis and FE-SEM characterizations. Construction of a simple function approximation task with non-linear and time-delay components from weighted linear output readouts confirmed that the reservoir dynamics arising from the device is more suitable for any non-linear computation but lags for higher memory task. The result was validated by studying the current-voltage (I-V), current-time (I-V) and memory capacity properties (MC). The I-V and I-t both typically revealed a non-linear negative differential (NDR) current fluctuation which were a source of  $1/f^\gamma$  noise manifesting in a maximized information processing for an edge of chaos computation. While, the MC did prove the short term memory of echo state property but a considerable low value suggested that it is underpowered by the greater non-linear dynamics thereby falling off for any delayed past memory construction task.



### 3.1 Introduction

The primary architecture of any neural network<sup>1</sup> consists of driving an input signal via a non-linear activation function and finally processing the signal as a linear weighted combination ( $w_{out}$ ) of the output states, as depicted in Fig. 3.1a. In the context of reservoir computing<sup>2,3</sup> this hidden activation layer represents a black box of recurrently connected non-linear units of random weights more precisely emulating the network structure of the human brain, shown in Fig. 3.1b.<sup>4</sup> The main purpose of the reservoir is to map the input to a higher dimensional output space which are solely the reproduction of the reservoir states occurring at different points in the network over time. Thus the temporal dynamics of the reservoir at given time  $X_i(t)$  is dependent on its current weighted ( $W_{in}$ ) input state  $U(t)$  and its recent weighted ( $W_{res}$ ) past state  $X(t-1)$  operated in a non-linear fashion given by Eq. (3.1) where  $f$  is the non-linear activation function.<sup>5</sup>

$$X_i(t) = f(W_{in}U(t) + W_{res}X_i(t-1)) \quad (3.1)$$

Such information processing over short-term memorization is a characteristic of the echo-state property (ESP) as formulated firstly by Jaeger et al.<sup>6</sup> An experimental way to check the ESP is to compute the memory capacity (MC)<sup>7</sup> of the device that measures the networks ability to reconstruct the past information from the reservoir on the network output by computing correlations. The MC is calculated with the Eq. (3.2), where  $u_k(t-1)$  is the input presented k-steps before the current input  $u_k(t)$  and  $y_k(t)$  is the linear weighted combined reservoir output (Fig. 3.1) used to construct the given delayed input.

$$MC = \sum_{k=1}^{k_{max}} MC_k = MC_k = \frac{cov^2(u(t-k), y_k(t))}{\sigma^2(u(t))\sigma^2(y_k(t))} \quad (3.2)$$

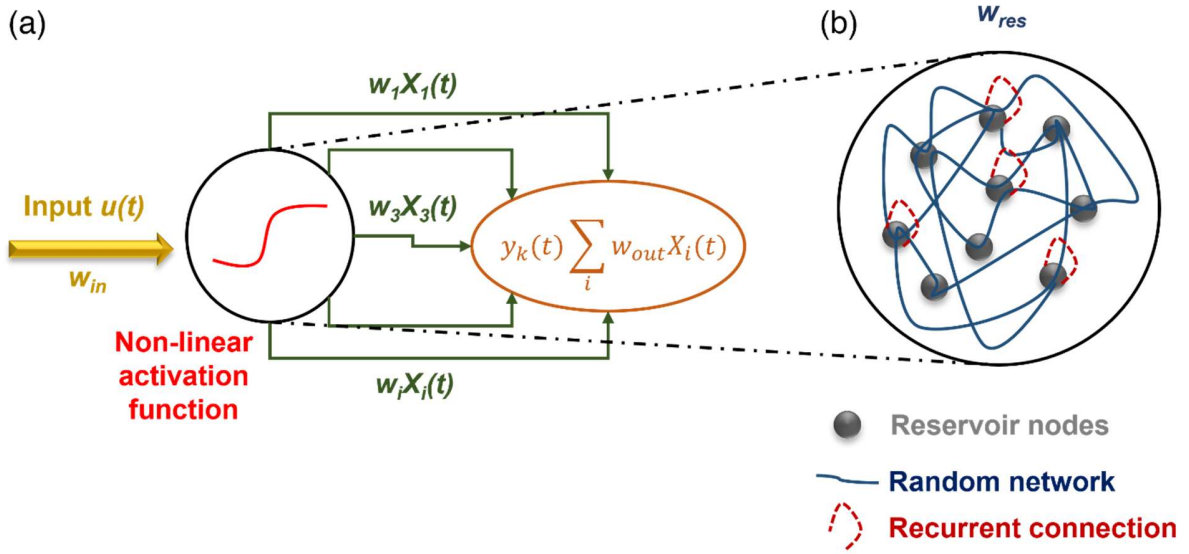


Fig. 3.1 The neural network functioning, (a) schematic of general architecture where a hidden layer of non-linear activation function drives an input to the output for linear weighted processing. (b) A reservoir acting as such a hidden layer with the reservoir nodes acting as the non-linear activation functional unit connected by recurrent connections.

The MC is higher when the  $u_k(t-1)$  matches the  $y_k(t)$  giving a high covariance factor ( $cov$ ). The non-linearity and the echo-state property of short-term memory are important attributes to any reservoir system as it allows computation of different RC tasks like higher time-series prediction, (memory property) and complex function optimizations (non-linearity).<sup>8-14</sup> Another vital feature that these reservoirs hold is their ability to process information at the border of stable and unstable regime giving rise to edge of chaos<sup>15-20</sup> computation like human brain. The presence of such trait allows the reservoir to higher computational efficiency thus satisfactorily achieving a desired task irrespective of its kind. Physical reservoir systems with such edge of chaos computing<sup>9-11,21</sup> have been recently reported substantiating the validity of RC to be a close edged bio-inspired unconventional platform. Since materials possessing these rudimentary properties are being constantly researched for their future use as in-materio RC, we too hereby experimentally study

the reservoir dynamics of our single-walled carbon nanotube/porphyrin-polyoxometalate complex (SWNT/Por-POM). The idea to incorporate such a material in the list of existing in-materio RC framework came from the proposed theoretical model of SWNT/POM where the intrinsic redox mediated charge transfer dynamics was utilized as high dimensional outputs to construct the NARMA-10 time series.<sup>22</sup> The complex imparts a non-linear negative differential resistance (NDR) dynamic at room temperature, a source of noise fluctuations,<sup>23</sup> and closely resembled the neuronal information processing behavior of the human brain.<sup>24</sup> Herein we extend the idea to a real physical platform and utilized a porphyrin functionalized POM formulated as  $\text{SV}_2\text{W}_{10}\text{O}_{40}[\text{H}_4\text{TPP}]$ .<sup>25</sup> The Por-POM is a 3D Keggin type molecule known to form stable thin films with characteristic feature of non-linear NDR behavior,<sup>25,26</sup> but never have such dynamics been investigated for the reservoir properties. We initially prepare a complex network of SWNT/Por-POM and study its functionalization characteristics via UV-Vis, FTIR, AFM and Fe-SEM techniques. We move on to discuss the SWNT/Por-POM dynamics via current-voltage (I-V) and time-domain current (I-t) studies under the influence of DC bias input. The results reflect on the spatio-temporal dynamics manifesting in a source of  $1/f'$  noise useful for brain like computational performance. To understand the fading memory effect, the MC was calculated by giving a random signal in the voltage interval of [0, 1]. The computational performance was analyzed via a simple function approximation task which served as a trade-off for non-linearity and memory operation. The task reveals our device's capability to perform higher degree of non-linear computation rather than memory-based operations.

## 3.2 Methods

### 3.2.1 SWNT/Por-POM dispersion

The SWNT/Por-POM dispersion was obtained using a known procedure.<sup>27</sup> Initially,  $2 \times 10^{-2} \text{ gL}^{-1}$  HiPCo SWNT, purified according to the previous report<sup>28</sup> and  $4 \times 10^{-2} \text{ gL}^{-1}$  of Por-POM were first bath sonicated in ethanol for 1 h (40 k Hz) separately and then for 4 h by mixing them together. The dispersion was then centrifuged at 1,000 G for 15 min and the excess of supernatant was discarded. The precipitate was collected and was further bath sonicated in ethanol for 1 h to get the final dispersion.

### 3.2.2 Fabrication of MEA substrate

Aluminum coated MEA pattern was obtained via a standard photolithography process on a borosilicate glass substrate. A lift-off resist LOR-10A was first spin coated at 3,000 rpm for 50 s followed by the deposition of the photoresist S18186 spin-coated at 4,000 rpm for 2 s. The substrate was pre-baked at 90 °C for 5 min and the pattern was developed with a 25 s exposure to the UV light. Finally, the resist was developed using MF 319 developer for 90 s and 50 nm thick aluminum metal was sputtered that produced the desire MEA substrate with inner circular pad diameter of 500  $\mu\text{m}$  and a pitch of 1.5 mm.

### 3.2.3 Thin film deposition of SWNT/Por-POM computational material

Thin film of SWNT/Por-POM random network was deposited onto the MEA pattern as per the previous report.<sup>22,29</sup> A vacuum-assisted wet transfer process was applied where 500  $\mu\text{L}$  of SWNT/Por-POM was filtered through a 1  $\mu\text{m}$  nitrocellulose paper and was placed on top of the MEA substrate with the SWNT/Por-POM facing down followed by its dissolution in acetone. The

entire substrate with the thin film was dried using acetone vapors at 80 °C by placing it on a glass veil of acetone solution.

#### *3.2.4 Characterization*

The UV-Vis spectroscopic measurement for Por-POM and SWNT/Por-POM were all done in the ethanol solvent using the single monochromator Shimadzu-2600 equipment. In each of the cases the concentration of SWNT and Por-POM was kept same as the synthesis part. The atomic force microscopy (AFM) of a drop casted dispersion of SWNT/Por-POM on a Si/SiO<sub>2</sub> substrate was measured using a JEOL JSPM-5200 instrument in the tapping mode. The FE-SEM was performed with Hitachi S-3400 N.

#### *3.2.5 Electrical Measurements*

The I-V characteristics was measured using a probe system (Pascal Co., Ltd) with a semiconductor parameter analyzer (Agilent 4156B) using a  $\pm 1$  V DC bias cyclically swept at 25 mVs<sup>-1</sup>. The I-t, was done at a constant DC bias voltage of 1 V for 300 s. The set-up shown in *Fig.2.8.2 of Chapter 2* was used with 1 M $\Omega$  resistor along with a variable gain low noise current amplifier (DLPCA-200) added between the output electric probe and DAQ system. The MC and function approximation all were done using Python coded programs. The input signal used for these studies were given using the set-up task in *Fig.2.8.2 of Chapter 2* where the function generator was replaced by a multifunctional I/O DAQ system (NI PXIe-4141) and the readouts were collected using a high speed USB carrier (NI USB-9162) sampled at 1 kHz. Since the readouts were voltage form, the noise current amplifier along with resistor was not connected.

The logarithmic plots of PSD were fitted using the power law in Eq. (3.3) where A represents the proportionality constant and  $\gamma$  represents the scaling factor. Both the FFT and the fitting was done using Origin Pro 9 software.

$$PSD = \frac{A}{f^\gamma} \quad (3.3)$$

### 3.3 Results and discussion

Figure 3.2a shows the AFM of the drop casted film of SWNT/Por-POM dispersion prepared by sonication method. Dense network of interconnected strands of SWNT with contrasting surface regions are visible. A scan with a closer area in Fig. 3.2b revealed bright spots of circular particles of 5.4-6.7 nm variable height thickness being adsorbed on the sites of bundled SWNT of 3.2 nm. Usually Por-POM has an average unit cell dimensions of 2.2 nm,<sup>25</sup> but to confirm its presence we studied the UV- Vis spectroscopy of the dispersion in ethanol solvent. Fig. 3.2c shows the absorption spectra of both Por-POM (black dot line) and SWNT/Por-POM (red solid line) normalize to the intensity. In both the cases strong porphyrin Soret band peak at 416 nm, tungsten-oxygen charge transfer peak at 266 nm and Q band peaks at 513, 547, 590 and 645 nm are clearly visible.<sup>26</sup> Apart from that in the complex structure, multiple peaks in the range above 700 nm to 1250 nm can be observed in the inset which are signatures of E<sub>11</sub> and E<sub>22</sub> semiconducting peaks of HiPco SWNT showing multiple chirality's of high diameter tubes.<sup>30</sup> Although the lower wavelength M<sub>11</sub> peaks of small diameters are missing due to the purification process,<sup>31</sup> still the spectrogram confirms that the dispersion indeed is a mixture of SWNT/Por-POM complex. The variable size distribution of Por-POM seen from the AFM (Fig. 3.2b) is understandable as they have the tendency to stack up due to  $\pi$ - $\pi$  interactions<sup>25</sup> hence generating a non-homogeneous surface functionalization driven by sonication. Additional heterogeneity in the network structure

from the vacuum assisted wet transfer thin deposition can also be seen from the random distribution of SWNT in the FE-SEM image in Fig. 3.2d. In the context of RC such conglomeration of intertwined networks with varying Por-POM cluster density is apt as it replicates the brain-like network structure where neural non-homogeneity has been proven to be efficient for information processing and critical learning.<sup>32,33</sup> To check the RC device performance we used a sine wave function approximation task given by Eq. (3.4) where ( $\nu, \tau$ ) are the non-linear and time-delayed task parameters that control the extent of non-linearity and memory required to construct the signal  $y(t)$  from the given voltage input  $u(t)$  of random noise distributed in the interval  $[-1,1]$  V. The target  $y(t)$  was constructed from the weighted linear combinations of eleven readouts as per Eq. (3.5) where each output weight  $w_{out}$  was optimized using a ridge regression analysis in Eq. (3.6), with a regularization parameter  $\lambda$  of 0.1. The fitting performance was evaluated using the normalized mean square error (NMSE) and accuracy given in Eq. (3.7) and (3.8).

$$y(t) = \sin(\nu u(t - \tau)) \quad (3.4)$$

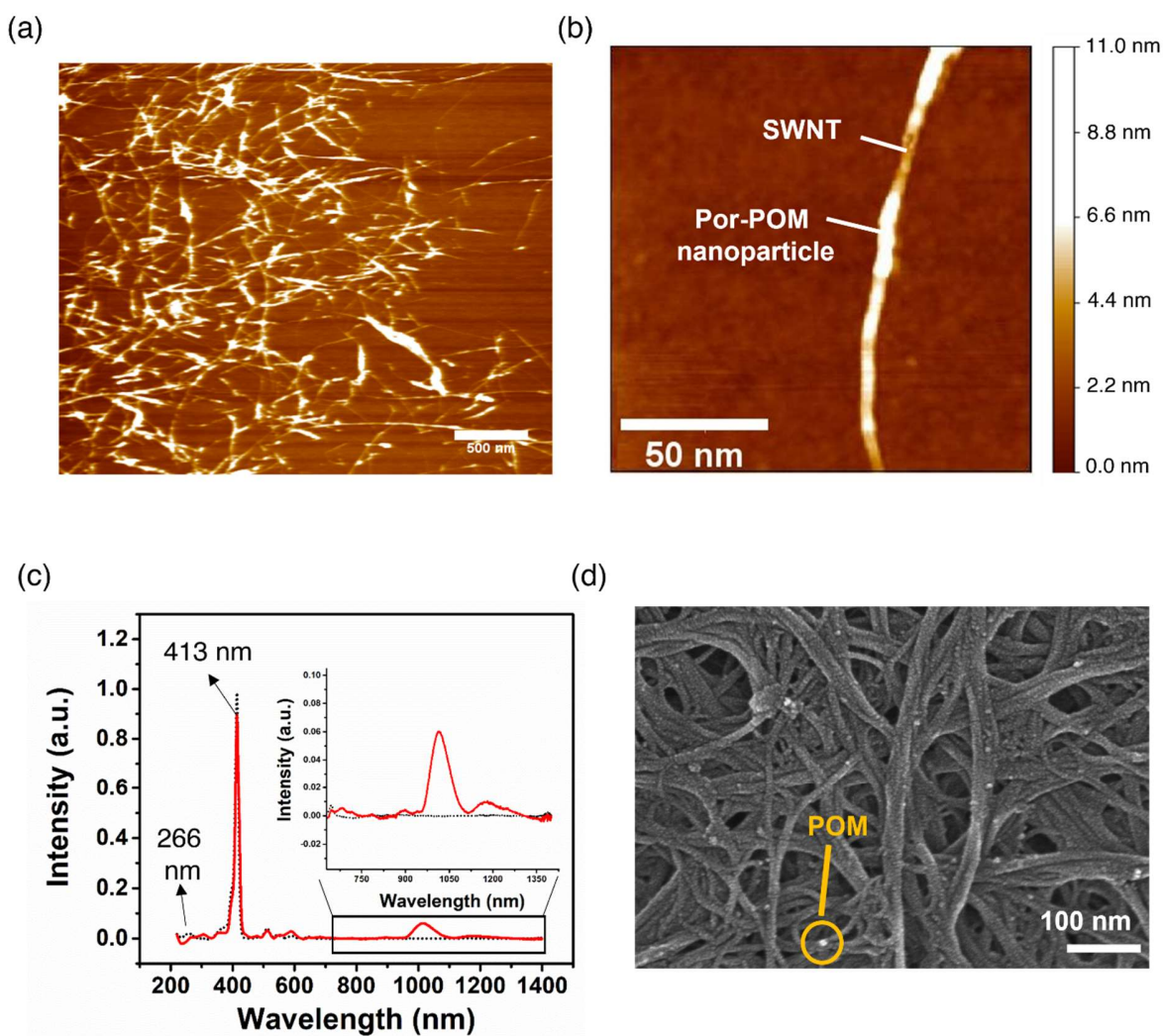
$$w_{out} = (X_i^T X_i + \lambda I) X_i^T y(t) \quad (3.5)$$

$$Z(t) = \sum_{i=1}^{11} w_{out} X_i(t) \quad (3.6)$$

$$NMSE = \frac{\sum y(t) - Z(t)^2}{\sum Y(t)^2} \quad (3.7)$$

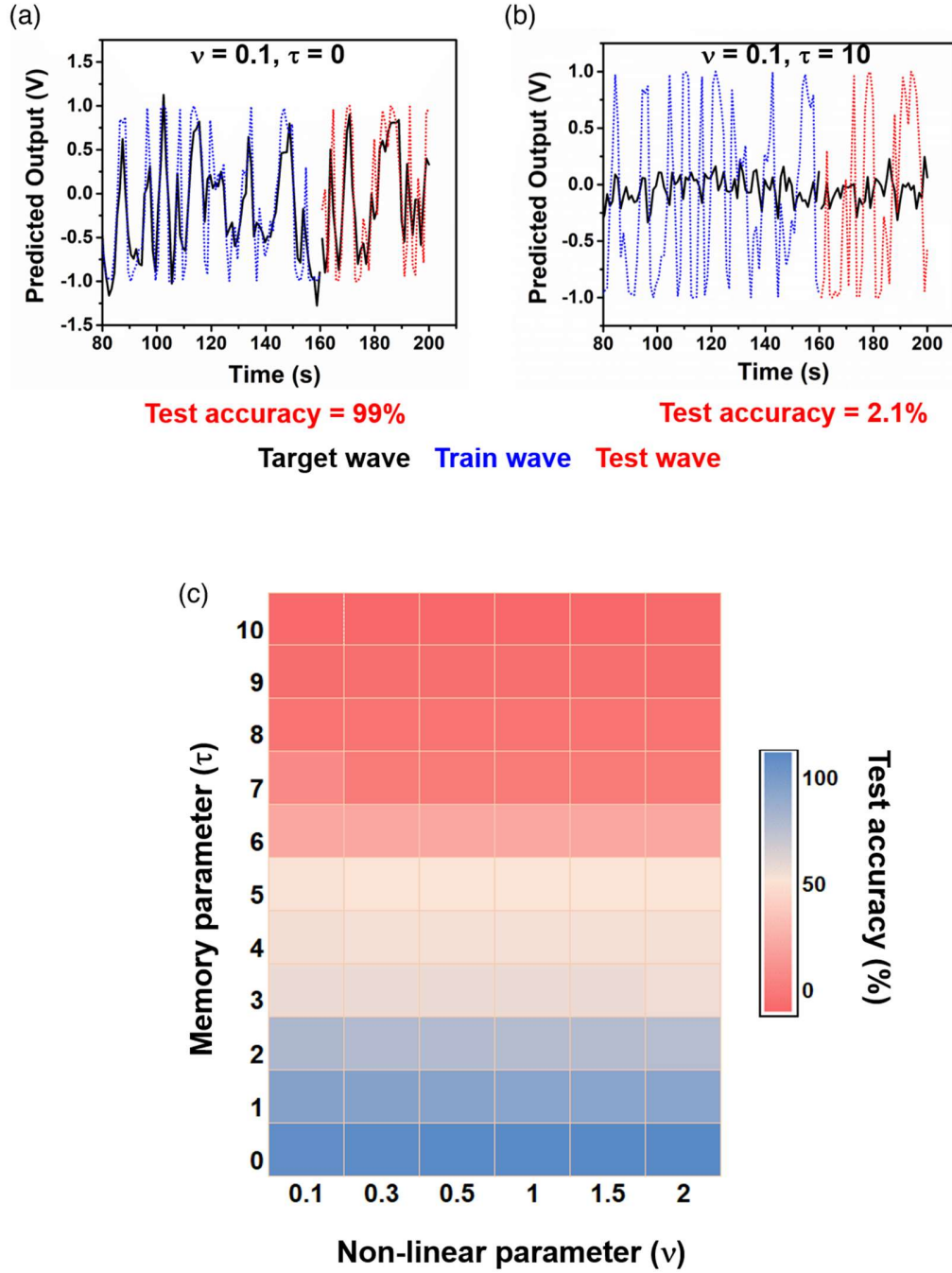
$$Accuracy = ((1 - NMSE) \times 100)\% \quad (3.8)$$

Figure 3.3a shows the trained (blue line) and the test output (red line) for  $\nu = 0.1$  and  $\tau = 0$  with a test fitting accuracy of 99%, showing that when there is no past information to be remembered, a low non-linear task can be easily computed over a RC framework training.



**Fig. 3.2** SWNT/Por-POM characterization. (a) AFM image of dispersed SWNT/Por-POM on Si/SiO<sub>2</sub> substrate. (b) Magnified version of AFM showing Por-POM particles of variable height thickness with a region of bare SWNT. (c) UV-Vis spectroscopy of Por-POM (black dotted line) and SWNT/Por-POM (red solid line) with characteristic peaks at 413 and 266 nm. The inset shows the region above 600-1250 nm for the SWNT absorption peaks. (d) FE-SEM of a random network of SWNT/Por-POM obtained after vacuum assisted wet transfer deposition.





**Fig. 3.3** The sine wave function approximation task obtained using Eq. (3.4). (a) The task for  $\nu = 0.1$  and  $\tau = 0$  indicating low non-linearity and no memory, with the test fitting of 99%. (b) The task for  $\nu = 0.1$  and  $\tau = 10$  indicating low non-linearity and high time-delayed memory, with the test fitting accuracy of 2.1%. (c) Heat map showing variation of  $\tau$  vs  $\nu$ . The higher the  $\tau$ , lower is fitting accuracy as indicated by the color bar.

But as soon as we increased the delay  $\tau = 10$ , keeping the  $\nu$  fixed at 0.1, we see a large degradation in both training and testing performance with very low accuracy of 2.1% in Fig. 3.3b. To get a clear picture of how the memory/non-linearity evolves in the regime RC, we performed the same task by varying  $\nu$  and  $\tau$  and constructed a heat map showing the variation of  $\nu$  (x-axis) as a function of  $\tau$  (y-axis). The heat map shows the test fitting accuracy as a color gradient in the plot where the blue represents the best performance while the red shows the worst as indicated by the color bar. A general trend of decreasing accuracy with increasing  $\tau$  is observed for all  $\nu$  indicating that irrespective of the increasing degree of non-linearity, tasks with the least past memory construction always excels the higher ones. It has been proven before that a trade-off between memory and non-linearity exists and that for a reservoir to operate at the optimal regime of memory and non-linearity, inclusion of linear units in the reservoir is important.<sup>34</sup> In order to get a better understanding we separately studied the MC and current-voltage dynamics. MC was performed according to Eq. (3.2) with an input of random signal in the interval of  $[0, 1]$  following the same methodology of function optimization, and a graph of MC vs delayed time-step was plotted in Fig. 3.4a. The gradual decrease over increasing time steps do support the validity of echo state property of fading memory<sup>6</sup> but the low value of MC about 4.2 strengthens the above result of time delayed function approximation. The heat map in Fig. 3.3c too shows that a transition point around  $\tau = 4$  or 5 exists after which the performance degrades rapidly for any number of non-linearity as it shows a clear non-linear current increase in both upward (black line) and downward (red line) scan in Fig. 3.4b. The above two experiments thus proves that a lack of linear component in the heterogeneous random recurrent network of SWNT/Por-POM makes way for an in-materio RC framework that is mostly suitable for non-linear tasks like approximations rather than time delayed past memory predictions.

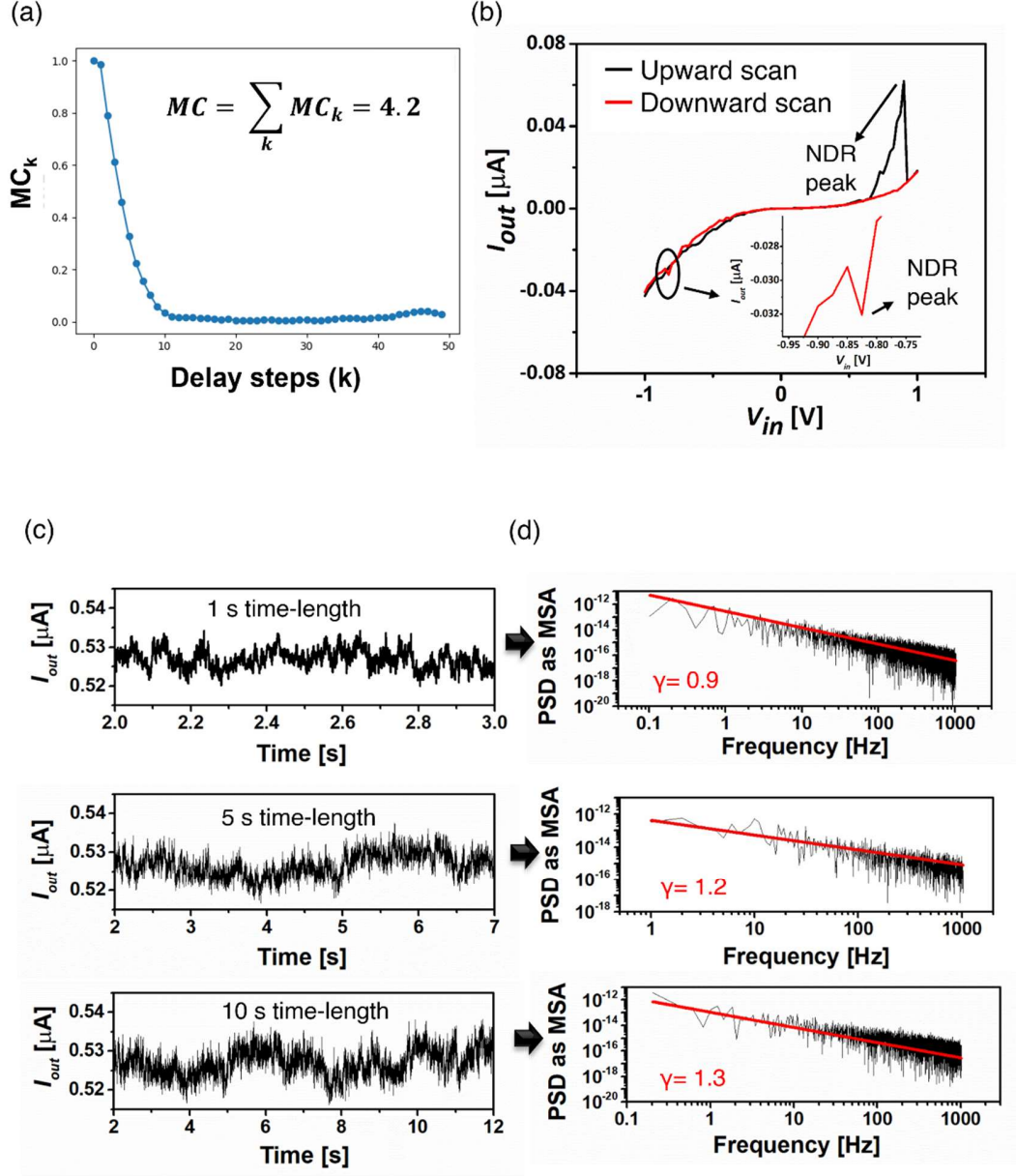


**Fig. 3.4** Validation of the low memory high non-linearity and maximum information processing. (a) The graph of memory capacity calculated by summing over all  $k$ -step delayed  $MC_k$ . (b) The I-V graph showing characteristic NDR peaks both in positive and negative bias region (inset) with non-linear current dynamics. (c) The temporal current dynamics study under constant DC bias of 1 V. NDR like fluctuations are present in all time lengths of 1 s (top), 5 s (middle) and 10 s (bottom). (d) The logarithmic power spectral density (PSD, black) obtained from FFT of current in (c) and its corresponding fitting (red line) calculated via Eq. (3.3). A  $0 < \gamma < 2$  suggests the network dynamics has  $1/f^\gamma$  noise useful for intelligent computation.

Another important feature that surfaces up in the I-V is a decrease in current at higher biases of 0.9 V and -0.83 V (inset), characteristic of negative differential resistance (NDR) behavior dominant also in the time-dependent current dynamics ( $I-t$ ) at different time-lengths of 1 s (top), 5 s (middle) and 10 s (bottom) depicted in Fig. 3.4c. The spatial information of NDR fluctuations in current are signatures of Por-POM molecules owing to their charge transfer redox mediated capacitive nature.<sup>25</sup> A qualitative understanding of such information processing was analyzed with the power spectral density (PSD, Methods) of each 1 s (top), 5 s (middle) and 10 s (bottom) time-lengths as represented in Fig. 3.4d. The logarithmic PSD when fitted (see Methods) showed a  $1/f^\gamma$  power law scaling with the scaling factor  $\gamma$  of 0.9 (1 s), 1.3 (5 s) and 1.2 (10 s) suggesting that these fluctuations are characteristics of the flicker noise. The result is consistent with other SWNT/polyoxometalate complex<sup>35</sup> and reflects on the importance of redox mediated charge-discharge property intrinsic to these random network devices that form the genesis for such random signals of spatio-temporal information. In real world, the human brain serves as an example of such  $1/f^\gamma$  power law and information correlation phenomena.<sup>36</sup> Varied spatio-temporal correlated activities, throughout the random network of recurrently connected neighboring neurons, are created from a time-varying external input over its entire time-length. Such maximization of information processing renders a  $1/f^\gamma$  power law in the PSD, thereby providing the highest computing performance at the ‘edge of chaos’.<sup>37,38</sup> Like human brain, thin films of SWNT/polyoxometalate complexes too possess such interconnected networks with easy solution processability. Due to their multiple redox states and varying degree of SWNT/polyoxometalate capacitive junctions, when perturbed by an input, cascade of charge-discharge processes of different intensities occurs at these randomly recurrent networks conceived by the CAM model.<sup>22,35</sup> The series of cascades hence creates a maximization of spatio-temporal information

exchange thereby producing high-dimensional reservoir states of different frequencies reflected in the PSD following the  $1/f^\gamma$  power law. It is also to be noted from Figure 1d, that these fluctuations in the current satisfies the condition of  $0 < \gamma < 2$  for all time-lengths supporting the scale-free nature of the events<sup>39</sup> a signature of  $1/f^\gamma$  power law, which suggests that the information generated from the input is solely an intrinsic property of the material and hence is retained over all lengths of the processing time.

### 3.4 Conclusion

The chapter deals with the formalism of reservoir dynamics emergent in our SWNT/por-POM complex. We successfully synthesized a functionalized dispersion of SWNT/por-POM as evident from the UV-Vis graph which showed all the characteristics of por-POM and SWNT in the absorption spectra. The AFM and FE-SEM revealed that the sonication and vacuum assisted wet transfer process drives a heterogeneous random network of SWNT/por-POM thin films on the MEA substrate just like the human network brain connectivity. The reservoir task of sine wave approximation with parameter of non-linearity  $\nu$  and time delay memory  $\tau$  was performed which clearly showed a trade-off where only the device excelled in non-linear tasks but failed to reconstruct distant past information. The result was validated with a low MC and high non-linear dynamics (I-V) that is inherent of SWNT/por-POM. The NDR like spatio-temporal information intrinsic to the system proves to be valuable source of  $1/f^\gamma$  noise fluctuations characteristic of ‘edge of chaos computation’ like the human brain. Based on these above results we proceeded to build up different RC tasks to evaluate our devices in-materio RC framework performance. We start off with the benchmark of waveform generation task in Chapter 2 and show that the sine wave approximation in the regime of  $\tau=0$  is useful for constructing complex waveforms with high accuracy. In Chapter 3 we increase the RC benchmark complexity by giving two binary inputs and

focus on the NDR property as a machine intelligent index for construction of all the logic functions. Lastly, we finally perform the benchmark task of object classification from tactile sensory data and emphasize on the point of  $1/f'$  maximized information processing for better classification.

## References

1. Wilamowski, B. M. How to not get frustrated with neural networks. *Proc. IEEE Int. Conf. Ind. Technol.* 5–11 (2011). doi:10.1109/ICIT.2011.5754336
2. Lukosevicius, M., Jaeger, H. & Schrauwen, B. Reservoir Computing Trends. *Kunstl Intell* **26**, 365–371 (2012).
3. Schrauwen, B., Verstraeten, D. & Van Campenhout, J. An overview of reservoir computing: Theory, applications and implementations. in *ESANN 2007 Proceedings - 15th European Symposium on Artificial Neural Networks* 471–482 (2007).
4. McKenna, T. M., McMullen, T. A. & Shlesinger, M. F. The brain as a dynamic physical system. *Neuroscience* **60**, 587–605 (1994).
5. Tanaka, G. *et al.* Recent advances in physical reservoir computing: A review. *Neural Networks* **115**, 100–123 (2019).
6. Jaeger, H. The “echo state” approach to analysing and training recurrent neural networks – with an Erratum note 1. *GMD Rep.* 1–47 (2010). doi:citeulike-article-id:9635932
7. Farkaš, I., Bosák, R. & Gergel', P. Computational analysis of memory capacity in echo state networks. *Neural Networks* **83**, 109–120 (2016).

8. Bianchi, F. M., Scardapane, S., Lokse, S. & Jenssen, R. Reservoir Computing Approaches for Representation and Classification of Multivariate Time Series. *IEEE Trans. Neural Networks Learn. Syst.* **32**, 2169–2179 (2021).
9. Kotooka, T. *et al.* Ag<sub>2</sub>Se Nanowire Network as an Effective In-Material Reservoir Computing Device. 1–20 doi:10.21203/rs.3.rs-322405/v1
10. Demis, E. C. *et al.* Nanoarchitectonic atomic switch networks for unconventional computing. *Jpn. J. Appl. Phys.* **55**, (2016).
11. Hadiyawarman *et al.* Performance of Ag-Ag<sub>2</sub>S core-shell nanoparticle-based random network reservoir computing device. *Jpn. J. Appl. Phys.* **60**, (2021).
12. Zhong, Y. *et al.* Dynamic memristor-based reservoir computing for high-efficiency temporal signal processing. *Nat. Commun.* **12**, 1–9 (2021).
13. Moon, J. *et al.* Temporal data classification and forecasting using a memristor-based reservoir computing system. *Nat. Electron.* **2**, 480–487 (2019).
14. Wyffels, F. & Schrauwen, B. A comparative study of Reservoir Computing strategies for monthly time series prediction. *Neurocomputing* **73**, 1958–1964 (2010).



15. Barras, C. Mind maths: Brainquakes on the edge of chaos. *New Sci.* **217**, 36 (2013).
16. Kawai, Y., Park, J. & Asada, M. A small-world topology enhances the echo state property and signal propagation in reservoir computing. *Neural Networks* **112**, 15–23 (2019).
17. Snyder, D., Goudarzi, A. & Teuscher, C. Computational capabilities of random automata networks for reservoir computing. *Phys. Rev. E - Stat. Nonlinear, Soft Matter Phys.* **87**, 1–8 (2013).
18. Büsing, L., Schrauwen, B. & Legenstein, R. Connectivity, dynamics, and memory in reservoir computing with binary and analog neurons. *Neural Comput.* **22**, 1272–1311 (2010).
19. Schrauwen, B., Büsing, L. & Legenstein, R. On computational power and the order-chaos phase transition in Reservoir Computing. *Adv. Neural Inf. Process. Syst. 21 - Proc. 2008 Conf.* 1425–1432 (2009).
20. Boedecker, J., Obst, O., Lizier, J. T., Mayer, N. M. & Asada, M. Information processing in echo state networks at the edge of chaos. *Theory Biosci.* **131**, 205–213 (2012).
21. Chen, T., Bobbert, P. A. & Wiel, W. G. 1/ f Noise and Machine Intelligence in a Nonlinear Dopant Atom Network . *Small Sci.* **1**, 2000014 (2021).

22. Tanaka, H. *et al.* A molecular neuromorphic network device consisting of single-walled carbon nanotubes complexed with polyoxometalate. *Nat. Commun.* **9**, 1–7 (2018).
23. Setiadi, A. *et al.* Room-temperature discrete-charge-fluctuation dynamics of a single molecule adsorbed on a carbon nanotube. *Nanoscale* **9**, 10674–10683 (2017).
24. Miller, K. J., Sorensen, L. B., Ojemann, J. G. & Den Nijs, M. Power-law scaling in the brain surface electric potential. *PLoS Comput. Biol.* **5**, e1000609 (2009).
25. Yamazaki, Y., Yamashita, K., Tani, Y., Aoyama, T. & Ogawa, T. Structure determination and negative differential resistance of tetraarylporphyrin/polyoxometalate 2 : 1 complexes. *J. Mater. Chem. C* **8**, 14423–14430 (2020).
26. Shi, Z. *et al.* New supramolecular compounds based on porphyrin and polyoxometalate: Synthesis, characterization and nonlinear optical and optical limiting properties. *RSC Adv.* **4**, 50277–50284 (2014).

27. Hu, J., Ji, Y., Chen, W., Streb, C. & Song, Y. F. ‘Wiring’ Redox-Active Polyoxometalates To Carbon Nanotubes Using a Sonication-Driven Periodic Functionalization Strategy. *Energy Environ. Sci.* **9**, 1095–1101 (2016).
28. Aji, W. W., Usami, Y., Hadiyawarman, Oyabu, R. & Tanaka, H. Frequency dependence dielectrophoresis technique for bridging graphene nanoribbons. *Appl. Phys. Express* **13**, (2020).
29. He, X. *et al.* Wafer-scale monodomain films of spontaneously aligned single-walled carbon nanotubes. *Nat. Nanotechnol.* **11**, 633–638 (2016).
30. Hodge, S. A., Bayazit, M. K., Coleman, K. S. & Shaffer, M. S. P. Unweaving the rainbow: A review of the relationship between single-walled carbon nanotube molecular structures and their chemical reactivity. *Chem. Soc. Rev.* **41**, 4409–4429 (2012).
31. Xu, Y. Q., Peng, H., Hauge, R. H. & Smalley, R. E. Controlled multistep purification of single-walled carbon nanotubes. *Nano Lett.* **5**, 163–168 (2005).
32. Marsat, G. & Maler, L. Neural heterogeneity and efficient population codes for communication signals. *J. Neurophysiol.* **104**, 2543–2555 (2010).

33. Rotman, Z. & Klyachko, V. A. Role of synaptic dynamics and heterogeneity in neuronal learning of temporal code. *J. Neurophysiol.* **110**, 2275–2286 (2013).
34. Inubushi, M. & Yoshimura, K. Reservoir Computing beyond Memory-Nonlinearity Trade-off. *Sci. Rep.* **7**, 1–10 (2017).
35. Goh, K. L., Fujii, H., Setiadi, A., Kuwahara, Y. & Akai-Kasaya, M. Spontaneous spike signals originated from redox-active molecules functionalised on carbon nanotubes. *Jpn. J. Appl. Phys.* **58**, (2019).
36. Vesicles, C., Salmon, T. & Carolina, N. (IgG) purification,. **267**, 1837–1840 (1995).
37. Legenstein, R. & Maass, W. What Makes a Dynamical System Computationally Powerful? in *New Directions in Statistical Signal Processing: From Systems to Brain* (MIT Press, 2007).  
doi:10.7551/mitpress/4977.003.0008
38. Legenstein, R. & Maass, W. Edge of chaos and prediction of computational performance for neural circuit models. *Neural Networks* **20**, 323–334 (2007).
39. Sohn, I. Small-World and Scale-Free Network Models for IoT Systems. *Mob. Inf. Syst.* **2017**, (2017).

## Chapter 4

### **Fourier transform waveforms via in-materio reservoir computing from single-walled carbon nanotube/porphyrin-polyoxometalate complex**

**Abstract:** This chapter shows the potential of our single-walled carbon nanotube/porphyrin-polyoxometalate (SWNT/Por-POM) complex for constructing different waveforms using in-materio reservoir computing (RC) learning architecture. The non-linear dynamical nature decodes an incident sin wave into high dimensional patterns of varied spatio-temporal outputs evident from the Lissajous plots. Changes in output amplitude, phase along with higher harmonic generation in the frequency space are observed network-wide. Such readouts linearly combined with optimized weights resulted in fruitful construction of multiple waveforms with highest accuracy of 99%. The task clearly depicts the materials ability to harness non-linearity for successful operation of sine wave Fourier series.

## 4.1 Introduction

A reservoir is considered a dynamical unit with pre-requisites of non-linearity and higher dimensionality.<sup>1,2</sup> In *Chapter 3* we have mentioned the SWNT/Por-POM's bottleneck of lower memory and higher non-linearity which clearly suggests that in-materio RC tasks of non-linear temporal sequences can be used as a benchmark to test the devices capability of replicating such unconventional architecture. One such task is related to the waveform generation, meaning constructing of different wave patterns from a sine wave of specific amplitude and frequency. Versatile physical systems based on atomic switch networks (ASN), SWNT/polymer composites and memristive delayed systems<sup>3-6</sup> have shown such task operation using similar in-materio RC platform. As the in-materio RC is a growing field, so in this aspect exploring such benchmark tasks with other available materials is also crucial in the field material science. Waveform generation is a mathematical formulation of Fourier series task. Infinite series of periodic sine trigonometric functions are linearly combined with coefficients to produce other form of complex periodic functions like triangular (Eq. 4.1), cosine (Eq. S4.2), sawtooth (Eq. 4.3) and square (Eq. 4.4).

$$Triangular = f(x) = \frac{8}{\pi^2} \sum_{i=1,3,5,\dots}^{\infty} \frac{(-1)^{\frac{(n-1)}{2}}}{n^2} \sin \left( \frac{n\pi x}{L} \right) \quad (4.1)$$

$$Cos = f(x) = \sin \left( \frac{\pi}{2} - x \right) \quad (4.2)$$

$$Sawtooth = f(x) = \frac{1}{2} - \frac{1}{\pi} \sum_{i=1}^{\infty} \frac{1}{n} \sin \left( \frac{n\pi x}{L} \right) \quad (4.3)$$

$$Square = f(x) = \frac{4}{\pi} \sum_{i=1,3,5,\dots}^{\infty} \frac{1}{n} \sin \left( \frac{n\pi x}{L} \right) \quad (4.4)$$

The complexity of the waveform increases as a function of the harmonics ( $n$ ) which determines the sine wave non-linearity ( $\nu$ ) as suggested previously in *Chapter 3 Eq. (3.4)*. For example, the cosine lacks a  $n$  term before sine and is only a phase shifted version of the sine wave hence requires mostly fundamental frequency to construct. Triangular, though requires multiple odd harmonics, but an  $n^2$  term in the denominator before sine makes it less non-linearly complex compared to square (odd  $n$ ) and sawtooth (odd and even  $n$ ). To understand this task complexity we hereby use our SWNT/Por-POM as an in-materio RC device for performance evaluation. We show in the subsequent sections of the RC operational principle and then move on to discuss the possible reason behind successfully implementing this task with our device.

## 4.2 Methods

### 4.2.1 SWNT/Por-POM dispersion

The SWNT/Por-POM dispersion was obtained using a known procedure.<sup>7</sup> Initially,  $2 \times 10^{-2} \text{ gL}^{-1}$  HiPCo SWNT, purified according to the previous report<sup>8</sup> and  $4 \times 10^{-2} \text{ gL}^{-1}$  of Por-POM<sup>9</sup> were first bath sonicated in ethanol for 1 h (40 k Hz) separately and then for 4 h by mixing them together. The dispersion was then centrifuged at 1,000 G for 15 min and the excess of supernatant was discarded. The precipitate was collected and was further bath sonicated in ethanol for 1 h to get the final dispersion.

### 4.2.2 Fabrication of MEA substrate

Aluminum coated MEA pattern was obtained via a standard photolithography process on a borosilicate glass substrate. A lift-off resist LOR-10A was first spin coated at 3,000 rpm for 50 s followed by the deposition of the photoresist S18186 spin-coated at 4,000 rpm for 2 s. The substrate was pre-baked at 90 °C for 5 min and the pattern was developed with a 25 s exposure to the UV light. Finally, the resist was developed using MF 319 developer for 90 s and 50 nm thick

aluminum metal was sputtered that produced the desire MEA substrate with inner circular pad diameter of 500  $\mu\text{m}$  and a pitch of 1.5 mm.

#### *4.2.3 Thin film deposition of SWNT/Por-POM computational material*

Thin film of SWNT/Por-POM random network was deposited onto the MEA pattern as per the previous report.<sup>10,11</sup> A vacuum-assisted wet transfer process was applied where 500  $\mu\text{L}$  of SWNT/Por-POM was filtered through a 1  $\mu\text{m}$  nitrocellulose paper and was placed on top of the MEA substrate with the SWNT/Por-POM facing down followed by its dissolution in acetone. The entire substrate with the thin film was dried using acetone vapors at 80  $^{\circ}\text{C}$  by placing it on a glass veil of acetone solution.

#### *4.2.4 Measurements*

The RC task of waveform generation was done using the custom built setup shown in *Chapter 2, section 2.8.2* without the current pre-amplifier, as we only took voltage readouts. Sine wave input was generated using the function generator (Agilent 33120A) and was fed to the device via one electrical probe. The outputs were collected via another probe and was readout by the PC using a high speed USB carrier (NI USB-9162) sampled at 1 kHz. All measurements were done at room temperature (28  $^{\circ}\text{C}$ ) and pressure. The detailed methods with corresponding schematic are discussed in *Chapter 2*.

The weight optimization of waveform RC task was all performed off-line with the Origin Pro 9.0 software via the multiple linear regression model. A training dataset of was collected to compute the weights and the device performance was evaluated on a different epoch section of the training data.



The Lissajous plots of input-output voltage relation was plotted by collecting the output sine waves from the device using the same hardware platform.

### 4.3 Results and discussion

Figure 4.1 displays the diagrammatic concept of carrying out the waveform generation task. For simplicity we have shown few pads in the MEA, but in reality an MEA with 12 pads are used for the experiment. An 11 Hz bipolar  $\pm 1$  V sine wave is firstly given as the input signal to one electrode pad (pink) which passes through the SWNT/Por-POM random network marked as black lines and green circles in the schematic. The signal creates a network wide impact, and as the Por-POM distribution is heterogeneous (*Chapter 3* AFM image *Fig. 3.2* confirms it), outputs of multiple patterns constituting the reservoir states  $X$  can be obtained from each of the electrode pads. The input signal was fed for 60 s and thus all the outputs collected had the same time length as the input. The set-up was so arranged that outputs were collected one at a time, as in only after the first 60 s data was collected, the probe was shifted to other electrode pad to continue the data collection procedure. A total of 2 s epoch was used for the data analysis with 1 s each for training and testing. An offline multiple linear regression<sup>12</sup> training approach was adopted, where the weights  $W_{out}$  of each of the reservoir states were optimized to fit the supervised target waves  $Y$ , using Eq. (4.5). The trained weights  $W_{out}$  were used to construct the test reservoir signal  $O(t)$  by a weighted linear combination of the reservoir states corresponding to  $m$  output electrodes Eq. (4.6). The  $m$  varied from 3 (minimum) to 7 to 11 (maximum) and the testing performance was evaluated by computing the normalized mean square error (NMSE) and the accuracy in Eq. (4.7) and Eq. (4.8) between the output  $O(t)$  and the target  $Y(t)$  over 1 s epoch.

$$W_{out} = (X^T X)^{-1} X^T Y \quad (4.5)$$

$$O(t) = \sum_{i=1}^m W_{out}^i X^i(t) \quad (4.6)$$

$$NMSE = \frac{\sum Y(t) - O(t)^2}{\sum Y(t)^2} \quad (4.7)$$

$$Accuracy = ((1 - NMSE) \times 100)\% \quad (4.8)$$

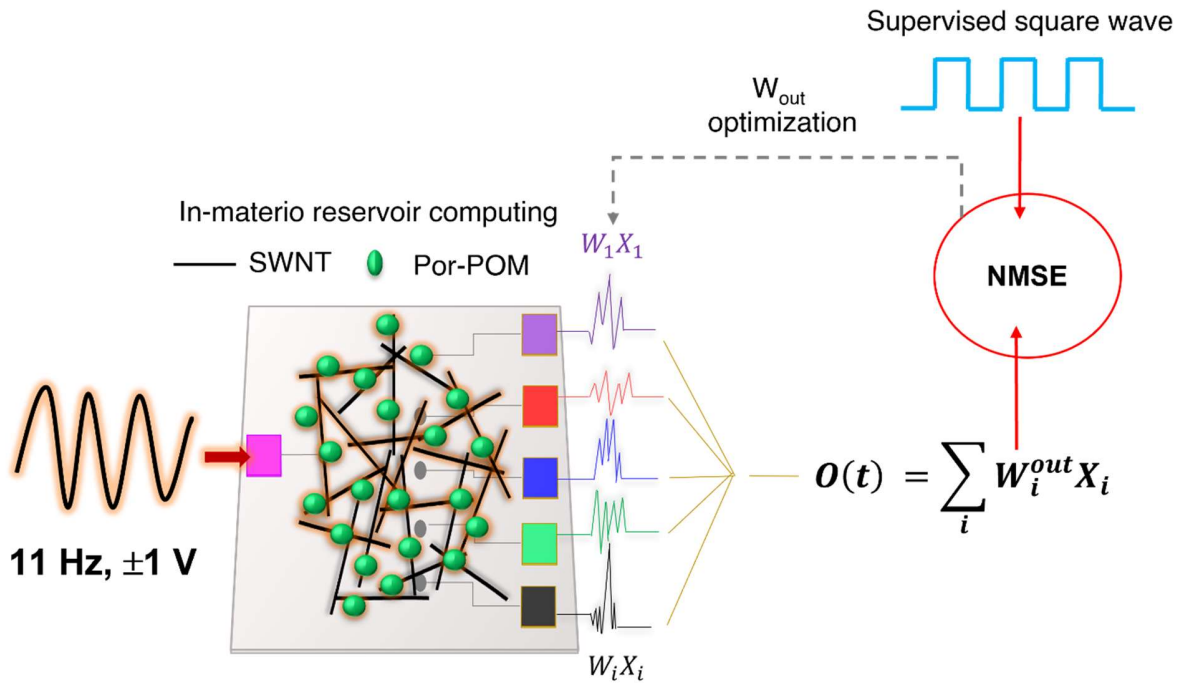


**Fig. 4.1** The RC operation for wave form generation task shown as an example for square wave supervised signal. The color coded pads imply sine wave outputs f different spatio temporal dimensions. In reality we use an MEA design with 12 total electrode pads, the diagram here just shows an illustration of the task technique.

Four different target waveforms of cosine, triangular, square, and sawtooth were performed for this operation as depicted in Fig. 4.2 by training eleven outputs. The triangular wave (Fig. 4.2a) showed the highest test accuracy of 99.4 % (red line) after training (green line) followed by cosine (99%, Fig. 4.2b), square (87%, Fig. 4.2c) and sawtooth (71%, Fig. 4.2d) in the decreasing order.

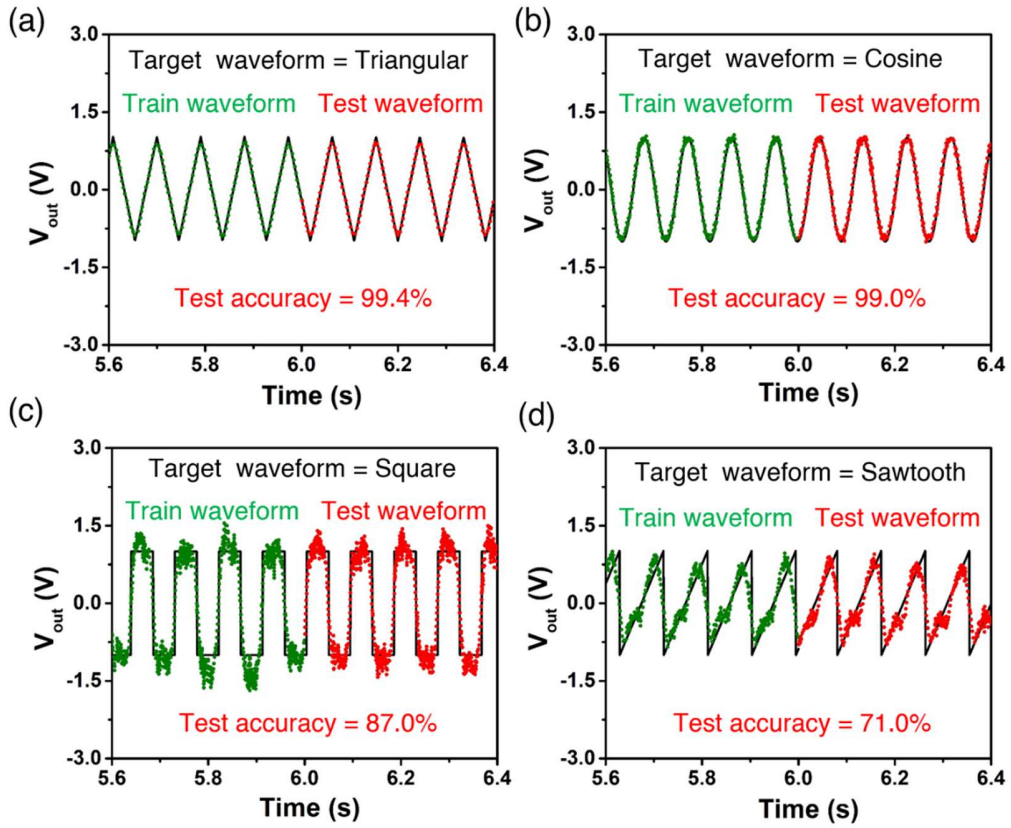


**Fig. 4.2.** Training and testing of waveform generation RC task by linear combination of sine wave outputs from SWNT/Por-POM reservoir when perturbed by a sine wave input of  $\pm 1$  V and 11 Hz. a) triangular, b) cosine, c) square, and d) sawtooth waveform generation RC task. Eleven output weights of 1 s epoch are first trained via supervised learning (green line), and the performance is evaluated via test waveform (red line) for the next 1 s epoch. The respective test fitting accuracy between the target (black line) and test data (red line) are given at the bottom.

To understand the reason behind the high accuracy machine learning performance we investigated the nature of the sine wave outputs relative to the input signal. This is important as it gives a clear picture of the non-linear high dimensional aspect of the reservoir required to perform such tasks with ease. Firstly we check the spatial dimensional change in terms of the amplitude for the outputs. Figure 4.3a shows the plot of the incident sine wave of amplitude  $\pm 1$  V that shows a smooth periodic motion. Upon passing through the SWNT/Por-POM computational material, change in output sine wave shapes can be observed in the consequent plots of Fig. 4.3b-e. The electrode pad colors (Fig. 4.3a) here indicate the outputs having the same nature of amplitude dimensional change. The simplest response comes from pad of  $O_1$  is Fig. 4.3b which retains the shape of the input with mostly 85% decrease the relative amplitude, calculated by Eq. (4.9), where  $A_{in}$  and  $A_{out}$  are the input and output sine wave amplitudes.

$$Relative\ amplitude = \frac{\Delta A}{A} = \frac{A_{in} - A_{out}}{A_{in}} \quad (4.9)$$

Fig. 4.3c shows slight distortion at the peaks of sine wave for output pads of  $O_2$ ,  $O_3$ ,  $O_5$  and  $O_8$  with amplitude attenuation of similar 85%. Along with these, larger distortion in sin wave shape and fluctuating peaks with phase delays can be observed in Fig. 4.3d-e for rest of the electrode pads with higher amplitude attenuation by about 98%. These result suggest that the random network structure produces multiple paths of different circuitry that results in varied degree of the incoming signal interaction with the material causing it to generate multi-dimensional spatial feature mappings.

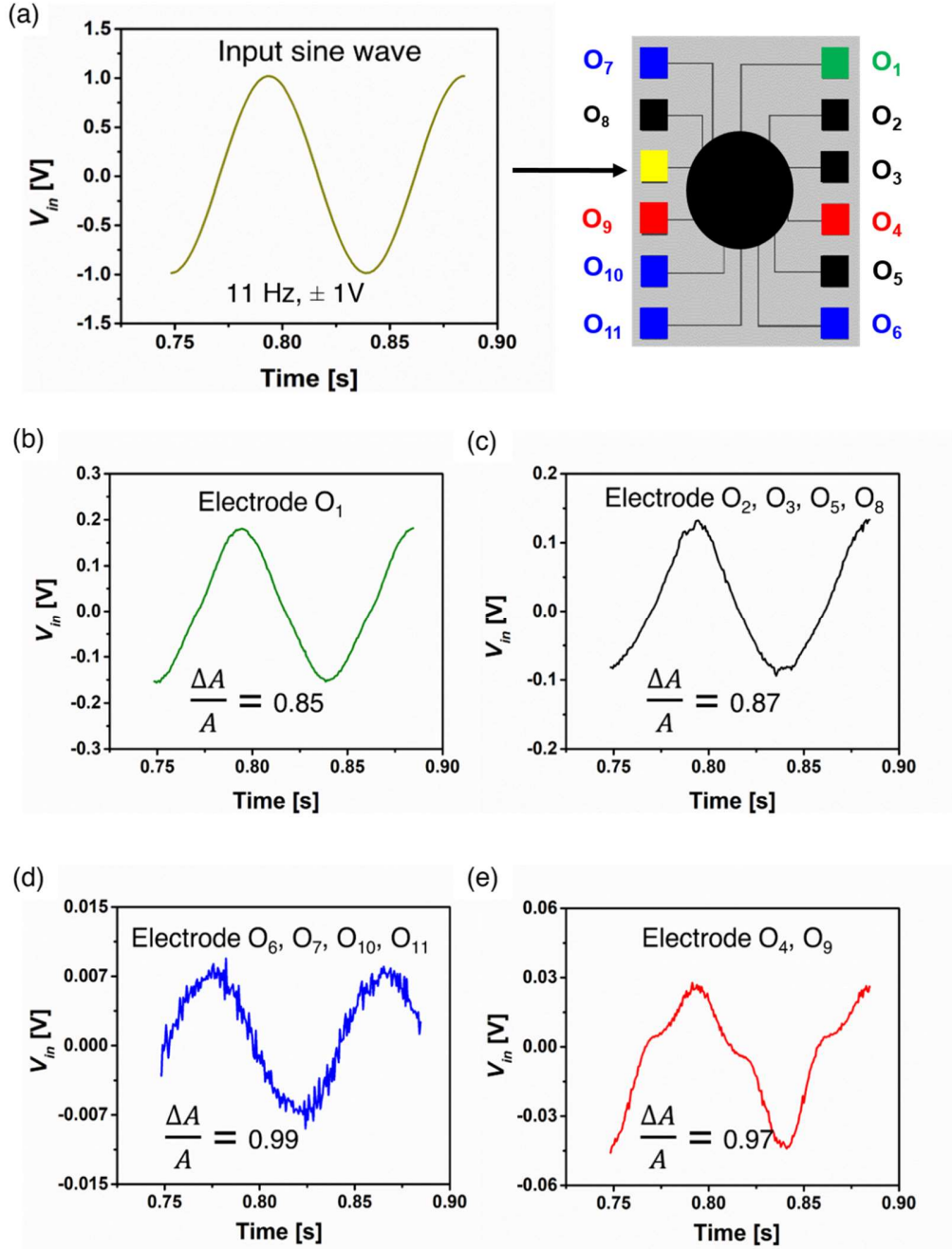


**Fig. 4.3.** Input and output sine waves from SWNT/por-POM network (a) The input sine wave  $\pm 1$  V and 11 Hz that was used to produce network wide reservoir output states when passed through the SWNT/por-POM MEA device (black circle). The color of the electrode pads indicate outputs of same nature. (b) In-phase output sine wave from electrode pad O<sub>1</sub>. (c) In-phase non-linear shaped sine wave from electrode pads O<sub>2</sub>, O<sub>3</sub>, O<sub>5</sub> and O<sub>8</sub>. (d) Phase change NDR like fluctuation sine wave outputs from electrode pads O<sub>6</sub>, O<sub>7</sub>, O<sub>10</sub> and O<sub>11</sub>. (e) Phase changed non-linear sine wave output from electrode pads O<sub>4</sub> and O<sub>9</sub>. The relative amplitude values as calculated from Eq. (4.9) are shown at the bottom of each graph.

In order to understand the internal dynamics happening at each nodal plots we studied the Lissajous plots (LP) in more detail<sup>13,14</sup>. LP is a graphical representation of input vs. output voltage ( $V_{in}$  vs  $V_{out}$ ) that analysis the networks linear and non-linear relationship between the two sine waves via a change in the amplitude, phase shift or frequency given by the Eq. (4.10) and Eq. (4.11), where  $A$ ,  $\omega$  are the input amplitude and frequency and  $a$ ,  $\omega'$  and  $\delta$  are the output amplitudes, frequencies, and phase delays, respectively.

$$x(t) = A \sin(\omega t) \quad (4.10)$$

$$x'(t) = a \sin(\omega' t + \delta) \quad (4.11)$$

A multitude of LP ( $V_{in}$  vs  $V_{out}$ ), color-coordinated with the output electrode pads in Fig. 4.3a, can be seen in Fig. 4.4a-d. Figure 4.4a,b shows the semi-linear and non-linear (in the input voltage window of -0.16 V to 0.15 V), nature of the output sine wave with attenuated amplitude and in-phase with the input similar to Fig. 4.3b,c. These profiles indicate that the input signal propagates through complex resistive network pathways with less non-linear redox activities thereby generating proportional changes in output amplitude signal. Higher dimensional profiles of distorted ellipse in Fig. 4.4c and non-linear ellipse in Fig. 4.4d coincidental with Fig. 4.3d-e are also visible. In these cases, the amplitude decrease is relatively high and are accompanied with multiple NDR like fluctuations with large hysteresis indicative of phase delay. Such phenomena can be attributed to the presence of more capacitive pathways along with resistive ones that allows a greater extent of charge-discharge cascading phenomena leading to such modulation of the output sine wave in terms of both amplitude and phase.

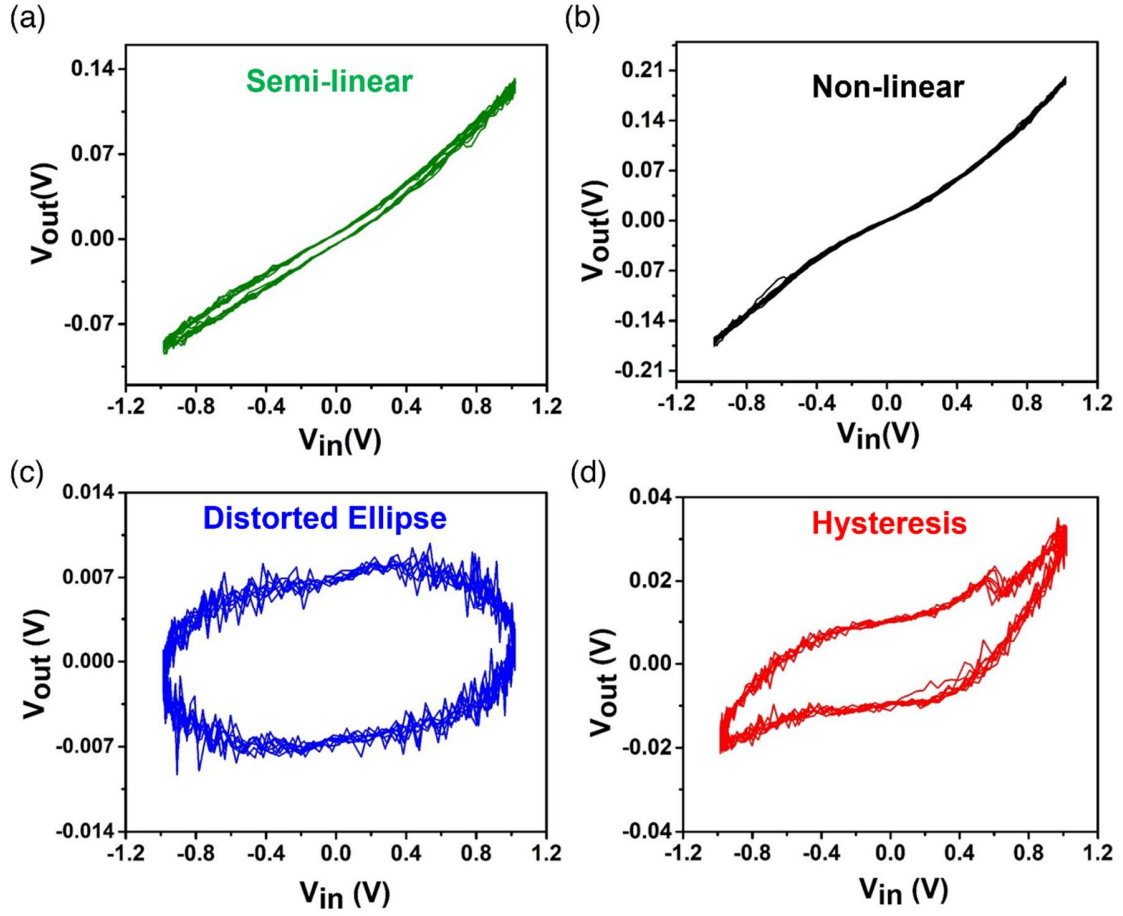


**Fig. 4.4.** SWNT/Por-POM complex network-wide dynamics via Lissajous representations. (a) Semi-linear Lissajous plot (LP) with no phase delay shows a proportional change in  $V_{out}$  amplitude relative to the  $V_{in}$  representative of resistive pathways. (b) The non-linear LP represents the charge-discharge phenomena occurring but with signals in phase with the input. (c) The elliptical and the (d) non-linear ellipse with NDR like fluctuations show phase delays corresponding to the complex capacitive network pathways. The color of the plots is coordinated with the electrode pads in Fig. 4.3a, indicating the outputs showing the same behavior.

The network wide spatial information decoding can be attributed to the non-homogenous size distribution of Por-POM over the SWNT confirmed from AFM in *Chapter 3*. The heterogeneity along with random network structure, creates varying degrees of cascading non-linear redox activity at different points in the network,<sup>11</sup> thereby generating pathways of different electrical properties of resistive or capacitive nature. Thin films of Por-POM have been shown to have such circuitry when studied under the electrical impedance spectroscopy (EIS) previously<sup>9</sup> confirming that even when adsorbed onto SWNT the behavior is retained as a result of which a mixture of LP's is generated from a single unit of SWNT/Por-POM with high dimensional information of the input in terms of amplitude and phase. The effect can also be seen in the temporal dimensions of the sine wave which are studied as frequency mappings via fast Fourier transformation of the output signals. Fig. 4.5b-e shows that for the outputs (Fig. 4.5b-e), as color coordinated, there are multiple even and odd harmonics present relative to the input (Fig. 4.5a) where only the presence of 11 Hz is seen. Second or higher order non-linearity are very much common in materials like Por-POM and SWNT when perturbed by an incident radiation because of the charge transfer and  $\pi$  electronic conjugation effect.<sup>15-21</sup> We believe that the functionalization brings around a synergistic effect within the network thus making the system more dynamical and complex in nature allowing for its excellent performance towards waveform generations as the Fourier transform of sine waves seen from Eq. (4.1)-(4.4) also demands such properties.



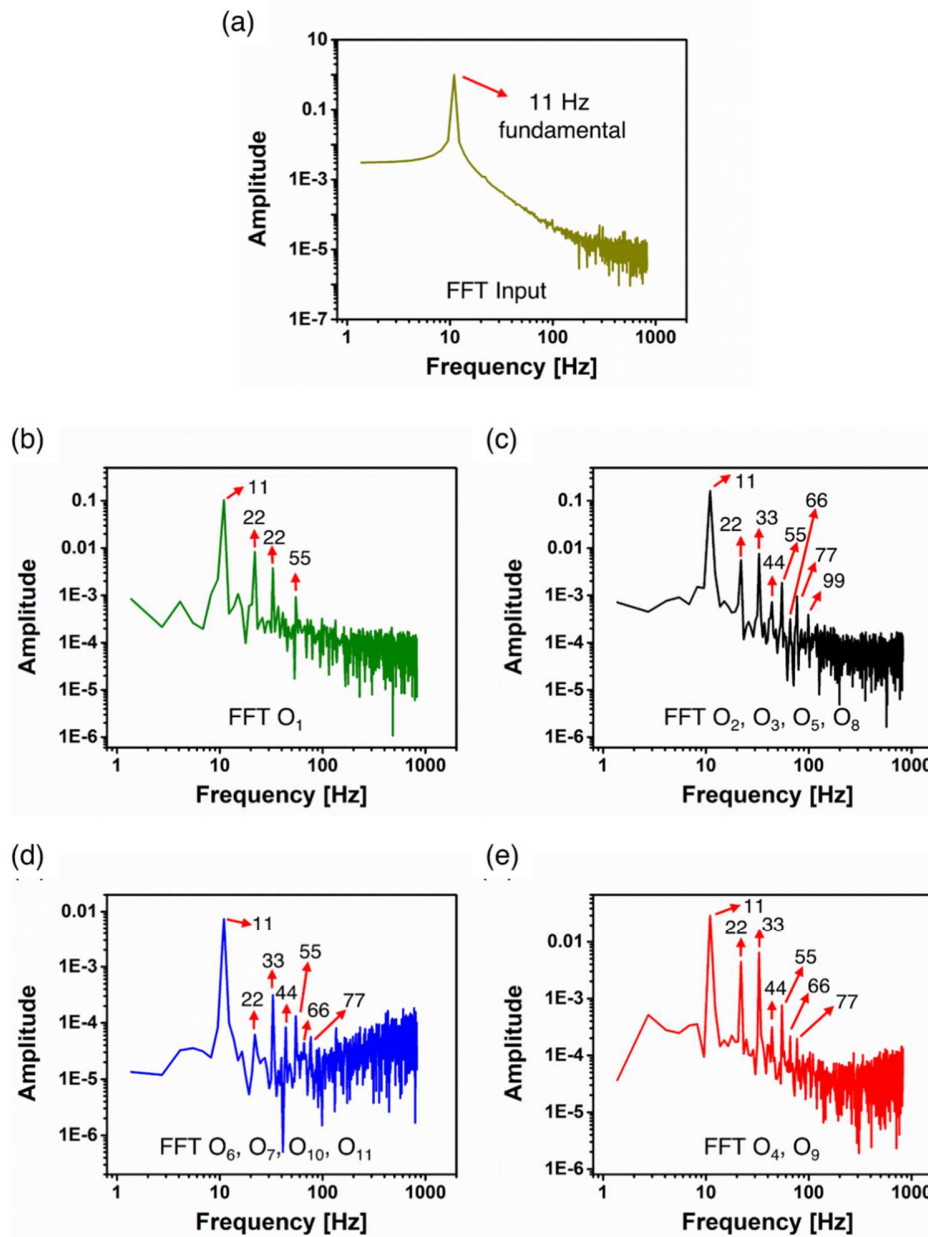


**Fig. 4.5.** Higher harmonic generation (HHG) of input and output sine waves. (a) HHG obtained by FFT analysis of input sin wave which shows only the fundamental 11 Hz frequency. (b) HHG of the output sin wave from  $O_1$ . (c) HHG of the output sin wave from  $O_2$ ,  $O_3$ ,  $O_5$  and  $O_8$ . (d) HHG of the output sin wave from  $O_6$ ,  $O_7$ ,  $O_{10}$  and  $O_{11}$ . (e) HHG of the output sin wave from  $O_4$  and  $O_9$ . All the FFT's were performed using Origin Pro 9.0 software and are plotted as log-log scale. The colors of FFT are coordinated with the sine waves in Fig. 4.3. Compared to the input, each output produced HHG of both odd and even harmonics indicating decoding of input via the materials innate recurrent connection arising from SWNT/Por-POM's non-linear dynamics.

To validate the importance of the non-linear rich reservoir states towards waveform generation, the SWNT/Por-POM reservoir performance was also evaluated with a lower number of training outputs as shown in Fig. 4.6-4.7. Electrode pads of  $O_1$  to  $O_7$  and  $O_1$  to  $O_3$  (Fig. 4.3a) were sequentially chosen to perform the task shown in Fig. 4.6 (seven outputs) and Fig. 4.7 (three outputs). A clear drop in the test accuracy of three outputs for cosine, square and sawtooth can be seen in Fig. 4.7e with the triangular being least affected as these can be replicated easily with fundamental and lower addition of odd harmonics due to their high resemblance to sine wave shape. On the contrary, complex waveforms like square and sawtooth with steep edges failed for the linear combination of three outputs but retained their shape for the seven outputs. This is because, as suggested from the Fourier series equations, greater the presence of linear outputs of higher harmonics and spatial decoded information in terms of phase and amplitude better will be the performance. Similarly, the cosine which requires only the fundamental sine harmonics showed a steep drop at three output combination as they lacked the phase delayed dynamics (Fig. 4.4a,b) which is important to convert the sine wave outputs into the cosine forms. The above result thus puts emphasis on the fact that for a reservoir to learn different time-series waveform targets efficiently, presence of non-homogeneous network distribution<sup>22,23</sup> with high charge transfer dynamics is vital as these give rise to multiple spatio-temporal dimensional patterns of amplitude, phase and frequency when instigated by an external sine wave input. The in-materio dynamics contained in each of the readouts rather represents the contrasting computational regime of reservoir states emerging from the random network of SWNT/Por-POM, hence enabling it to carry out the unconventional RC task of supervised learning.

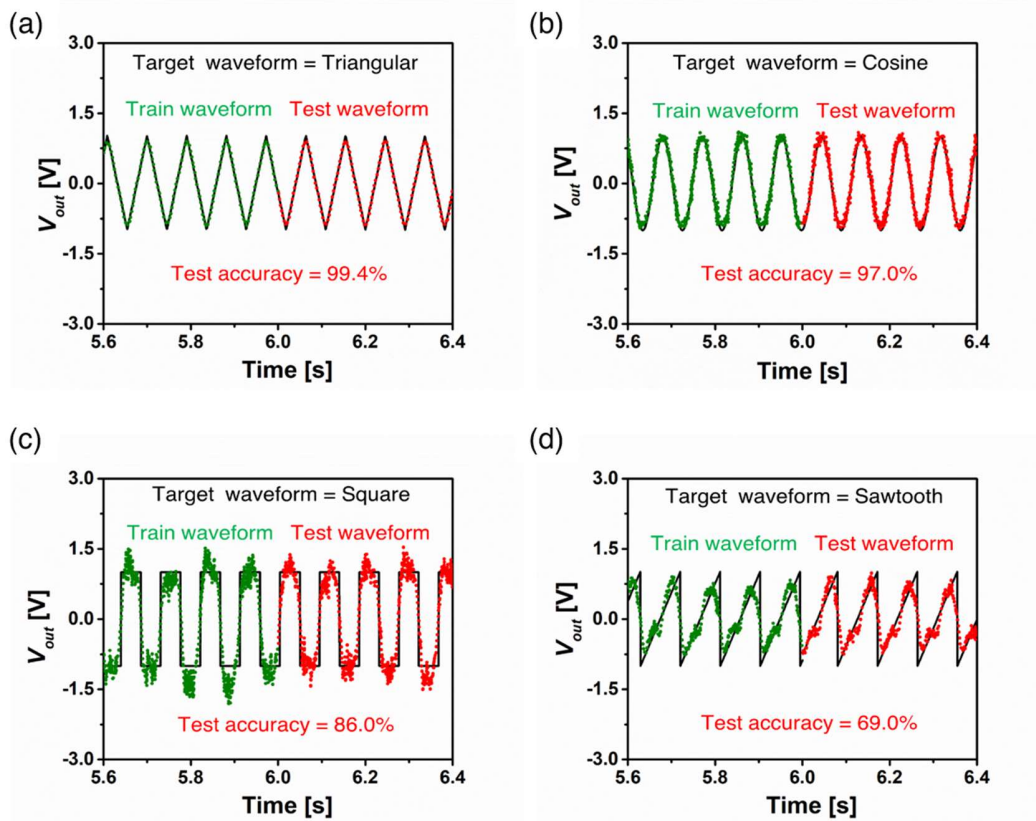


**Fig. 4.6.** Waveform generation from training 7 outputs of the output sin wave. The train data (green dotted line) and the test data (red dotted line), each with an epoch of 1 s are plotted against the target wave (black line) for (a) triangular, (b) cosine, (c) square, and (d) sawtooth. Training weights over 1 s epoch are used for fitting the test data over another 1 s epoch. The corresponding test accuracies calculated from normalized mean square error (NMSE, Methods) is represented at the bottom of each graph.

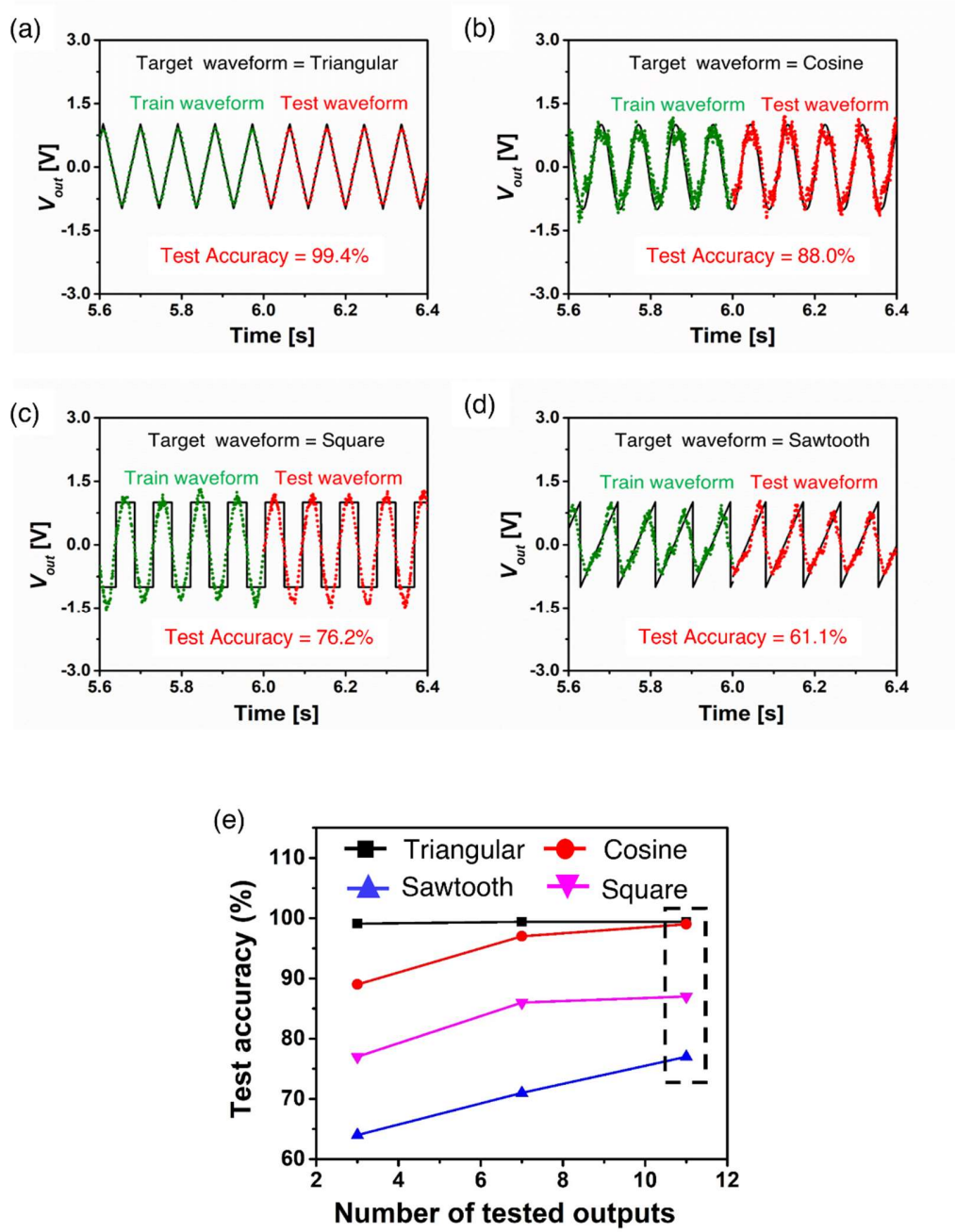


**Fig. 4.7.** Waveform generation from training 3 outputs of the output sin wave. The train data (green dotted line) and the test data (red dotted line), each with an epoch of 1 s are plotted against the target wave (black line) for (a) triangular, (b) cosine, (c) square, and (d) sawtooth. (e) Plot of test accuracy against the number of tested linearly combined output electrode pads. Training weights over 1 s epoch are used for fitting the test data over another 1 s epoch. The corresponding test accuracies calculated from normalized mean square error (NMSE, Methods) is represented at the bottom of each graph.

#### 4.4 Conclusion

In summary, we concluded that the first in-materio RC benchmark task of single input non-linear complex function prediction from a dynamical unit of SWNT/Por-POM was successfully achieved. The fundamental reason being the combined effect of non-linear charge dynamics arising from the SWNT/Por-POM. The complex network showed varied Lissajous plots (LP) manifesting in a network of different electronic components within a single unit. The interconnected resistive-capacitive pathways created from easy solution processible sonicated driven heterogeneous functionalization lead to differentiating nodal points of high dimensional spatio-temporal patterns in amplitude, phase and frequency space. The LP attractors followed the same pattern over time indicating the presence of recurrent connections leading to varied computational regimes. All these properties allowed us to exploit the voltage readouts and linearly combine them to construct triangular, cosine, square and sawtooth waveforms with a simple linear regression output layer weight training. The device retained its performance over lower number of seven outputs and gradually showed a decayed performance for three outputs indicating the fault tolerant nature. It suggests that even in the failure of multiple output nodes the device still performs and computes the optimization validating the RC platform to be a robust, simple, efficient and fault-tolerant computational architecture.

## References

1. Nakajima, K. Physical reservoir computing—an introductory perspective. *Jpn. J. Appl. Phys.* **59**, 060501 (2020).
2. Tanaka, G. *et al.* Recent advances in physical reservoir computing: A review. *Neural Networks* **115**, 100–123 (2019).
3. Demis, E. C. *et al.* Nanoarchitectonic atomic switch networks for unconventional computing. *Jpn. J. Appl. Phys.* **55**, (2016).
4. Hadiyawarman *et al.* Performance of Ag-Ag<sub>2</sub>S core-shell nanoparticle-based random network reservoir computing device. *Jpn. J. Appl. Phys.* **60**, (2021).
5. Kotooka, T. *et al.* Ag<sub>2</sub>Se Nanowire Network as an Effective In-Material Reservoir Computing Device. 1–20 doi:10.21203/rs.3.rs-322405/v1
6. Zhong, Y. *et al.* Dynamic memristor-based reservoir computing for high-efficiency temporal signal processing. *Nat. Commun.* **12**, 1–9 (2021).
7. Hu, J., Ji, Y., Chen, W., Streb, C. & Song, Y. F. ‘Wiring’ Redox-Active Polyoxometalates To Carbon Nanotubes Using a Sonication-Driven Periodic Functionalization Strategy. *Energy Environ. Sci.* **9**, 1095–1101 (2016).
8. Aji, W. W., Usami, Y., Hadiyawarman, Oyabu, R. & Tanaka, H. Frequency dependence dielectrophoresis technique for bridging graphene nanoribbons. *Appl. Phys. Express* **13**, (2020).

9. Yamazaki, Y., Yamashita, K., Tani, Y., Aoyama, T. & Ogawa, T. Structure determination and negative differential resistance of tetraarylporphyrin/polyoxometalate 2 : 1 complexes. *J. Mater. Chem. C* **8**, 14423–14430 (2020).
10. He, X. *et al.* Wafer-scale monodomain films of spontaneously aligned single-walled carbon nanotubes. *Nat. Nanotechnol.* **11**, 633–638 (2016).
11. Tanaka, H. *et al.* A molecular neuromorphic network device consisting of single-walled carbon nanotubes complexed with polyoxometalate. *Nat. Commun.* **9**, 1–7 (2018).
12. Lukoševičius, M. & Jaeger, H. Reservoir computing approaches to recurrent neural network training. *Comput. Sci. Rev.* **3**, 127–149 (2009).
13. AL-KHAZALI, H. A. H. Geometrical and Graphical Representations Analysis of Lissajous Figures in Rotor Dynamic System. *IOSR J. Eng.* **02**, 971–978 (2012).
14. Scharnhorst, K. S. *et al.* Atomic switch networks as complex adaptive systems. *Jpn. J. Appl. Phys.* **57**, 1–6 (2018).
15. Ul Hassan, S. *et al.* ‘Closer is better and two is superior to one’: Third-order optical nonlinearities of a family of porphyrin-anderson type polyoxometalate hybrid compounds. *J. Phys. Chem. C* **120**, 27587–27599 (2016).
16. Liu, X. M. *et al.* Two new isolated Zn- $\epsilon$ -Keggin clusters modified by conjugated organic ligands with decent electrocatalytic and third-order NLO properties. *Dalt. Trans.* **49**, 14251–14257 (2020).

17. Shi, Z. *et al.* New supramolecular compounds based on porphyrin and polyoxometalate: Synthesis, characterization and nonlinear optical and optical limiting properties. *RSC Adv.* **4**, 50277–50284 (2014).
18. Slepyan, G. Y. *et al.* Highly efficient high-order harmonic generation by metallic carbon nanotubes. *Phys. Rev. A - At. Mol. Opt. Phys.* **60**, R777–R780 (1999).
19. Belonenko, M. B., Glazov, S. Y. & Meshcheryakova, N. E. Influence of constant electric field on generation of higher harmonics in semiconductor carbon nanotubes. *Opt. Spectrosc. (English Transl. Opt. i Spektrosk.* **108**, 774–779 (2010).
20. Slepyan, G. Y., Maksimenko, S. A., Kalosha, V. P., Gusakov, A. V. & Herrmann, J. High-order harmonic generation by conduction electrons in carbon nanotube ropes. *Phys. Rev. A - At. Mol. Opt. Phys.* **63**, 10 (2001).
21. Trolle, M. L. & Pedersen, T. G. Second harmonic generation in carbon nanotubes induced by transversal electrostatic field. *J. Phys. Condens. Matter* **25**, 325301 (2013).
22. Perez-Nieves, N., Leung, V. C. H., Dragotti, P. L. & Goodman, D. F. M. Neural heterogeneity promotes robust learning. *bioRxiv* 1–22 (2020).  
doi:10.1101/2020.12.18.423468
23. Lengler, J., Jug, F. & Steger, A. Reliable neuronal systems: The importance of heterogeneity. *PLoS One* **8**, (2013).



## Chapter 5

### **Room temperature demonstration of in-materio reservoir computing for optimizing Boolean function with single-walled carbon nanotube/porphyrin-polyoxometalate composite**

**Abstract:** The chapter deals with the in-materio RC operation of single walled carbon nanotube/porphyrin-polyoxometalate network (SWNT/Por-POM) towards six Boolean logic supervised targets. By training only once and computing the weighted linear combination of high dimensional voltage readouts, a device accuracy greater than 90% is achieved which is robust against any time length and multiple test datasets owing to the echo-state property and faultless information processing. Moreover, a non-zero machine intelligence index confirms that the current dynamics contain negative differential resistance which makes the SWNT/Por-POM act as a mathematical additive and subtractive unit aiding it in constructing such complex Boolean functions.

## 5.1 Introduction

Evolution of neural network (NN) architecture<sup>1),2)</sup> has made brain-inspired computing a possibility in today's age on conventional von Neumann architectures with constructed algorithms. Although a step stone in the field of machine intelligence but processing stacks of data requires heavy CMOS circuitry and multiple electronic components to come at par with brain's computational efficiency. Both of these factor are challenging as downscaling devices are reaching its limit rapidly<sup>3)-5)</sup> along with data transfer latency due to von Neumann bottleneck.<sup>6)</sup> To overcome this, alternative research work termed as unconventional computing are being adopted where the NN models are replicated on a hardware platform.<sup>7)-9)</sup> The goal of such adaptation is to exploit the internal non-linear information dynamics, store the processed data within the same hardware unit and lastly utilize this data for training a given task via a simplified and time-efficient learning platform. One such NN platform that closely resemble the aforementioned unconventional architecture is reservoir computing.<sup>10)-12)</sup> It is a class of recurrent neural network<sup>13)</sup> with a single layer of recurrently connected non-linear neuronal units called the reservoir. Time-varying input information is mapped to high dimensional linear output readouts via the reservoir states of fixed arbitrary weights. These states are then supervised to learn a given task by optimizing the output weights only and thus any target task can be constructed by just performing a weighted linear combination of all the outputs following the echo state network principle.<sup>12)</sup> In the context of unconventional computing, non-temporal task of logic function optimization has been a benchmark over the years.<sup>14)-17)</sup> In-materio computation of Boolean operations with single-walled carbon nanotube (SWNT)/polymer composite, dopant atomic network (DAN) and atomic switch networks (ASN) has been implemented successfully using either evolutionary algorithm (EA) or off-line RC supervised learning.<sup>18)-20)</sup> Since in all these cases the intrinsic non-linear dynamics in terms of

current or voltage readouts are exploited to achieve the desired Boolean task, so the platform of experimentally exploring other materials of similar dynamics remains open and unlimited. Recently, SWNT coupled with polyoxometalates (POM) has surfaced up as a neuronal spike based neuromorphic device due to the multiple redox states of POM.<sup>21)</sup> They have shown theoretically, that by utilizing the random fluctuations of the dynamical system an in-materio RC with FORCE learning can be developed to carry out time-series tasks of NARMA 10, thereby reducing the time complexity required for brutal EA based search algorithms for similar materials. The property of self-randomness and non-linearity with functionalized SWNT is very much inherent unlike ASN and DAN which requires pre-activation or low temperature conditions to compute. This makes it necessary that such functionalized SWNT composites be further exploited for unconventional RC framework physically. Based on the previous report, herein we use SWNT/Porphyrin-POM (SWNT/Por-POM hereafter) complex for in-materio RC Boolean function optimization problem. Por-POM ( $\text{SV}_2\text{W}_{10}\text{O}_{40}[\text{H}_4\text{TPP}]$ ) has been extensively studied for its non-linear properties arising from the charge transfer of porphyrin to POM.<sup>22),23)</sup> The thin films of these Keggin molecules possess resistive-capacitive circuit pathways, hence manifesting in a negative differential resistance (NDR) behavior, proven to be useful for non-linear machine intelligent task of Boolean logic optimizations.<sup>24)</sup> Thus in this study, we demonstrate the usefulness of SWNT/Por-POM towards Boolean logic construction by harnessing the network wide non-linear dynamics mapped into high dimensional space of voltage readouts via the off-line supervised technique. We achieve this by fabricating the SWNT/Por-POM computational material network on a photo lithographically patterned multi electrode array (MEA, see Methods) system.

Figure 5.1 depicts the schematic of the entire set-up with MEA interfaced with PC for controlling input-output operations, thus allowing for an easy hardware interface platform for realization of room temperature in-materio RC Boolean task.

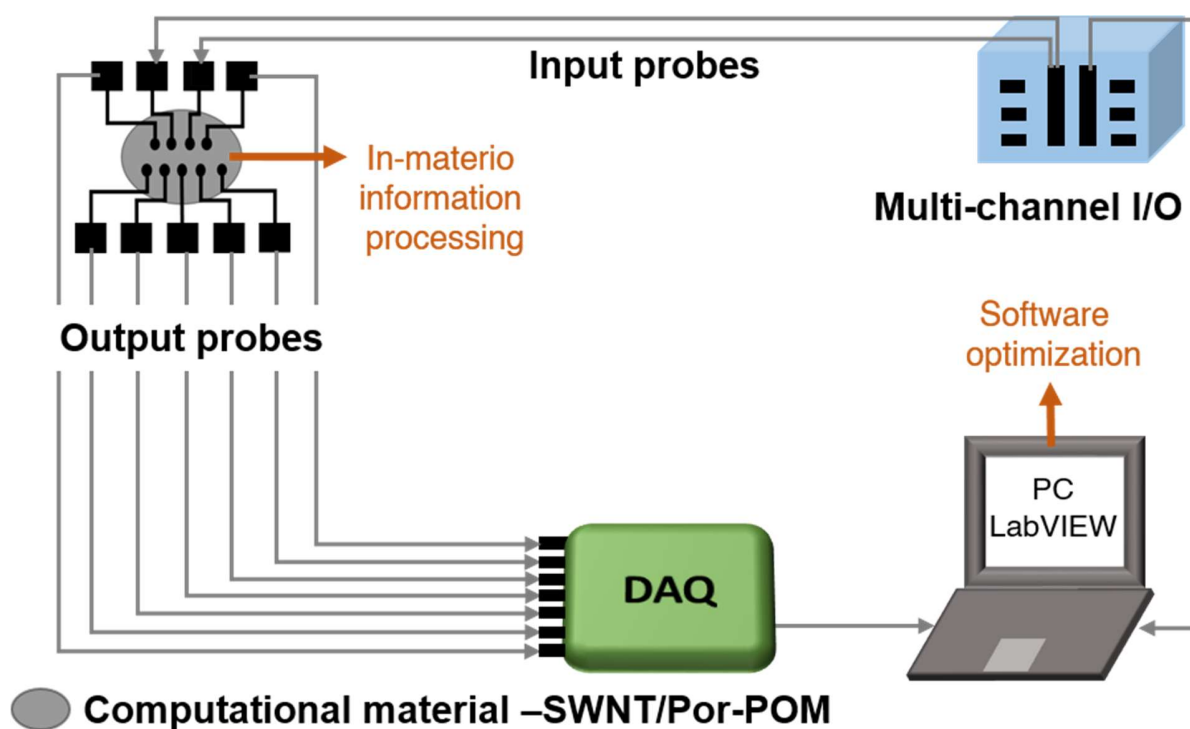


**Fig. 5.1** Schematic of the experimental set-up to carry out the in-materio RC operation with MEA electrode (left) interfaced with PC (right) via the I/O multi-channel readout and DAQ system. The computational material used here is SWNT/Por-POM.

## 5.2 Methods

### 5.2.1 SWNT/Por-POM dispersion

The SWNT/Por-POM dispersion was obtained using a known procedure.<sup>25)</sup> Initially,  $2 \times 10^{-2}$  gL<sup>-1</sup> HiPCo SWNT, purified according to the previous report,<sup>26)</sup> and  $4 \times 10^{-2}$  gL<sup>-1</sup> of Por-POM were first bath sonicated in ethanol for 1 h (40 k Hz) separately and then for 4 h by mixing them together. The dispersion was then centrifuged at 1,000 G for 15 min and the excess of supernatant was discarded. The precipitate was collected and was further bath sonicated in ethanol for 1 h to get the final dispersion.

### 5.2.2 Fabrication of MEA substrate

Aluminum coated MEA pattern was obtained via a standard photolithography process on a borosilicate glass substrate. A lift-off resist LOR-10A was first spin coated at 3,000 rpm for 50 s followed by the deposition of the photoresist S18186 spin-coated at 4,000 rpm for 2 s. The substrate was pre-baked at 90 °C for 5 min and the pattern was developed with a 25 s exposure to the UV light. Finally, the resist was developed using MF 319 developer for 90 s and 50 nm thick aluminum metal was sputtered that produced the desire MEA substrate with inner circular pad diameter of 500  $\mu$ m and a pitch of 1.5 mm.

### 5.2.3 Thin film deposition of SWNT/Por-POM computational material

Thin film of SWNT/Por-POM random network was deposited onto the MEA pattern as per the previous report.<sup>21)</sup> A vacuum-assisted wet transfer process was applied where 500  $\mu$ L of SWNT/Por-POM was filtered through a 1  $\mu$ m nitrocellulose paper and was placed on top of the MEA substrate with the SWNT/Por-POM facing down followed by its dissolution in acetone.

The entire substrate with the thin film was dried using acetone vapors at 80 °C by placing it on a glass veil of acetone solution.

#### 5.2.4 Measurements

The I-V characteristic was measured using a probe system (Pascal Co., Ltd) with a semiconductor parameter analyzer (Agilent 4156B) using a DC bias swept at 25 mVs<sup>-1</sup>. The RC task for Boolean logic function was done using the custom-built setup shown in Fig. 5.1. The set-up is somewhat described in *Chapter 2 section 2.8.2* is similar but since we are using two inputs, so we used a different configuration (see Methods). The two binary inputs of random '0' and '1' was generated using the LabVIEW program and was fed to the device via two electrical probes interfaced with a multifunctional I/O DAQ system (NI PXIe-4141) instead of a function generator. The outputs were collected via another probe and was readout by the PC using a high-speed USB carrier (NI USB-9162) sampled at 1 kHz. All measurements were done at room temperature (28 °C) and pressure. The detailed methods with corresponding schematic are discussed in *Chapter 2*.

The weight optimization of Boolean logic RC task was all performed off-line with the Origin Pro 9.0 software via the multiple linear regression model. A training dataset of 1 min was collected to compute the weights and the device performance was evaluated using five different datasets collected individually for a similar interval of 1 min epoch.

The machine intelligence index is calculated by firstly converting the  $I_{out}$ - $V_{in}$  plot into its differential form that results in conductance ( $dI_{out}/dV_{in}$ ). The  $dI_{out}/dV_{in}$  was then smoothed using Savitzky-Golay method<sup>24)</sup> in order to reduce the noise and enhance the signal peaks for proper calculation. The entire procedure was done using the Origin pro 9.0.

### 5.3 Results and discussion

Figure 5.2a schematically depicts the RC task of Boolean logic function optimization for an XOR gate as an example. Two binary functions of randomized ‘0’ and ‘1’ are first given as voltage inputs,  $V_{in1}$  and  $V_{in2}$ , to two electrode pads of the MEA consisting of the random network of SWNT (black line)/Por-POM (pink circles). The two inputs are sampled at 1 bit/s and are chosen to create 4 states of inputs in the form of (0,0), (0,1), (1,0) and (1,1), depicting the mathematical inputs of a logic table as shown in Fig. 5.2b. In this experiment we have used 0 V to represent the logic ‘0’ low state while +2 V as the logic ‘1’ high state. The resultant random fluctuation of non-linear high dimensional outputs, arising from the SWNT/Por-POM redox mediated dynamics, are then collected as reservoir states  $O_i$  depicted in Fig. 5.2c. A total of  $i$  equal to seven electrode pads (Fig. 5.2a) are used in our case which are color coordinated with the outputs in Fig. 5.2c. Each output in Fig. 5.2c shows a step-wise increasing of  $V_{out}$  signal and are representative of each state of the combined input signals, where the lowest and the highest  $V_{out}$  relates to the (0,0) and (0,1) input states with the intermediate  $V_{out}$  values being representative of the (1,0) and (0,1) input states. It is evident that these output responses are thus mappings of the input and its recent past states which evolves non-linearly with time and thus suggests the SWNT/Por-POM’s ability to process input driven spatio-temporal information, a fundamental necessity of a dynamical reservoir system.<sup>27)</sup> In RC, the machine intelligence task is achieved by training only the output weights  $w_i^y$  with a specific supervised target signal  $Y(t)$ <sup>28)</sup> as shown in Fig. 5.2a for the XOR logic gate, where the output represents a state ‘1’ only when either of  $V_{in1}$  or  $V_{in2}$  is high, otherwise it outputs a ‘0’. A multiple linear regression is adapted to train the weights off-line using the Moore-Penrose pseudo inverse algorithm in the Origin Pro 9.0 given by Eq. (5.1). The algorithm is a generalization of inversion matrix for computing the best fit  $w_i^y$  to a set of linear reservoir readouts  $O_i$  when operated

on its transpose form  $O_i^T$ . The trained  $w_i^y$  are used to construct the reservoir signal  $Z(t)$  via a weighted linear combination added to a bias term  $b_0$  as per Eq. (5.2) and the best fit between  $Z(t)$  and  $Y(t)$  is obtained by minimizing the mean square error (MSE) (Fig. 5.2a) over  $N$  data points given in Eq. (5.3). The ultimate device performance with  $Y(t)$  is further evaluated from the accuracy given in Eq. (5.4), where now the trained  $w_i^y$  are instead linearly combined with readouts of a different test dataset driven by the same input sequence.

$$w_i^y = (O_i^T O_i)^{-1} O_i^T Y \quad (5.1)$$

$$Z(t) = \sum_{i=1}^m w_i^y O_i(t) + b_0 \quad (5.2)$$

$$MSE = \frac{\sum Y(t) - Z(t)^2}{N} \quad (5.3)$$

$$Accuracy = ((1 - MSE) \times 100)\% \quad (5.4)$$



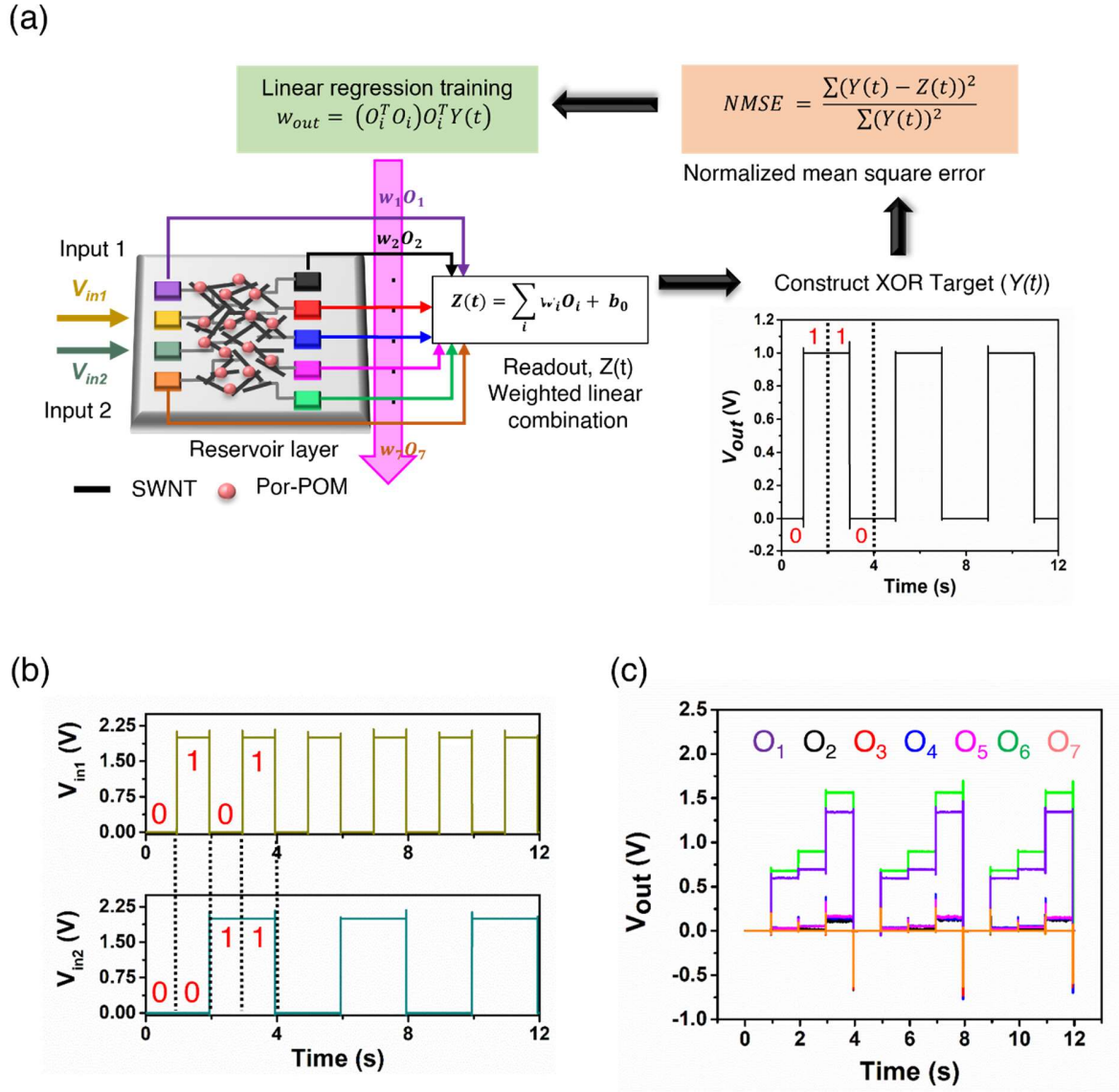


**Fig. 5.2** Boolean function RC operation task procedure with (a) showing the operational architecture of RC. Two voltage inputs  $V_{in1}$  and  $V_{in2}$  perturb the SWNT (black line)/Por-POM (red circles) random network structure to give voltage readouts  $O_i$  from seven color coded electrodes. The output weights  $W_{out}$  are trained with a supervised signal, e.g. XOR function (truth logic of two high and low output states (1,1) and (0,0) and are optimized via linear regression till the mean square error is minimized. (b) The two binary inputs  $V_{in1}$  and  $V_{in2}$ . Of four states; (0,0), (1,0), (0,1) and (1,1). (c) The high dimensional outputs obtained from each electrodes color coded with the pads shown in (a). These readouts are trained as depicted in the schematic.

The above method was applied firstly used to train the six well know Boolean logic functions over an epoch of 12 s and was analyzed for a given test dataset as shown in Fig. 5.3. All the target logic gates (black line) of OR (Fig. 5.3a), AND (Fig. 5.3b), XOR (Fig. 5.3c), NOR (Fig. 5.3d), NAND (Fig.5.3e), and XNOR (Fig. 5.3f) were replicated by the linear combination of test readouts (blue dots) indicating the successful implementation of in-materio RC based on the echo-state network learning architecture.<sup>29)</sup> Although the test waves followed their respective targets, however appearance of noise fluctuations for all the gates at the steep edges transitioning from '0' to '1' state, similar to the outputs (Fig. 5.2c), can be observed. A plausible reason can be attributed to the sudden change in the device capacitance requiring time to adjust to the given voltage state when such linear drop in the voltage occurs, because of which the weight adjustments on those parts give out noisy fitting. It is to be noted that the behavior is more prominent for XOR and XNOR as these gates are exclusively complex and difficult to optimize relative to their counterparts right at the edges as validated by the assembly of nanoparticle network as well.<sup>19)</sup>

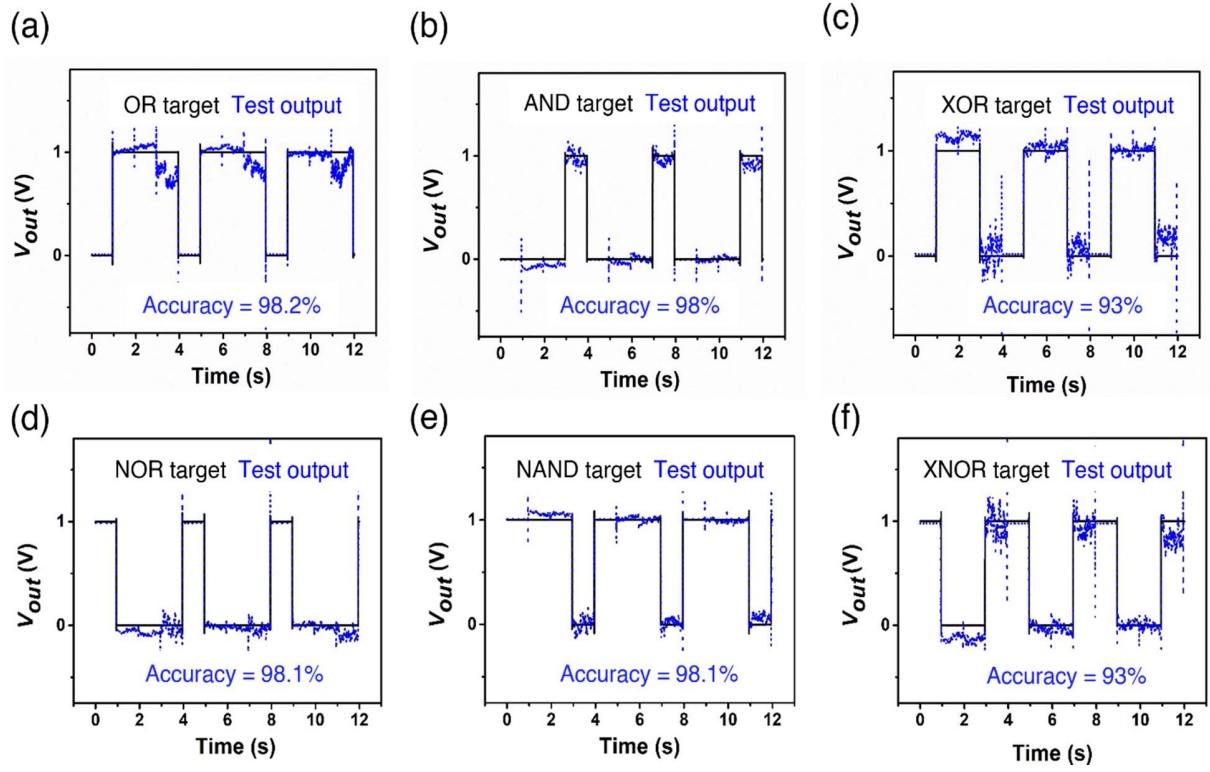


**Fig. 5.3** Construction of Boolean logic target functions (black) from weighted linear combination of voltage readouts after output weight training by supervised learning for (a) OR, (b) AND, (c) XOR, (d) NOR, (e) NAND and (f) XNOR with their respective test accuracy fitting values at the bottom of each plot.

The formulation of varied Boolean targets portray the RC advantage of multitasking,<sup>30)</sup> where target specific tasks can be achieved from a single unit of SWNT/Por-POM reservoir upon driven by the same input sequence. This characteristic feature is highly evident when one assesses the training weight distribution plots of different electrode pads for all the gates in Fig. 5.4a. The bar plots for each gates (color coded) show a clear distinction amidst each other indicating that each task certainly can be learned uniquely and permanently with ruling out the possibility of catastrophic interference learning<sup>31)</sup> owing to the output layer only learning method. In order to quantitatively understand the trained weights capability towards the device performance, we gauged the accuracy factor in Eq. (5.4) over five test datasets for 12 s epoch. Figure 5.4b shows the column plot of test accuracy for all the gates with the error bars corresponding to the standard deviation (SD) among the datasets. An accuracy greater than 95% is achievable for OR, AND, NOR and NAND gates with a slightly lower than 95% for the XOR and XNOR gates. The result is consistent with Fig. 5.3 where the XOR and XNOR shows a mismatch in following the horizontal lines compared to the other gates. The difference is evitable as XOR and XNOR are deemed to be linearly inseparable compared to the other gates<sup>32)</sup> and hence requires high dimensional space to par up their performance.

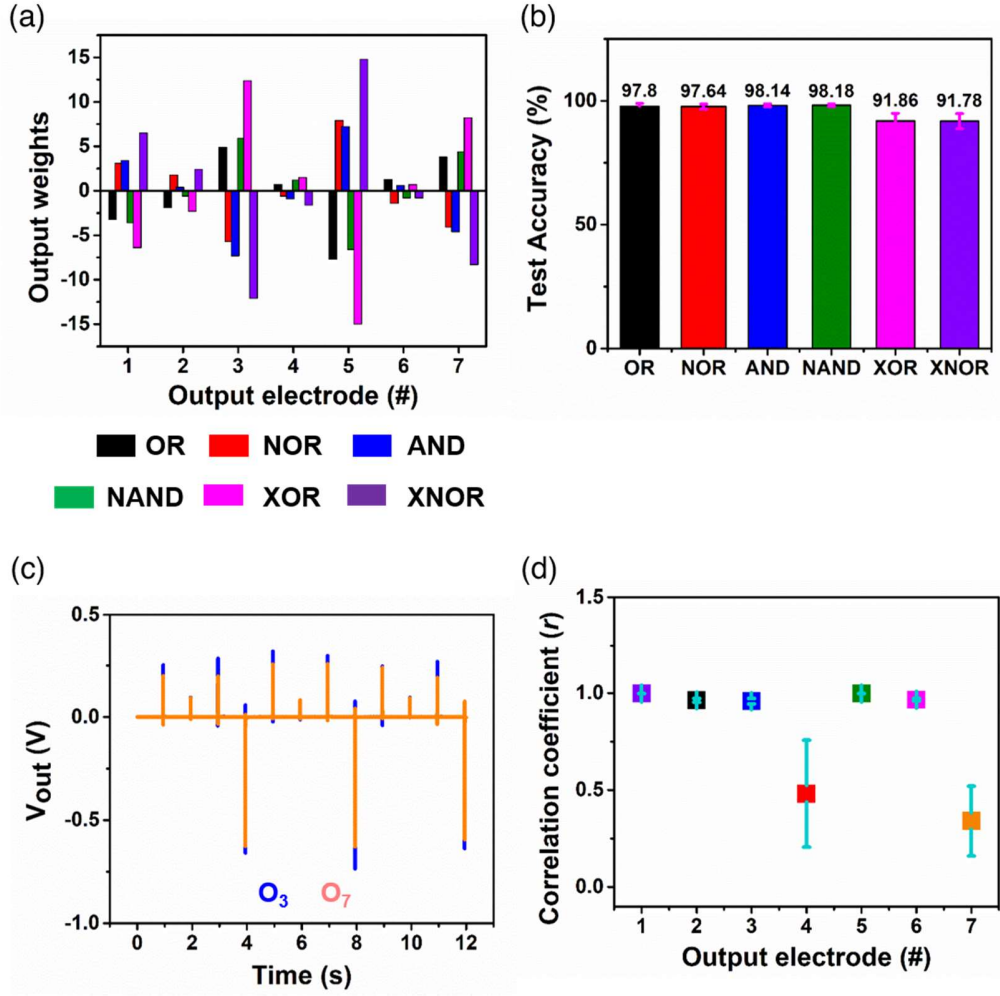


**Fig. 5.4** SWNT/Por-POM's reservoir performance analysis. (a) The plot of weight distribution against electrode pad number clearly shows distinct values for each electrode for all hence depicting the multitasking nature of the RC learning architecture. The learning is solely at the output layer and target specific, so no interference is there hence the gates are easily distinguishable. (b) The device performance analysis over five datasets. The plot shows the average test accuracy with the error bars (pink) representing the standard deviation amongst the datasets. (c) The  $V_{out}$  response from electrode pads O3 and O7. A zero response shows that no high dimensional spatial data in terms of amplitude is obtained which hinders the performance of complex XOR and XNOR. (d) The plot of  $V_{out}$  correlation coefficient ( $r$ ) for the same output electrode pads amongst different datasets. It gives a picture of the echo state property possessed by SWNT/Por-POM where a higher  $r$  implies that the reservoir state responses are same and is a function of the only input itself.

One of the pre requisites of RC is the presence of high dimensional outputs<sup>30)</sup> and in regard to in-materio SWNT/Por-POM, the random distribution of Por-POM over an array of recurrent SWNT network structure is a reflection of the cellular automata model.<sup>21)</sup> So like brain, network wide voltage readout dynamics of varying amplitudes, arising from Por-POM's redox nature, can be exploited as high dimensional spatial features when collected from different electrode points. As depicted in Fig. 5.2c noticeable amplitude changes corresponding to different binary input states (Fig. 5.2b) are visible for most electrodes except for O<sub>3</sub> and O<sub>7</sub> where an almost zero response for all input state combination can be visualized in Fig. 5.4c. Such result hinders in the overall weighted linear average (Eq. (2)) giving away a near zero additive factor even when the weight coefficients are non-zero elements (Fig. 5.4a), thereby reducing the high dimensional aspect and hence lags the performance magnitude of XOR /XNOR slightly than OR, AND, NOR and NAND gates. In machine intelligence the consistency of device performance is also important for it to be robust. The lower SD of around 0.75 for OR, AND, NOR and NAND and of about 3.0 for XOR and XNOR over all five test datasets in Fig. 5.4b emphasizes this point. The reproducible performance can be accredited to the high correlation between the V<sub>out</sub> of each electrode for all five datasets measured by the correlation coefficient ( $r$ ) parameter given in Eq. (5.5).

$$r = \frac{\sum_j (V_{out,i}^j - \overline{V_{out,i}}) (V_{out,i}'^j - \overline{V_{out,i}'})}{\sqrt{\sum_j (V_{out,i}^j - \overline{V_{out,i}})^2 (V_{out,i}'^j - \overline{V_{out,i}'})^2}} \quad (5.5)$$

The  $r$  is a measure of the closeness between V<sub>out, i</sub> and V'<sub>out, i</sub> of the same electrode  $i$  but different dataset. A value closer to one strengthens the input-output reproducibility focusing on the reservoirs another important conditional parameter of echo state property.<sup>30),33)</sup> Reservoir states (V<sub>out</sub> in this case) are mostly echoes of the input signal over time, as such, for the same input sequence irrespective of the given initial condition of the device, it should respond in a similar

manner for the learning operation to be valid for any given test dataset. The plot of  $r$  vs the output electrode number in Fig. 5.4d shows a near to 1 correlation for most electrodes with a small SD (error bars) amongst the datasets except for  $O_3$  and  $O_7$  where the  $r$  reduces due their unresponsive amplitude values. The observation clearly supports the fact that the SWNT/Por-POM device also features the echo state property over most reservoir states, as a result aids in for such in-tuned test performance by training  $W_{out}$  for only one time. An advantage of RC also lies in its ability to recall temporal information owing to the presence of recurrent network connection. It allows the reservoir to reconstruct a future time-step target sequence based on its past temporal sequence with the initial optimized trained weights. Figure 5.5a shows a concept for the non-linear XOR where the initial target sequence (top) was shifted by an infinitesimal amount of 0.01 s (middle) to a larger value of 1 s (bottom). Voltage readouts of test dataset containing same time-interval as the target set were then chosen to analyze the device performance over the initial trained weights. As seen from Fig. 5.5b, for multiple time shifts of the target in log scale, the SWNT/Por-POM reservoir was able to follow the target with a consistent accuracy relative to the no shift case, thereby supporting the fact that the random network of SWNT/Por-POM reservoir indeed possesses the recurrent connection as well. Furthermore the variation in accuracy over different training time-lengths were also conducted as shown in Fig. 5.5e (OR, AND, and XOR) and Fig. 5.5f (NOR, NAND, and XNOR) for one test dataset. The overall performance increases till 36 s epochs after which it becomes consistent till 60 s. The increase with time-length is justifiable, as it includes in a large number of data points  $N$  which makes the MSE in Eq. (3) attain a lower value. Usually, with increasing sampling space ( $N$  in this case), statistical precision tends to increase because of the presence of higher information leading to overall parameter estimation.

It also points out that the non-linear high dimensional information processing is retained over the entire time-series thereby producing recurrent mappings of the input assisting in such robust RC performance for any time length.

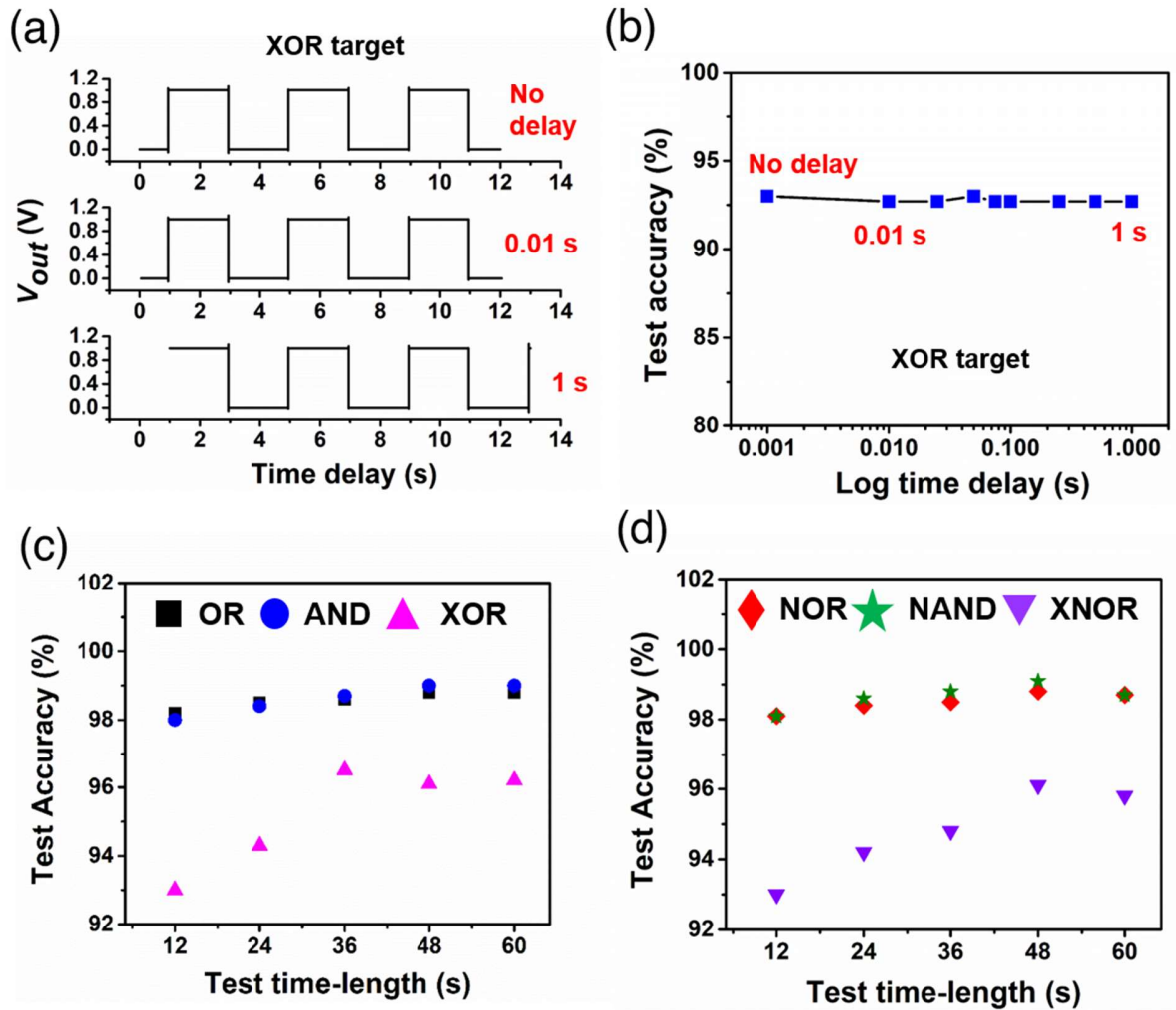


**Fig. 5.5** Temporal performance of SWNT/Por-POM. (a) The XOR target shifted by a certain time delay. The top shows the target with no delay, the middle one is with a small delay of 0.01 s and the bottom shows the maximum delay of 1 s. (b) The plot of test accuracy over logarithmic time delay scale. Each of the delayed targets were fitted with the same optimized trained weights obtained from the no delay target sequence. (c) Device performance robustness over different training time-lengths for OR, AND, and XOR. The graph shows the evaluation of one test dataset. An increase in accuracy is due to the increase in sampling points. (d) Similar interpretation as in (c) for NOR, NAND and XNOR gates.



A rudimentary property for any reservoir to carry out complex mathematical transformations of XOR or XNOR lies in its ability to process information non-linearly. In this context non-monotonic increase in current possessing the property of negative differential resistance (NDR) effect, where the current decreases with increasing bias, has emerged as an important parameter to estimate the machine intelligence index (*MII*) given by Eq. (5.6).<sup>24)</sup>

$$MII = 1 - \left( \frac{m(G_p) - m(G_n)}{m(G_p) + m(G_n)} \right)^2 \quad (5.6)$$

The MII approaches the value 1 only when the number  $m$  of positive ( $G_p$ ) and negative ( $G_n$ ) conductance's are equal, as this results in a NDR effect, thereby giving rise to higher degrees of non-linear response. To validate this, we studied the current response ( $I_{out}$ ) over voltage sweeps ( $V_{in}$ ) between -2 V to +2 V as seen in Fig. 5.6a. Varied degrees of non-linear responses from different electrodes are evident with small peaks of NDR. The MII was calculated from the differential current plot that gave the conductance values, as shown in Fig. 5.6b for the electrode pad O<sub>6</sub>. As our high logic state input bias was +2 V, we considered only the positive sweeping part of the I-V graph in Fig. 5.6a. Clear presence of multiple NDR peaks are visible in the range of 1 V to 2 V. NDR in SWNT/polyoxometalates is a well-known trait arising from the polyoxometalate redox states of multiple charge-discharge phenomena at the SWNT junctions.<sup>21)</sup> To compute the MII we calculated  $m(G_p)$  constituting the increasing conductance points with voltage in the direction of A to B (red dotted arrow) in Fig. 5.6b, and  $m(G_n)$  as the points from B to C (purple dotted arrow) of decreasing conductance with bias. The points corresponding to all the NDR peaks were calculated this way and the corresponding MII values were plotted against different electrode pads displayed in Fig. 5.6c. For all the electrodes a non-zero MII was obtained indicating the presence of non-linearity at every nodal points. The high positive MII as a consequence of NDR

makes the SWNT/Por-POM device act as a mathematical unit capable of performing both additive and subtractive operations in a single network structure. Since Boolean logic is an algebraic operation and gates like XOR, NOR, NAND and XNOR all require additive and inverted operators to be efficiently emulated, we believe that the inherent NDR effect along with high dimensional spatial readouts make SWNT/Por-POM a promising candidate for fruitful exhibition of in-material RC based Boolean function optimization.

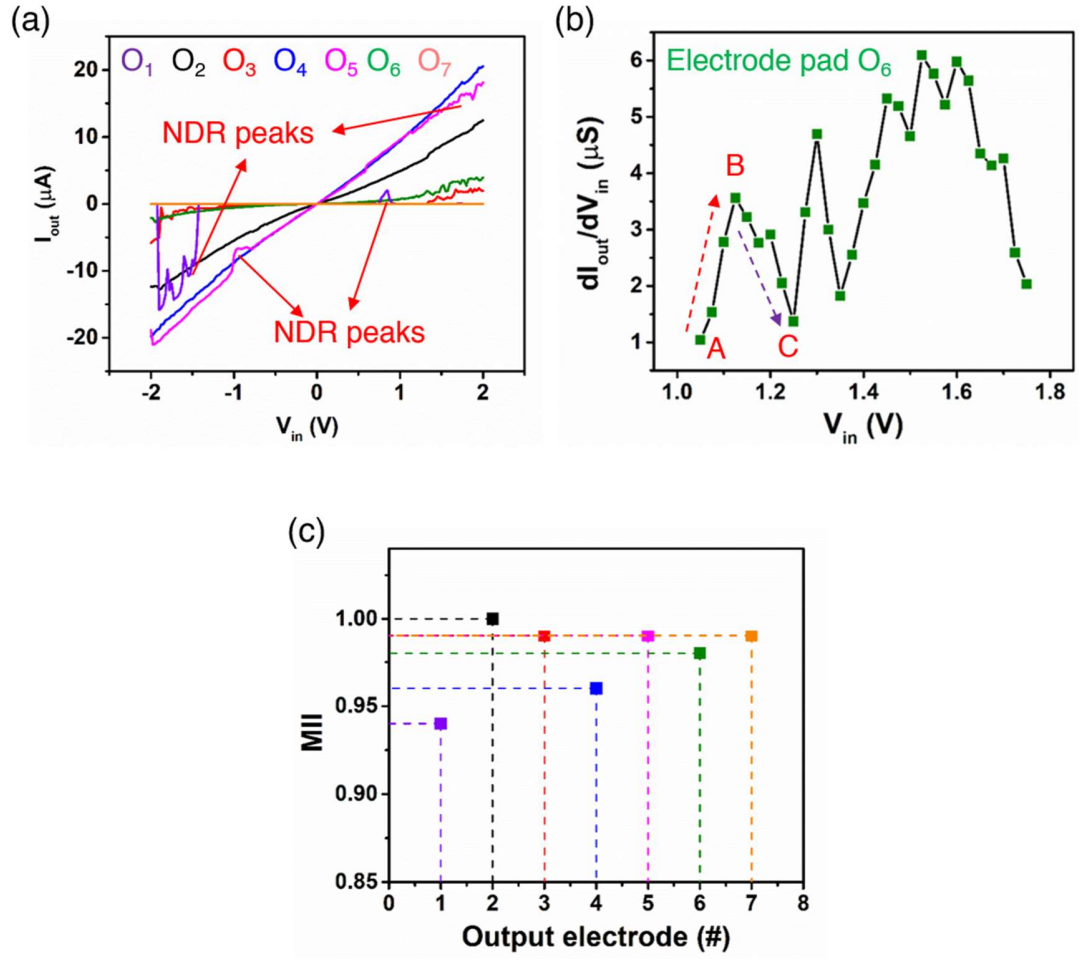


**Fig. 5.6** The importance of non-linear negative differential resistance (NDR) towards RC task. (a)  $I_{out}$  vs.  $V_{in}$  plots of all electrodes color coded with the schematic in Fig. 5.2(a). Since the magnitudes of  $I_{out}$  differ with electrodes so Small NDR peaks are visible in the plot. (b) The  $dI_{out}/dV_{in}$  plot of only the positive I-V sweep for output electrode  $O_6$  which gives the value of device conductance ( $G$ ). The graph is smoothed with Savitzky-Golay method to get the clearer NDR peaks. A positive  $G_p$  are the points in the direction A to B while the points of negative  $G_n$  are from B to C. (c) The measured machine intelligence index (MII) for different electrode pads. The MII is calculated using Eq. (6) where the points of  $G_p$  and  $G_n$  are counted from plot from (b) for all the peaks.

## 5.4 Conclusion

In summary, we successfully demonstrated SWNT/Por-POM in-materio RC task of Boolean logic optimization at room temperature using off-line supervised learning. The linearly combined readouts very well followed the targets of all six logic operations of OR, AND, NOR, NAND, XOR and XNOR with an accuracy of greater than 90%. The device showed robust performance over all five datasets and entire time-length sequence of the input due to the possession of echo-state property and lossless information processing driven by the binary inputs. Non-linearity in the form of NDR behavior was also observed as suggested from the non-zero MII index. Presence of such non-linearity and high dimensional outputs from multiple electrodes is sought to be the reason for such high accuracy performance. The unique weights for each task allows for the logic gates to be classified, hence can be constructed without any interference. The performance of XOR and XNOR lagged behind others gates as these are complex operations, but training over large datasets and with more output linear combinations can be considered important factors for their performance enhancement. We believe that such first-hand exhibition of in-materio RC specifically with SWNT/Por-POM dynamical system can open up possibilities for other temporal and non-temporal RC tasks in near future.

## References

- 1) P. A. Jansson, Anal. Chem. **63** [6], 357 (1991).
- 2) O. I. Abiodun, A. Jantan, A. E. Omolara, K. V. Dada, A. M. Umar, O. U. Linus, H. Arshad, A. A. Kazaure, U. Gana and M. U. Kiru, IEEE Access **7** [February 2017], 158820 (2019).
- 3) M. Lundstrom, Science (80-. ). **299** [5604], 210 (2003).
- 4) G. Yeric, .
- 5) K. J. Kuhn, Proc. - 2009 13th Int. Work. Comput. Electron. IWCE 2009 1 (2009).
- 6) D. Efnusheva, A. Cholakoska and A. Tentov, Int. J. Comput. Sci. Inf. Technol. **9** [2], 151 (2017).
- 7) M. Ziegler, Sci. Rep. **10** [1], 10 (2020).
- 8) Z. Wang, R. Midya, S. Joshi, H. Jiang, C. Li, P. Lin, W. Song, M. Rao, Y. Li, M. Barnell, Q. Wu, Q. Xia and J. J. Yang, Proc. - IEEE Int. Symp. Circuits Syst. **2018-May**, 2 (2018).
- 9) D. Vodenicarevic, N. Locatelli, A. Mizrahi, J. S. Friedman, A. F. Vincent, M. Romera, A. Fukushima, K. Yakushiji, H. Kubota, S. Yuasa, S. Tiwari, J. Grollier and D. Querlioz, Phys. Rev. Appl. **8** [5], 1 (2017).
- 10) M. Lukosevicius, H. Jaeger and B. Schrauwen, Kunstl Intell **26**, 365 (2012).
- 11) B. Schrauwen, D. Verstraeten and J. Van Campenhout, in *ESANN 2007 Proceedings - 15th European Symposium on Artificial Neural Networks* (2007) pp. 471.
- 12) Z. Konkoli, *On Reservoir Computing: From Mathematical Foundations to Unconventional Applications* (2017).
- 13) B. Li, E. Zhou, B. Huang, J. Duan, Y. Wang, N. Xu, J. Zhang and H. Yang, Proc. Int. Jt. Conf. Neural Networks 4062 (2014).
- 14) Z. R. Wang, Y. Li, Y. T. Su, Y. X. Zhou, L. Cheng, T. C. Chang, K. H. Xue, S. M. Sze and X. S. Miao, IEEE Trans. Electron Devices **65** [10], 4659 (2018).

- 15) A. Adamatzky, B. De Lacy Costello, P. Dittrich, J. Gorecki and K. P. Zauner, *Int. J. Gen. Syst.* **43** [7], 757 (2014).
- 16) J. W. Lawson and D. H. Wolpert, *J. Comput. Theor. Nanosci.* **3** [2], 272 (2006).
- 17) J. M. Tour, W. L. Van Zandt, C. P. Husband, S. M. Husband, L. S. Wilson, P. D. Franzon and D. P. Nackashi, *IEEE Trans. Nanotechnol.* **1** [2], 100 (2002).
- 18) K. Scharnhorst, W. Woods, C. Teuscher, A. Stieg and J. Gimzewski, *Proc. IEEE/ACM Int. Symp. Nanoscale Archit. NANOARCH 2017* 133 (2017).
- 19) S. K. Bose, C. P. Lawrence, Z. Liu, K. S. Makarenko, R. M. J. Van Damme, H. J. Broersma and W. G. Van Der Wiel, *Nat. Nanotechnol.* **10** [12], 1048 (2015).
- 20) M. K. Massey, A. Kotsialos, F. Qaiser, D. A. Zeze, C. Pearson, D. Volpati, L. Bowen and M. C. Petty, *J. Appl. Phys.* **117** [13], 134903 (2015).
- 21) H. Tanaka, M. Akai-Kasaya, A. Termehyousefi, L. Hong, L. Fu, H. Tamukoh, D. Tanaka, T. Asai and T. Ogawa, *Nat. Commun.* **9** [1], 1 (2018).
- 22) Y. Yamazaki, K. Yamashita, Y. Tani, T. Aoyama and T. Ogawa, *J. Mater. Chem. C* **8** [41], 14423 (2020).
- 23) Z. Shi, Y. Zhou, L. Zhang, C. Mu, H. Ren, D. U. Hassan, D. Yang and H. M. Asif, *RSC Adv.* **4** [91], 50277 (2014).
- 24) T. Chen, P. A. Bobbert and W. G. Wiel, *Small Sci.* **1** [3], 2000014 (2021).
- 25) W. W. Aji, Y. Usami, Hadiyawarman, R. Oyabu and H. Tanaka, *Appl. Phys. Express* [ DOI:10.35848/1882-0786/abb68d].
- 26) J. Hu, Y. Ji, W. Chen, C. Streb and Y. F. Song, *Energy Environ. Sci.* **9** [3], 1095 (2016).
- 27) G. Tanaka, T. Yamane, J. B. Héroux, R. Nakane, N. Kanazawa, S. Takeda, H. Numata, D. Nakano and A. Hirose, *Neural Networks* **115**, 100 (2019).
- 28) M. Lukoševičius and H. Jaeger, *Comput. Sci. Rev.* **3** [3], 127 (2009).
- 29) D. Verstraeten, B. Schrauwen, M. D'Haene and D. Stroobandt, *Neural Networks* **20** [3], 391 (2007).

- 30) K. Nakajima, arXiv.
- 31) M. McCloskey and N. J. Cohen, Psychol. Learn. Motiv. - Adv. Res. Theory **24** [C], 109 (1989).
- 32) T. Chen, J. van Gelder, B. van de Ven, S. V. Amitonov, B. de Wilde, H. C. Ruiz Euler, H. Broersma, P. A. Bobbert, F. A. Zwanenburg and W. G. van der Wiel, Nature **577** [7790], 341 (2020).
- 33) H. Jaeger, GMD Rep. [148], 1 (2010).

## Chapter 6

### **Binary object classification with tactile sensory input information of via single-walled carbon nanotube/porphyrin-polyoxometalate network as in-materio reservoir computing**

**Abstract:** Information encoding by human brain through sensory touch is highly pronounced as a characteristic trait of object distinguishability. Tactile sensors in robot serve this purpose of fetching object grasping information, but to utilize it for classifying the object based on a certain feature, a neural network architecture is mandatory for learning the processed data over repeated trainings. Herein, we use single-walled carbon nanotube/porphyrin-polyoxometalate (SWNT/Por-POM) in-materio reservoir architecture to classify objects of differing hardness by supervised learning of the fetched tactile grasping data implemented on a Toyota Human Support Robot (HSR) manipulator. The classification problem is addressed using binary one-hot vector target where the device learns to output a high value target as the correctly labelled object relative to the other objects labelled as the low vector target. We show that this kind of classification primes up when the grasping information data follows a  $1/f$  power law of maximized information processing.



## 6.1 Introduction

Fast processing capabilities of electronic components along with their miniaturization have made today's robots smarter, smaller and efficient compared to what they were specifically designed for as heavy object lifters. The visible changes have redefined the coming age of robotic technology to scale-up their utility in healthcare, military, agriculture, and automobile industries via the development of sensors and machine learning technologies.<sup>1-6</sup> The evolution in terms of structure, functionality, flexibility, and human level interaction has recently encouraged Toyota to manufacture a Human Support Robot (HSR) mobile manipulator to be implemented as a human-like domestic robot aimed at cleaning and fetching/carrying objects, thereby reducing physical efforts for all age groups of people, especially the aged and disabled ones.<sup>7</sup> To implement such a 'pick-place' operation, the HSR must recognize the objects of interest and classify them just like humans do. A usual way for this is to use a visual camera sensor to process object images based on their geometry and learn them over time through ANN architectures.<sup>8,9</sup> Although such training allows instant detection without reference object templates every time, the sensors falter to gather valuable information at low light environments, hence leading to faulty operations. So, to avoid this, deep learning techniques interfaced with tactile sensors<sup>10-12</sup> have been employed to categorize object grasping data into different classes based on hardness under any environment through overtime training and learning. Recently *Tamuko et al.* has designed a flexible tactile sensor supported on the Toyota HSR arm and used the grasping information to classify objects of different hardness and color by employing an echo state network architecture theoretically.<sup>13</sup> Since RC follows an echo state approach of weight training and learning we hereby illustrate the in-materio RC of binary object classification by taking advantage of the non-linear information processing emerging from the random network of SWNT/Por-POM. The problem statement consists of two

parts, (i) the collection of raw tactile sensory data and converting to the desirable voltage inputs and (ii) use a one-hot vector supervised target as object labels for training the voltage readouts from SWNT/Por-POM hence formulating the classification task. One-hot encoding is employed to convert categorical data into numerical values as this makes it easier for the neural network algorithm to distinguish the patterns in the form of numerical matrices. In binary one-hot, the classification is gauged between two objects as shown in Fig. 6.1. The target vector can be designed row or column wise and contains vector values of only '1' and zero. The supervised target for the correctly predicted object will be row/column matrix with '1' and '0' valued where the position of '1' will be labelled under the categorical variable to be correctly classified while the other being labelled '0' indicating the 'not correct object prediction'.

## 6.2 Methods

### 6.2.1 SWNT/Por-POM dispersion

The SWNT/Por-POM dispersion was obtained using a known procedure.<sup>14</sup> Initially,  $2 \times 10^{-2}$  gL<sup>-1</sup> HiPCo SWNT, purified according to the previous report,<sup>15</sup> and  $4 \times 10^{-2}$  gL<sup>-1</sup> of Por-POM were first bath sonicated in ethanol for 1 h (40 k Hz) separately and then for 4 h by mixing them together. The dispersion was then centrifuged at 1,000 G for 15 min and the excess of supernatant was discarded. The precipitate was collected and was further bath sonicated in ethanol for 1 h to get the final dispersion.

### 6.2.2 Fabrication of MEA substrate

Aluminum coated MEA pattern was obtained via a standard photolithography process on a borosilicate glass substrate. A lift-off resist LOR-10A was first spin coated at 3,000 rpm for 50 s followed by the deposition of the photoresist S18186 spin-coated at 4,000 rpm for 2 s. The substrate was pre-baked at 90 °C for 5 min and the pattern was developed with a 25 s exposure to

the UV light. Finally, the resist was developed using MF 319 developer for 90 s and 50 nm thick aluminum metal was sputtered that produced the desire MEA substrate with inner circular pad diameter of 500  $\mu\text{m}$  and a pitch of 1.5 mm.

### *5.2.3 Thin film deposition of SWNT/Por-POM computational material*

Thin film of SWNT/Por-POM random network was deposited onto the MEA pattern as per the previous report.<sup>16,17</sup> A vacuum-assisted wet transfer process was applied where 500  $\mu\text{L}$  of SWNT/Por-POM was filtered through a 1  $\mu\text{m}$  nitrocellulose paper and was placed on top of the MEA substrate with the SWNT/Por-POM facing down followed by its dissolution in acetone.

The entire substrate with the thin film was dried using acetone vapors at 80  $^{\circ}\text{C}$  by placing it on a glass veil of acetone solution.

### *5.2.4 Tactile sensory information and conversion to time-series data*

Here we give the details about the tactile sensory data along with converting the raw sensory dataset obtained into time series data. Grasping data is the robot hand's angle ( $\theta$ ) when it grasps the object with constant torque. We measure the robot hand's angle ( $\theta$ ) grasping the object every 0.1N between 0.1N and 1.2N. A total of five grasping datasets were obtained for each of the objects and the same pre-processing method was applied. For the pre-processing, the corresponding ' $\theta$ ' values obtained from the objects' grasping datasets were arranged into 5 bits/s information and were normalized to lie in the interval of  $[0, -1]$  V. An input gain of '5' was multiplied throughout the range to give the desired input signal in the interval of  $[0, -5]$ . To carry out the RC task of object classification the custom built setup as described in *Chapter 5 section 5.8.2* was used. The input interval stream was generated using the LabVIEW program and was fed to the device via an electrical probe interfaced with a multifunctional I/O DAQ system (NI PXIe-4141) instead of a

function generator. The outputs were collected via another probe and was readout by the PC using a high speed USB carrier (NI USB-9162) sampled at 1 kHz. The weight optimization of Boolean logic RC task was all performed using a one-hot encoded program designed in Python off-line via a ridge regression model. All measurements were done at room temperature (28 °C) and pressure. The detailed methods with corresponding schematic are discussed in *Chapter 2*.

The logarithmic plots of PSD were fitted using the power law in Eq. (6.1) where A represents the proportionality constant and  $\gamma$  represents the scaling factor. Both the FFT and the fitting was done using Origin Pro 9 software.

$$PSD = \frac{A}{f^\gamma} \quad (6.1)$$

The short term Fourier transform (STFT) was also performed in Origin Pro 9 software operation with a Hamming window length of 256 points spaced over the time-interval and an overlapping window of 128 points.

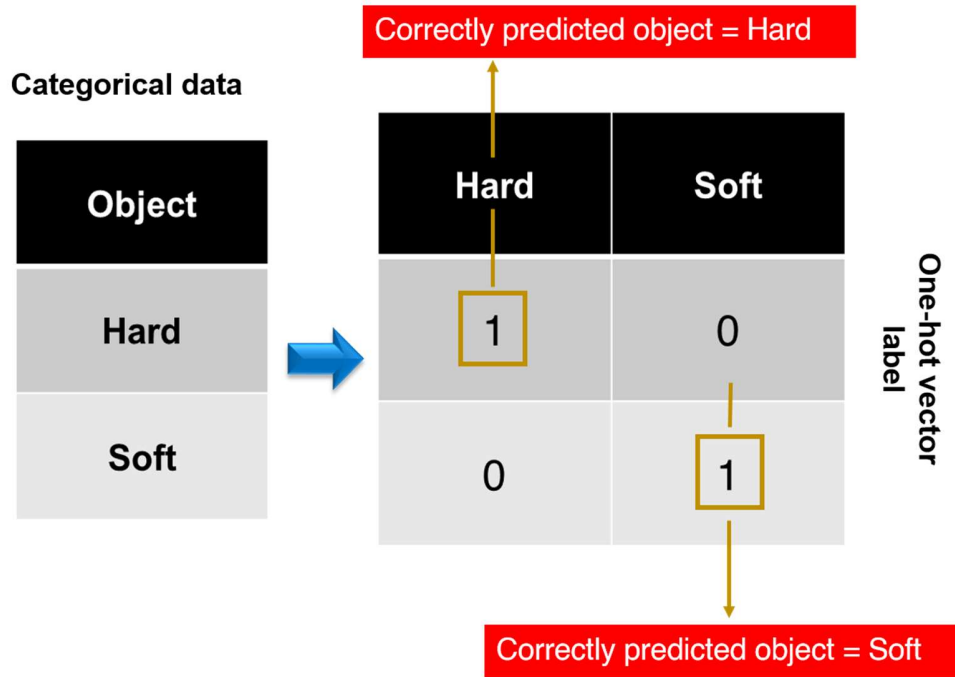


**Fig. 6.1** Illustration showing the one-hot vector operation for binary classification. Categorical data labelled as 'Hard and 'Soft' are changed to one-hot vector labels of '1' and '0'. The target is a row/column binary data consisting of both the values. For the 'Hard' object the matrix representation of the target positions '1' in the first column and '0' in the second like [1 0] and for the 'Soft' it is the opposite like [0 1]. Training is done corresponding to those matrix sets.

### 6.3 Results and Discussion

Figure 6.2a left shows the HSR, with an elaborated schematic of its arm on the right attached to the gripper via a force-torque sensor that generates tactile sensory information of grasped objects containing the change in the gripper angle ( $\theta$ ) as a function of the applied forces (see Methods). Four toys of mixed hard and soft, namely bus, block, dog, and hedgehog (HH hereafter), were used in this study as depicted from top to bottom in the red box beside the schematic of Fig. 6.2a. The tactile sensing data from each of the grasped objects was collected and pre-processed using LabVIEW software to obtain bits of input biases of varying voltages sequenced over time as shown in Fig. 6.2b right (see Methods). Five input datasets corresponding to each object were produced

by grasping the objects and were arranged sequentially in the LabVIEW which were fed to one electrode of the MEA and outputs from 11 electrode pads related to each of the inputs were recorded one at a time shown in Fig. 6.2c. The data collection was separately done as in only after finishing the input-output operation for one object for all 11 electrodes, the procedure for the next object was done and continued till data of all four objects became available. The pre-processing produces bits of DC like input biases of different voltages as seen in Fig. 6.2b right that are used to perturb the SWNT/Por-POM reservoir to fetch high dimensional spatio-temporal voltage information particular to a given object. These outputs acted as the different internal states of the SWNT/Por-POM reservoir represented as  $X_{class}$ . 80% of the datasets were used for training and the remaining 20% were used for testing the device's classification performance as displayed in Fig. 6.2d. For training, the output weights  $W_{out}^{class}$  were optimized with the one-hot vector supervised target  $Y_{one-hot}$ , having data length equal to the time length of the input data, using an offline ridge regression<sup>18</sup> shown in Eq. (6.2). The targets for each of the objects are shown in Fig. 6.2d where the correctly classified object were labelled the vector value '1', while the others were labelled '0'.

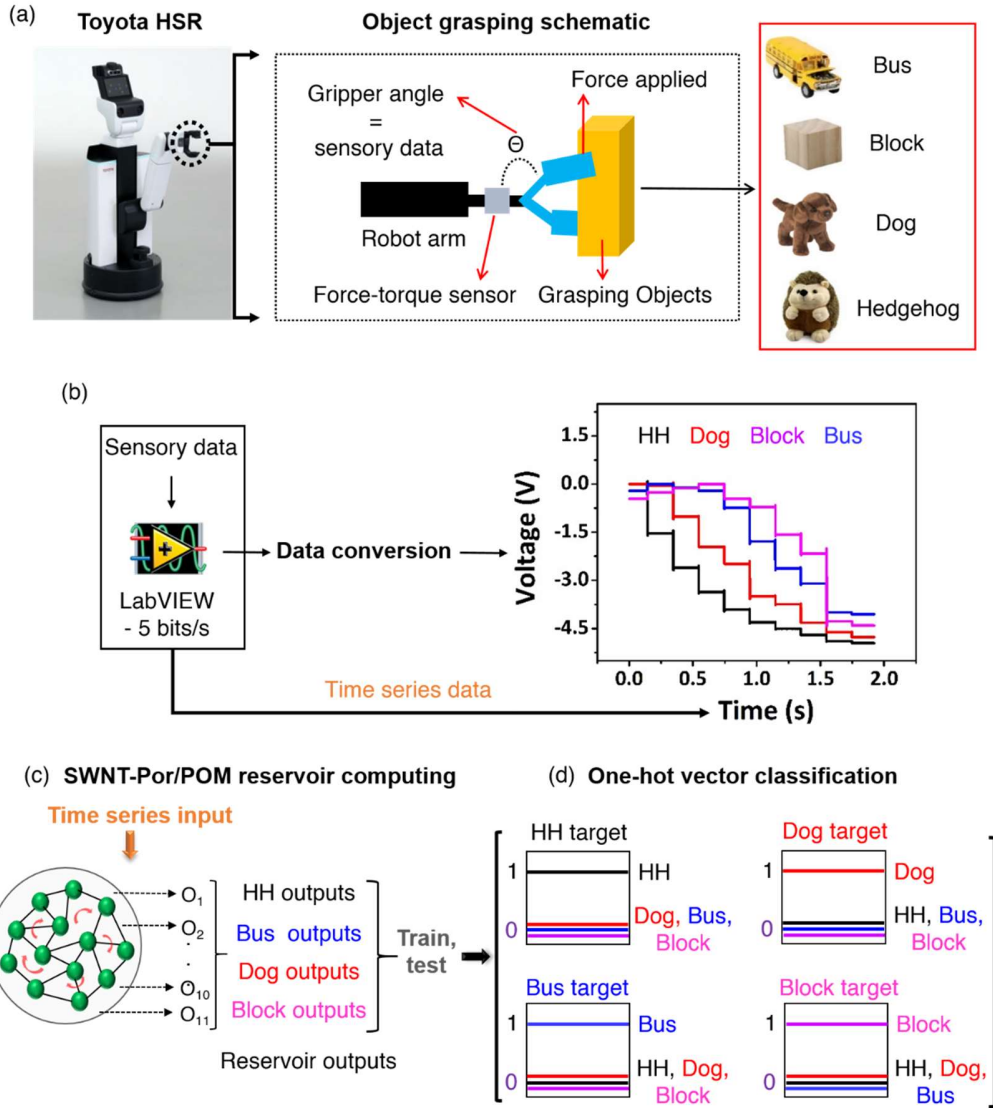


**Fig. 6.2** Stepwise object binary classification with SWNT/Por-POM reservoir. (a) The HSR (left) with a schematic of the arm (middle) connected to the gripper via force-torque sensor gathers tactile data from the change in the gripper angle ( $\theta$ ) and grasping force applied to objects (right) like bus, block, dog, and hedgehog (HH) toys presented in a red box. (b) The sensory data obtained from each of the objects in are converted to voltage-time using LabVIEW by sampling at 5 bits/s (left) in the range [0, -5] V as depicted graphically to the right. (c) Time series inputs are separately inputted into the SWNT (black line)/Por-POM (green circles) reservoir with recurrent connections (red arrow). A total of 11 reservoir outputs, each of HH, Dog, Block, and Bus, are collected one by one over the entire input time frame, and 80% of them were trained, with the remaining 20% being tested for binary classification evaluation. d) One-hot vector encoding is used for binary classification. Each square box with the lines inside represents the supervised target signal for each of HH, dog, bus and block where the true predicted object is trained to vector value 1 while the others are trained to vector value 0.

The ridge regression model was chosen because this kind of regularization is beneficial for fitting models where the independent variables are highly correlated. Since the target length over entire time series is either ‘0’ or ‘1’ so the value at each time step is the same and highly correlated. The model was encoded in Python with a ridge regularization co-efficient ( $\lambda$ ) value of one multiplied to an identity matrix  $I$ . To test the SWNT/Por-POM reservoirs classification performance an inference was made on a test dataset consisting of the reservoir states of  $S_{class}^i(t)$  collected from its related test input time series sequence. The supervised target was fitted by constructing the reservoir output  $Z(t)$  using a weighted linear combination of the optimized weights (Eq. (6.2)) by Eq. (6.3).

$$W_{out-class} = (X_{class}^T X_{class} + \lambda I) X_{class}^T Y_{one-hot} \quad (6.2)$$

$$Z(t) = \sum_{i=1}^{11} W_{out-class}^i S_{class}^i(t) \quad (6.3)$$

Figure 6.3 shows the inference data of binary object classification for each of the objects compiled into one plot. Each of HH (Fig. 6.3a), Dog (Fig. 6.3b), Block (Fig. 6.3c), and Bus (Fig. 6.3a) were rightly predicted in presence of another object giving a likelihood of vector target value ‘1’.



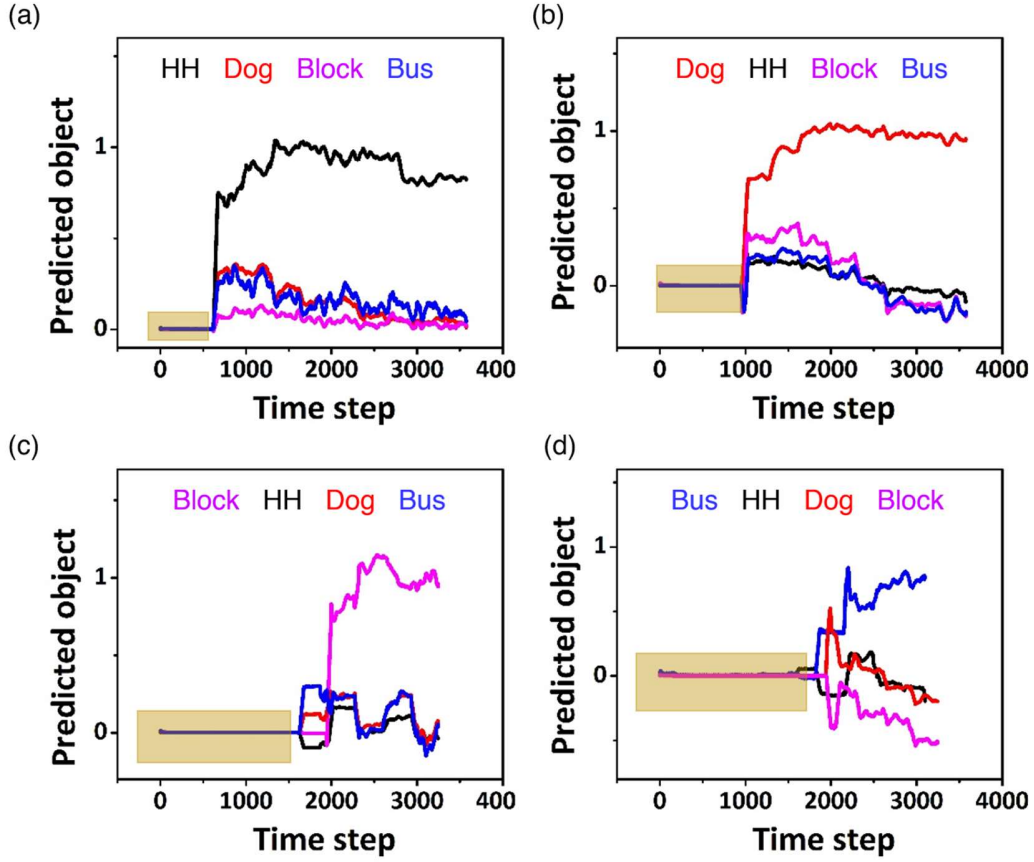


**Fig. 6.3** RC task of supervised one-hot vector target binary object classification result on test data with SWNT/Por-POM reservoir. True predicted classification of (a) HH, (b) Dog, (c) Block, and (d) Bus with their respective color codes. The binary classification task for each pair of objects was performed separately and the results are concatenated into one plot for each of the objects. Initially a no separation region marked by the colored rectangular box is seen which eventually resulted in a successful classification where the true predicted object showed a likelihood of vector value ‘1’ with others being ‘0’.

It is to be noted that in each of the cases the classification happens after a certain time-step before which it remains unclassified as marked by the colored rectangular box. This can be understood by the extent of information processing arising from the output responses presented in Fig. 6.4a. As discussed in *Chapter 3*, that for a reservoir to compute it is very much necessary that it operates at the ‘edge of chaos regime’. For any dynamical non-linear physical system such phenomena emerges as the  $1/f'$  maximization of information processing like the human brain.<sup>19–23</sup> SWNT/Por-

POM too shows a similar behavior in this context as evident from the logarithmic PSD plot of the temporal DC current dynamics (*Chapter 3*, Fig.). Here also, as we can see from Fig. 6.4a that Compared to ‘Region A’, the non-linear NDR like high dimensional fluctuations are more pronounced in ‘Region B’ which leads to a distinct increase in the scaling factor  $\gamma$  evident from the PSD plots of a certain time section in Fig. 6.4b-e. A contrasting change is observed between the two regions evident from the bar plot in Fig. 6.4f. Such characteristic behavior of both the regions are replicated over the entire time-step as also depicted in the plots of short-term Fourier transform (STFT) in Fig. 6.5. STFT basically gives a three-dimensional mapping of the PSD which shows the variation of the amplitude of frequency, represented by the color profile, as a function of time. Here also the graph is divided into two regions marked by double headed arrows above each plot of HH (Fig. 6.5a), dog (Fig. 6.5b), block (Fig. 6.5c) and bus (Fig. 6.5d). The orange arrow is the signature of ‘Region A’ in PSD plot where the amplitude gradient over all frequency and time range is almost constant and very low. On the other hand, the green arrow depicts the ‘Region B’ in the PSD plot which not only shows an increase in the frequency amplitude along the time scale but also shows a fall in the gradient at higher frequencies suggestive of the  $1/f$  scale-free behavior. Thus, as the transition from ‘Region A’ to ‘Region B’ takes place, more information exchange via the charge-discharge cascading effects happens which in turn enhances the object separability following their respective supervised targets. Thus the requirement of maximization of information to correctly optimize the weights via supervised learning to is highly evident from these observations in order to successfully achieve the binary classification task. It is noteworthy here that the performance of the in-materio RC device consisting of SWNT/Por-POM for classification, replicates the results of the previously algorithm-based echo state network (ESN) approach.<sup>13</sup> Thus, the present analysis substantiates the fact that, low-dimensional material

platforms with their non-linear information processing capability holds the potential of emulating their software analogues for machine intelligence task performance.

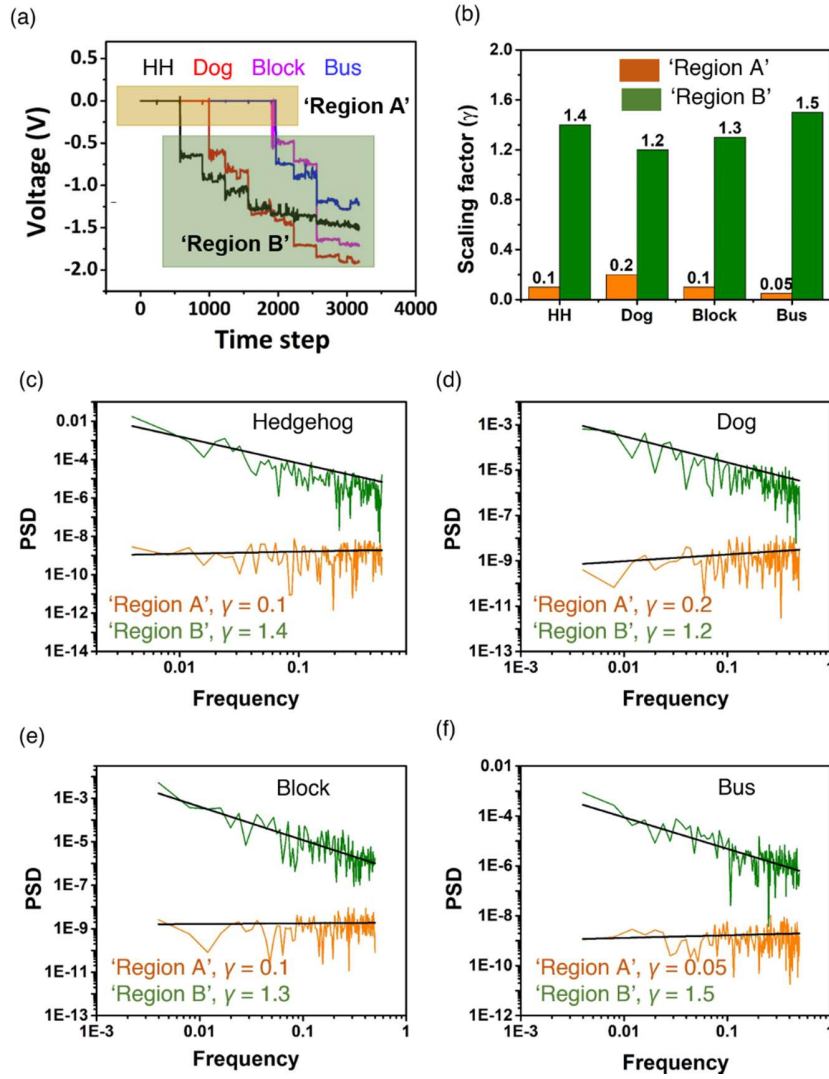


**Fig. 6.4** Object output responses and the power spectral density (PSD) (a) The output response obtained from averaging all 11 outputs of the micro-electrode array for HH, Dog, Block, and Bus. A flat response of 'Region A' in the yellow box was transformed to higher fluctuations, marked by green box 'Region B'. The PSD plots of (b) HH, (c) Dog, (d) Block and (e) Bus obtained via FFT of 300-550 time step of 'Region A' (yellow line) and 2600-2850 time step of 'Region B' (green line) from plot (a). Each logarithmic PSD plot is fitted with the power law equation to obtain the scaling factor  $\gamma$  displayed at the bottom. (f) Comparison of  $\gamma$  of 'Region A' (orange bar) and 'Region B' (green bar) obtained from PSD for HH, Dog, Block and Bus. A clear increase in  $\gamma$  from 'Region A' to 'Region B' is observed for all objects indicating maximum information processing, a symbol of  $1/f^\gamma$  scale-free operation.

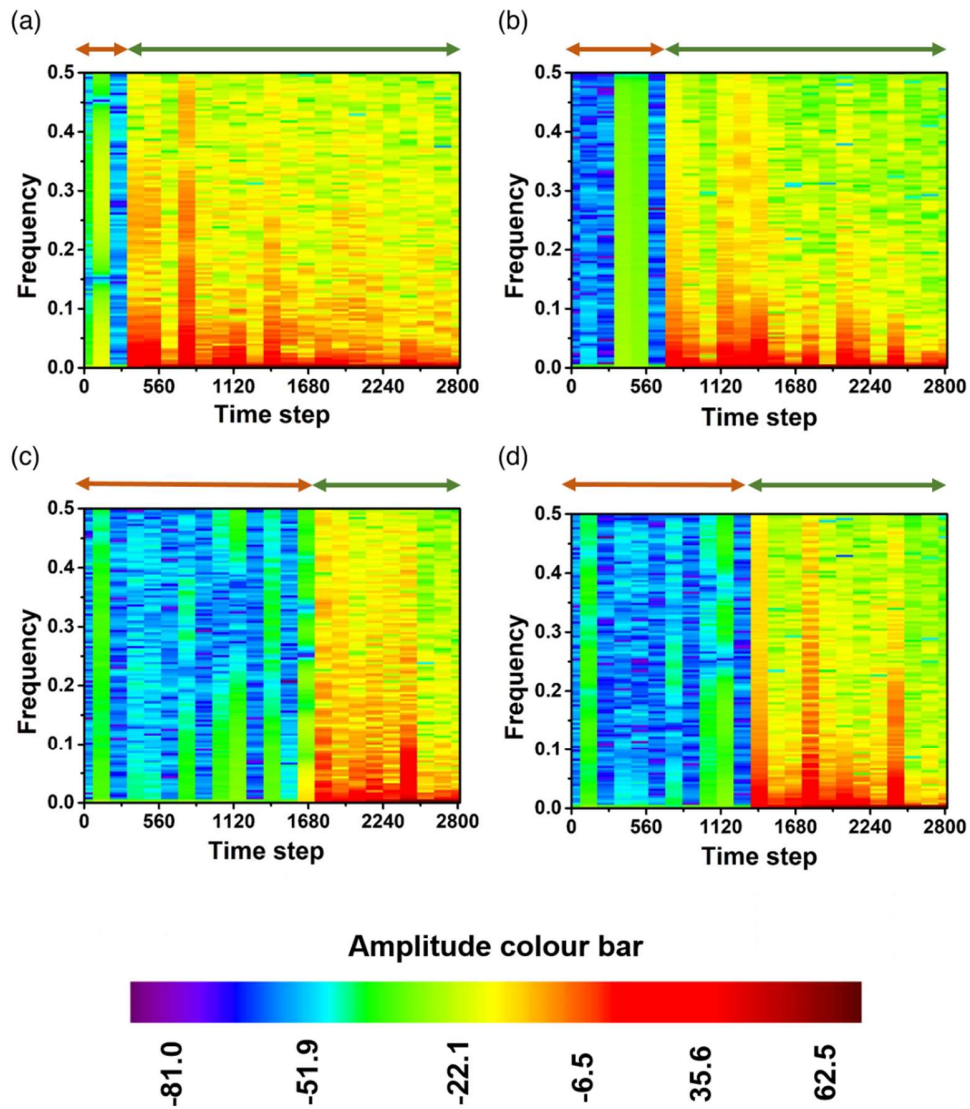


**Fig. 6.5** Short-term Fourier transform (STFT) of object output responses obtained over the time step of output response in Fig. 6.4 for (a) HH, (b) Dog, (c) Block, and (d) Bus with the amplitude colour bar at the bottom. The orange double headed arrow represents the 'Region A' of PSD plot (Fig. 6.4). The blue amplitude gradient shows minimal frequency change of low information. The green double headed arrow represents that of 'Region B' of PSD (Fig. 6.4). The higher amplitude gradient in the frequencies over time shows maximization of information. The decreasing change in gradient along the higher frequency in the y-axis is the indication of the  $1/f'$  scaling behavior coincidental with the PSD.

## 6.4 Conclusion

The paper showed the potential of SWNT/Por-POM as an in-materio reservoir for binary object classification task. Objects of soft like HH and dog, and hard like bus and block each of them can be categorized into their respective target vectors by following a simplified ridge regression training interfaced with Python software. The fruitful operation is a direct consequence of the materials high dimensional non-linear outputs arising from the charge transfer redox behavior of SWNT/Por-POM complex. Voltage readouts of NDR like fluctuations originating from a sub-threshold charge-discharge phenomena allows exchange of maximum information network wide evident from the  $1/f$  behavior of the logarithmic PSD plot. The performance replicates the ‘edge of chaos’ phenomena where the available information becomes desirable for such computational performance. All these result thus suggest that brain-like dynamics and information processing can be realized in our SWNT/Por-POM device with large scalability just from wet transfer thin film deposition. Simplified fabrication method along with easy learning architecture provides for the inclusion of another low dimensional material in the family of in-materio RC. A unified structure of processing and learning unit like brain can hence emerge as an alternative ‘in-materio neural network architecture’ for the present day von Neumann ones leading to a paradigm shift in field of straightforward unconventional computing.

## References

1. Siegel, M. Smart sensors and small robots. *Conf. Rec. - IEEE Instrum. Meas. Technol. Conf.* **1**, 303–308 (2001).
2. Favennec, J. M. Smart sensors in industry. *J. Phys. E.* **20**, 1087–1090 (1987).
3. Pinto, A. M. *et al.* Evaluation of depth sensors for robotic applications. *Proc. - 2015 IEEE Int. Conf. Auton. Robot Syst. Compet. ICARSC 2015* 139–143 (2015).  
doi:10.1109/ICARSC.2015.24
4. McSherry, T. M. Robots of the Future. *Proc. Annu. Meet. Tech. Conf. - Numer. Control Soc.* 39–48 (1984). doi:10.1007/s12045-007-0073-7
5. Andras, I. *et al.* Artificial intelligence and robotics: a combination that is changing the operating room. *World J. Urol.* **38**, 2359–2366 (2020).
6. Bogue, R. The role of artificial intelligence in robotics. *Ind. Rob.* **41**, 119–123 (2014).
7. Yamamoto, T. *et al.* Development of Human Support Robot as the research platform of a domestic mobile manipulator. *ROBOMECH J.* **6**, (2019).
8. Balasubramanian, S., Chukewad, Y. M., James, J. M., Barrows, G. L. & Fuller, S. B. An Insect-Sized Robot That Uses a Custom-Built Onboard Camera and a Neural Network to Classify and Respond to Visual Input. in *Proceedings of the IEEE RAS and EMBS International Conference on Biomedical Robotics and Biomechatronics 2018-Augus*, 1297–1302 (2018).
9. Giusti, A. *et al.* A Machine Learning Approach to Visual Perception of Forest Trails for Mobile Robots. *IEEE Robot. Autom. Lett.* **1**, 661–667 (2016).

10. Kumra, S. & Kanan, C. Robotic grasp detection using deep convolutional neural networks. in *IEEE International Conference on Intelligent Robots and Systems* **2017-Septe**, 769–776 (2017).
11. Qian, X. *et al.* Hardness recognition of robotic forearm based on semi-supervised generative adversarial networks. *Front. Neurorobot.* **13**, 1–10 (2019).
12. Yuan, W., Zhu, C., Owens, A., Srinivasan, M. A. & Adelson, E. H. Shape-independent hardness estimation using deep learning and a GelSight tactile sensor. in *Proceedings - IEEE International Conference on Robotics and Automation* 951–958 (2017).  
doi:10.1109/ICRA.2017.7989116
13. Shoshi, T., Yuichiro, T., Takumi, K., Koh, H. & Hakaru, T. Object Recognition Using Flexible Tactile Sensor. *Proc. Asia Pacific Conf. Robot IoT Syst. Dev. Platf.* **2020**, 81–82 (2021).
14. Hu, J., Ji, Y., Chen, W., Streb, C. & Song, Y. F. ‘Wiring’ Redox-Active Polyoxometalates To Carbon Nanotubes Using a Sonication-Driven Periodic Functionalization Strategy. *Energy Environ. Sci.* **9**, 1095–1101 (2016).
15. Aji, W. W., Usami, Y., Hadiyawarman, Oyabu, R. & Tanaka, H. Frequency dependence dielectrophoresis technique for bridging graphene nanoribbons. *Appl. Phys. Express* **13**, (2020).
16. Tanaka, H. *et al.* A molecular neuromorphic network device consisting of single-walled carbon nanotubes complexed with polyoxometalate. *Nat. Commun.* **9**, 1–7 (2018).

17. He, X. *et al.* Wafer-scale monodomain films of spontaneously aligned single-walled carbon nanotubes. *Nat. Nanotechnol.* **11**, 633–638 (2016).
18. Lukoševičius, M. & Jaeger, H. Reservoir computing approaches to recurrent neural network training. *Comput. Sci. Rev.* **3**, 127–149 (2009).
19. Shew, W. L., Yang, H., Yu, S., Roy, R. & Plenz, D. Information capacity and transmission are maximized in balanced cortical networks with neuronal avalanches. *J. Neurosci.* **31**, 55–63 (2011).
20. Antonopoulos, C. G., Srivastava, S., Pinto, S. E. d. S. & Baptista, M. S. Do Brain Networks Evolve by Maximizing Their Information Flow Capacity? *PLoS Comput. Biol.* **11**, 1–29 (2015).
21. Miller, K. J., Sorensen, L. B., Ojemann, J. G. & Den Nijs, M. Power-law scaling in the brain surface electric potential. *PLoS Comput. Biol.* **5**, e1000609 (2009).
22. Chen, T., Bobbert, P. A. & Wiel, W. G. 1/ f Noise and Machine Intelligence in a Nonlinear Dopant Atom Network . *Small Sci.* **1**, 2000014 (2021).
23. Demis, E. C. *et al.* Nanoarchitectonic atomic switch networks for unconventional computing. *Jpn. J. Appl. Phys.* **55**, (2016).



## Chapter 7

### Future scope and Conclusion

#### 7.1 Future scope

In the previous chapters we have seen that the in-materio RC performance of our device works better for any degree of non-linear task but has a degrading performance in constructing larger time step delays. In order to increase the MC, two key factors are important regarding construction of the reservoir, (i) adjusting the ratio of SWNT/Por-POM which can be a balancing factor of linear-nonlinear regime and (ii) to increase the number of output nodes in order to have more temporal information of the input signal. The MEA we have used majorly consists of a lower number of output pads compared to atomic switch network systems. A possible way is to fabricate greater electrode pads, but this would require us to shift from cost-effective photolithography to e-beam lithography technique, which though has a high resolution but is also time-consuming. The most prominent way one can do is to use a time-delayed reservoir system with only one real node consisting of SWNT/Por-POM and other virtual nodes created by feed-backing the output signal to input again with a time step delay.<sup>1,2</sup> Since the distribution of Por-POM is heterogeneous itself, so the point of choosing the best electrode pad out of many, to be used as the one output node, adds in an uncertainty to the entire system, as there will be a large variation in device to device performance. So, in this regard a better and prominent solution would be to change the surface dimensionality. Instead of creating a 2D-thin film, we can use a 3D cube coated with SWNT/Por-POM equivalent to a 3D brain structure as shown in Fig. 7.1a. The direct advantage is the availability of multiple surfaces throughout the volume, where each 2D surface can now act as a layer of interconnected dynamical system. Without the use of photolithography we can pin electrodes at different points

of the surface and collect the dynamics from both the outer and the inner surface thereby giving us more high dimensional temporal dynamics about the input. This is reflected in the memory capacity (MC) plot Fig. 7.1b-c, where the 2D device showed a low MC (as suggested in *Chapter 3*), but the MC got enhanced for 3D to about 9.8. In order to see this effect on in-materio RC task we performed two non-linear autoregressive moving average (NARMA) time series prediction of NARMA-2; Eq. (7.1), and NARMA-10; Eq. (7.2), where the number denotes k-step time lag in the functions to be reconstructed by the reservoir outputs. The tasks were performed with the same measurement set-up and RC learning principle discussed in *Chapter 3* and the performance of both the devices was analyzed by the test accuracy. A clear increase in both NARMA- 2 and NAMRA-10 can be observed from Fig. 7.1d-e for the 3D sample, indicating that the volumetric density increase in the network topology can play a role for better performance. Although the results are promising but factors such as SWNT/Por-POM weight ratio, size of the template structure, number of output electrodes and the network density distribution need to be studied further and optimized for the devices in order to have a comparative inference for both the devices

$$y(k+1) = \alpha y(k) + \beta y(k)y(k-1) + \gamma u(k)^3 + \delta \quad [\alpha = 0.4, \beta = 0.4, \gamma = 0.6 \text{ and } \delta = 0.1] \quad (7.1)$$

$$y(k+1) = \alpha y(k) + \beta y(k) (\square y(k-i)) + \gamma u(k-9) u(k) + \delta \quad (7.2)$$

$$[\alpha = 0.3, \beta = 0.04, \gamma = 1.5 \text{ and } \delta = 0.1]$$

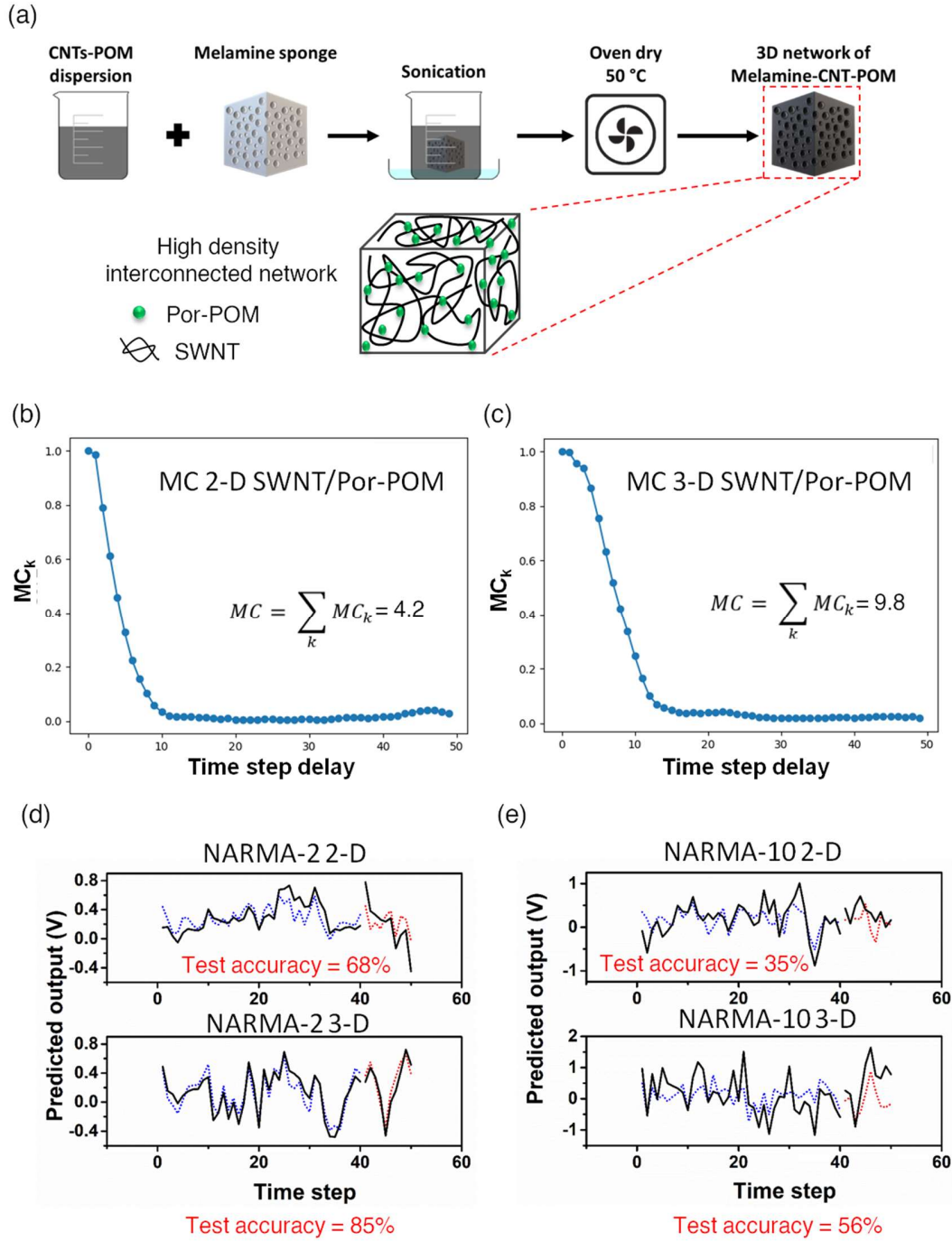


**Fig. 7.1** An idea of preparing a 3D reservoir with SWNTT/Por-POM. (a) Schematic of the synthesis procedure using a porous sponge allowing SWNT/Por-POM to be seeped in and cover the entire surface as seen in the inset. (b) Low MC of 2D device. (c) High MC of 3D device. (d) Top shows the NARMA-2 for 2D device while the bottom for the 3D device. (e) Top shows the NARMA-10 for 2D device while the bottom for the 3D device. In both the NARMA task, 3D device performed better.

## 7.2 Conclusion

The problem statement of generating an in-materio RC device with random network of SWNT/Por-POM molecule was successfully demonstrated in this research work. A simple sonication procedure was adopted for preparing the SWNT functionalized Por-POM as confirmed from the various characterization methods. The UV-Vis spectroscopic studies revealed that the characteristic peaks of porphyrin Soret band at 413 nm, W-O charge transfer band at 266 nm and other high wavelength Q bands along with E<sub>11</sub> and E<sub>22</sub> semiconducting bands of SWNT were all present in the SWNT/Por-POM complex confirming its successful synthesis. The AFM and FE-SEM showed that the surface morphology contained variable height thickness of Por-POM in the intertwined network of SWNT, thereby giving a brain-like heterogeneous distribution of random network structure driven by sonication and wet transfer thin film deposition process. The rudimentary RC task of a sine wave approximation with non-linear  $\nu$  and time-delay memory  $\tau$  parameters was performed to reflect on the reservoir dynamics present in the system. The results showed a consistent performance of target construction for both low and high  $\nu$  in the regime of smaller  $\tau$ , but failed drastically for greater values  $\tau$ . To understand this trade-off the memory capacity (MC) and the I-V characteristics was performed. The MC followed a gradual decay over increasing time step delays with a value of 4.2 confirming the presence of fading memory a behavior related to the echo state property. On the other hand the I-V showed clear non-monotonic current increase in the entire range of negative to positive bias with characteristic NDR peaks. These observations validate the above mentioned point of the memory-nonlinearity trade-off in the sense that because of low MC the device could not reconstruct the past information when delayed by higher values  $\tau$ , but on the contrary its high non-linear dynamics aided in the accurate task performance for any order of non-linearity. Such valuable computation can be thought to arise

from the intrinsic spatio-temporal dynamics of high dimensional NDR like fluctuations. The I-t along with its power spectral density disclosed that these fluctuations are a source of  $1/f^\beta$  scale-free noise which happens to be an important parameter for maximized information processing at the ‘edge of chaos’ brain like computation. Thus based on the above results, we designed three benchmark RC tasks that harnessed the non-linear dynamics of the device rather than the memory property and included waveform generation, Boolean logic function optimization and tactile sensory based object classification to test the in-materio RC performance of our device. The waveform generation was an extension of the sine wave approximation but without the term and constituted the Fourier transformation of the sine waves to various other forms of cosine, triangular, square and sawtooth waves of increasing non-linear complexity. The MEA architecture was adopted to carry out these tasks as it enabled us to exploit the high dimensional voltage readouts from multiple electrode pads which acted as the nodes. A simplified multiple linear regression was adopted to optimize each output weights and target was constructed via the weighted linear combinations of these outputs. The training and testing was done for different epoch sections of the output sine waves and the test performance was evaluated via the NMSE/accuracy. Initially, we studied the input-output relationship via Lissajous plots (LP) to understand the dynamics emerging from the device. Multiple trajectories of LP were obtained from proportional amplitude attenuated non-linear curves to phase delayed ones, emphasizing the importance of heterogeneity in the network structure. Different nodal points actually acted as different electrical circuits of varying resistive-capacitive junctions within the random network leading to such versatile computational regimes of overall. Similar observation was concluded in the time-domain space as well, where the FFT plots displayed multiple higher harmonic generations of odd and even overtones, initially absent in the input signal. The rich dimensionality in both the spatio-temporal

space arises because of the charge transfer interactions at the junctions of SWNT and Por-POM upon perturbing it with external stimuli. Such dynamics is important as Fourier series demands the linear combination of infinite sine waves of varying amplitudes, phases and frequency overtones. Because of this, the device was actually able to construct all the waveforms with a greater accuracy except for the sawtooth which lagged relatively. The best performance was obtained for triangular and cosine with 99% accuracy as these mostly resemble the sine wave shape and requires less non-linearity and combination of frequency overtones with/without phase delayed outputs. The second best performance was obtained square with 86% accuracy followed by sawtooth with 76%. Although both these waveforms require the same degree of non-linearity higher than the triangular and cosine ones, but sawtooth requires additional even overtones with the odd ones compared to square which requires only the latter. The slight performance degradation can thus be attributed to the lower intensity of the even harmonics that were generated from our device which might have hindered the construction of sawtooth. Another important point that surfaced up was the fault tolerant performance. The same tasks were performed for lower number of outputs where the accuracy gradually decreased from training eleven to seven to three outputs. The most prominent drop was observed for the three output case, with the seven performing equally well as the eleven. Two important things can be inferred. (i) That the lack of high dimensional outputs reduces the linear combinations thereby affecting the accuracy, so for the device to perform better it is indeed important to have more non-linear high-dimensionality which is an important parameter for any reservoir device. (ii) The slow decrease of the performance, reflects on the importance of the non-homogeneous random recurrent network which consists of multiple computational regimes, as a result of which even in the absence of few outputs the device still performed without full failure manifesting in the fault tolerant property. The successful in-matrix RC performance lead us to test

the device for another challenging task of Boolean function optimization where the reservoir dynamics was now exploited with two simultaneous inputs of binary ‘0’ and ‘1’. Reconstruction of all six functions of OR, AND, NOR, NAND, XOR and XNOR were successfully obtained with an accuracy above 95% by applying the same learning optimization techniques as the waveform generation. The device could undergo multitasking as in it was able to learn all the function optimizations from the same unit without any interference reflected from the variable weight distributions of output electrodes for each of the Boolean function. It puts forth the point that without forgetting the SWNT/Por-POM’s readout dynamics can be trained efficiently for separate tasks because of the ease of training only the output layer without disturbing the reservoir layer which mostly happens for recurrent neural networks because of back propagation technique. The device performance was robust against multiple test datasets because output for each of the electrodes for the entire test datasets collected from the same input showed a high correlation. This is possible only because of the echo state property of fading memory. Because our device showed very less MC, so each time when the present input was fed in after some time for generating outputs of different datasets, the states of the reservoir states gathered from the previous inputs faded away hence producing same the readout states every time. Such robust performance was also obtained for different time length scales indicating that the internal dynamics was solely input driven and is retained over all time-scale hence maintaining the computational performance. The implementation of Boolean logic happens to be a consequence of the NDR like non-linearity which acted as machine intelligent index (MII). The presence of equal number both high and low conductance points at increasing bias produced a high MII closer to 1 indicating that the device holds the property of carrying out both additive and subtractive operations required for Boolean algebraic functions of XOR and XNOR. Owing to two function optimization tasks we lastly tested

the device for a classification performance by utilizing the tactile sensory information of different objects when grasped by the Toyota HSR. A binary one-hot vector classification was implemented using the same learning method as the previous two. The device was able to classify all objects of differing hardness into their respective classes by following their one-hot encoded targets. It was shown that this task performance got enhanced over time as a function of the maximized information. Initially a no separation region was observed because of lack of information processing reflected from the low  $\gamma$  value of  $1/f^\gamma$  power law. The classification became prominent and separated into '1' and '0' target vectors only when the power law got intense with higher  $\gamma$  value. Overall, the SNWT/Por-POM showed its in-material RC performance by utilizing all its intrinsic dynamics. Each of the parameters of non-linearity, NDR effect and  $1/f^\gamma$  power law all were exploited for different task. The presence of inhomogeneous random network structure did play a crucial role in generating high dimensional patterns and produce fault tolerant operations. The echo state property was also useful for the device to show the robustness in computational performance. Lastly, we also propose a plan to realize a 3D SNWT/Por-POM network like the human brain which can prove beneficial for higher memory tasks also apart from the non-linear ones. In summary, the field of physical RC is vast and materials are being constantly explored for variable task performance. Experimenting the intrinsic dynamical properties specific to each material can thus pave way for deeper understandings in the realm of in-material RC. Here, we extrapolated the idea that apart from the general use of SNWT/polyoxometalates in the field of catalysis and supercapacitors, their redox mediated charge transfer property charge if electrically exploited via voltage or current readouts can pave way for large scale non-silicon based unconventional in-material RC in near future.



## References

1. Haynes, N. D., Soriano, M. C., Rosin, D. P., Fischer, I. & Gauthier, D. J. Reservoir computing with a single time-delay autonomous Boolean node. *Phys. Rev. E - Stat. Nonlinear, Soft Matter Phys.* **91**, 2–6 (2015).
2. Ortín, S. & Pesquera, L. Reservoir Computing with an Ensemble of Time-Delay Reservoirs. *Cognit. Comput.* **9**, 327–336 (2017).

## List of Publications

1. D. Banerjee, S. Azhari, Y. Usami, H. Tanaka, “Room temperature demonstration of in-materio reservoir computing for optimizing Boolean function with single-walled carbon nanotube/porphyrin-polyoxometalate composite”. **Applied Physics Express**. DOI: 10.35848/1882-0786/ac24db (2021) **(accepted)**.
2. D. Banerjee, Y. Xinguang, D. G. O. Hernowo, , Y. Yamazaki, T. Ogawa, H. Tanaka, “Pulse Generation Behavior of Single-Walled Carbon Nanotube/ Polyoxometalate Complex Random Network”. **Proceedings of International Symposium on Applied Science**, 3, 150 – 153 (2019).
3. D. Banerjee, T. Kotooka, S. Azhari, Y. Usami, T. Ogawa, J. K. Gimzewski, H. Tamukoh, H. Tanaka, “Emergence of In-Materio Intelligence from an Incidental Structure of Single-Walled Carbon Nanotube–Porphyrin Polyoxometalate Random Network” **(under review)**.
4. S. Azhari, D. Banerjee, T. Kotooka, S. Murazoe, Y. Usami, and H. Tanaka, “Performance of two- and three-dimensional single-walled carbon nanotubes-polyoxometalate network as in-materio reservoir computing device” **(under review)**.

## List of Conferences

### Oral Presentations

1. Banerjee Deep, Xinguang Yu, Detiza Goldianto Octensi Hernowo, Yoshito Yamazaki, Takuji Ogawa, Hirofumi Tanaka, “*Pulse generation behavior of single-walled carbon nanotube/porphyrin-polyoxometalate complex random network*”. The International Symposium on Applied Science (ISAS), 2019, Ho Chi Minh University, Vietnam.
2. Banerjee Deep, Yoshito Yamazaki, Takuji Ogawa, Hirofumi Tanaka, “*Neuron-like pulse behavior of single-walled carbon nanotube/porphyrin-polyoxometalate complex random network*”. The 80<sup>th</sup> Autumn Meeting of Japanese Society of Applied Physics (JSAP), 2019, Hokkaido University, Sapporo, Japan.
3. Banerjee Deep, Yoshito Yamazaki, Takuji Ogawa, Hirofumi Tanaka, “*Reservoir computing with single-walled carbon nanotube/polyoxometalate random network*”. The 67<sup>th</sup> Spring Meeting of Japanese Society of Applied Physics (JSAP), 2020, Hokkaido University, Sapporo, Japan.
4. Banerjee Deep, Takumi Kotooka, Yoshito Yamazaki, Takuji Ogawa, Hirofumi Tanaka, “*A physical reservoir system from dynamical single-walled carbon nanotube/porphyrin-polyoxometalate random network*”. The 33<sup>rd</sup> International Microprocesses and Nanotechnology Conference (MNC), 2020, Virtual in Zoom, Japan.
5. Banerjee Deep, Yoshito Yamazaki, Takuji Ogawa, Hirofumi Tanaka, “*Physical reservoir system with single-walled carbon nanotube/ asymmetric porphyrin sandwiched polyoxometalate random network*”. The 81<sup>st</sup> Autumn Meeting of Japanese Society of Applied Physics (JSAP), 2020, Virtual in Zoom, Japan.

6. Banerjee Deep, Yoshito Yamazaki, Takuji Ogawa, Hirofumi Tanaka, “*Physical reservoir system with single-walled carbon nanotube/ asymmetric porphyrin sandwiched polyoxometalate random network for waveform generation*”. The 11<sup>th</sup> Molecular Architectonics Meeting (MoleArc), 2020, Virtual in Zoom, Japan.
7. Banerjee Deep, Yoshito Yamazaki, Takuji Ogawa, Yuki Usami, Hirofumi Tanaka, “*Single-walled carbon nanotube/ porphyrin polyoxometalate physical reservoir device for supervised learning*”. The 82<sup>nd</sup> Spring Meeting of Japanese Society of Applied Physics (JSAP), 2020, Virtual in Zoom, Japan.

#### **Poster Presentations**

1. Banerjee Deep , Tomoya Ishizuka , Takahiko Kojima , Takuji Ogawa, Hirofumi Tanaka, “Neuronal pulse behavior using single-walled carbon nanotube/porphyrin polyoxometalate random network”. The 32<sup>nd</sup> International Microprocesses and Nanotechnology Conference (MNC), 2019, Hiroshima, Japan.
2. Banerjee Deep , Yoshito yamazaki , Takahiko Kojima , Takuji Ogawa, Hirofumi Tanaka, “Brian-like pulse impulses emerging from single-walled carbon nanotube/porphyrin polyoxometalate random network”. The 10<sup>th</sup> Molecular Architectonics Meeting (MoleArc), 2019, Fukuoka, Japan.



